AFOSR Grant Number 84-0044

ANALYSIS OF LONG BONE AND VERTEBRAL FAILURE PATTERNS

HAHNEMANN UNIVERSITY
PHILADELPHIA, PA 19102

Jo Ann C. Eurell, D.V.M., Ph.D.

Controlling Office: USAF Office of Scientific Research/NL
Bolling Air Force Base, DC 20332

Unclassified

SECURITY CLASSIFICATION OF THIS PAGE (When Data Entered)

REPORT DOCUMENTATION PAGE	READ INSTRUCTIONS BEFORE COMPLETING FORM
1. REPORT NUMBER AFOSR-TR- 85-0454 2. GOVT ACCESSION NO. A154796	3. RECIPIENT'S CATALOG NUMBER
4. TITLE (and Subtitle) ANALYSIS OF LONG BONE AND VERTEBRAL FAILURE PATTERNS	5. TYPE OF REPORT & PERIOD COVERED Final Scientific Report 6. PERFORMING ORG. REPORT NUMBER
7. AUTHOR(s) Jo Ann C. Eurell	8. CONTRACT OR GRANT NUMBER(s) AFOSR-84-0044
9. PERFORMING ORGANIZATION NAME AND ADDRESS Department of Anatomy, MS 408 Hahnemann University, Broad and Vine Sts. Philadelphia, PA 19102	10. PROGRAM ELEMENT, PROJECT, TASK AREA & WORK UNIT NUMBERS 2312/A1 61102F
11. CONTROLLING OFFICE NAME AND ADDRESS Air Force Office of Scientific Research Building 410 (NL) Bolling AFB, DC 20332	12. REPORT DATE February 14, 1985 13. NUMBER OF PAGES 214
14. MONITORING AGENCY NAME & ADDRESS(if different from Controlling Office)	15. SECURITY CLASS. (of this report) Unclassified 15a. DECLASSIFICATION/DOWNGRADING SCHEDULE

16. DISTRIBUTION STATEMENT (of this Report)

Approved for public release; distribution unlimited.

Accession For	
NTIS GRA&I	☒
DTIC TAB	☐
Unannounced	☐
Justification	
By	
Distribution/	
Availability Codes	
Dist	Avail and/or Special
A/1	

17. DISTRIBUTION STATEMENT (of the abstract entered in Block 20, if different from Report)

18. SUPPLEMENTARY NOTES

Cont'd

19. KEY WORDS (Continue on reverse side if necessary and identify by block number)

Spinal column, impaction, electron microscopy, light microscopy, intervertebral discs, bone histomorphometry, fracture.

DTIC COPY INSPECTED

20. ABSTRACT (Continue on reverse side if necessary and identify by block number)

This report documents five years of work on the normal anatomy of the rhesus monkey vertebral column, the vertebral column response to compressive loading, and the response of bone to hypokinesia. The surface of fractures of long bones were also examined. The rhesus monkey vertebral column was similar to the human spine anatomically, with the exception of the cartilaginous end plates which had unique islands of calcification. The primate vertebral column responded to compressive loading by bending or fracture of

Cont'd

DD FORM 1473

UNCLASSIFIED

bone within individual vertebral bodies, burst injuries in spinal units, and stimulation of osteophyte formation in in vivo impacted spines. Bone formation appeared to be inhibited by hypokinesia in the femur, rib, and vertebral body of exposed rhesus monkeys. Torsional and straight fractures of long bones had varied surface texture due to different angles of fracture planes across the bone matrix. Originator Supplied Keywords include:)

(See DD 1473 (Block 19)

AFOSR Grant Number 84-0044

ANALYSIS OF LONG BONE AND VERTEBRAL FAILURE PATTERNS

HAHNEMANN UNIVERSITY
PHILADELPHIA, PA 19102

Jo Ann C. Eurell, D.V.M., Ph.D.

Controlling Office: USAF Office of Scientific Research/NL
Bolling Air Force Base, DC 20332

ABSTRACT

The normal anatomy of the rhesus monkey vertebral column including radiology, scanning electron microscopy (SEM), light microscopy (LM), and quantitative histochemistry was described. The radiology correlated with previously described gross anatomy of the rhesus monkey spine. The vertebral body consisted of trabecular bone arranged in three zones. A cartilaginous end plate separated the intervertebral disc from the underlying bony vertebral body and contributed to growth in length of the body. The end plate contained unique islands of calcification not present in humans. Blood vessels were observed crossing the plate in the area of the nucleus pulposus, and were thought to be embryonic blood vessel remnants. The articular cartilage of the zygapophysial joints varied from smooth to severely disrupted.

Primate vertebral columns were subjected to compressive loading and examined with SEM and LM. Individual vertebral bodies were compressed to 50% of their original height at three different strain rates. The trabecular bone of the bodies deformed by bending in an anterior-posterior direction at the lower strain rates, and fracturing at the higher strain rates.

Compressed spinal units responded to loading with burst-type injuries. The relatively compression resistant nucleus pulposus herniated into the vertebral body. The cartilaginous end plate was fractured and was usually separated from the adjacent vertebral body. Anterior collapse of the vertebral bodies was often noted.

In-vivo impacted baboon vertebral columns had anterior osteophytes which were first noted in the six months post impaction

group and progressed to multiple exostoses by six years post-impaction. Damage to the cartilaginous end plates and intervertebral discs of the impacted animals was minimal. Degeneration of the posterior zygapophysial joints increased with time, and was possibly related to changes in the anterior column.

Rhesus monkeys were exposed to hypokinesia, and the bone dynamics during recovery of the femur, rib, and vertebral body were studied with histomorphometry. Hypokinesia appeared to inhibit bone formation in all three bones. Inhibition appeared to be at the osteoblast level. Recovery following hypokinesia was most delayed in the vertebrae.

Torsional and straight fracture surfaces of long bones were studied with SEM. The fracture surface texture varied with the fracture type due to the different angles of the two fracture planes across collagen fibers and mineralized matrix.

TABLE OF CONTENTS

THE NORMAL ANATOMY OF THE RHESUS MONKEY VERTEBRAL COLUMN

Introduction and Literature Review

The vertebral column consists of vertebrae, intervening intervertebral discs, and associated ligaments. The column provides support for the body trunk, protection for the spinal cord, and an attachment for ribs and muscles. The anterior portion of the column is composed of vertebral bodies and intervertebral discs. Anatomically, the vertebral body is primarily trabecular bone surrounded by a collar of compact bone (Kazarian, 1978). The body is bounded on either end by a cartilaginous end plate. The intervertebral disc is composed of an outer annulus fibrosus and an inner nucleus pulposus. The posterior elements of the column articulate via zygapophysial joints which are bilateral and synovial in type.

Vertebral Body

The vertebral bodies form from mesenchyme which organizes as cartilage around the fetal notochord (Bick and Copel, 1950). Blood vessels invade the cartilage model and trabecular bone forms. The bone eventually expands until a thin cartilaginous end plate is left at either end of the body.

When viewed in sagittal section, the bony portion of the primate vertebral body is composed of three regions: cranial end zone, central zone, and caudal end zone (Eurell and Kazarian, 1982). The trabeculae are fine and the marrow spaces regular and relatively small in the end zones. Each end zone extends about 20% of the body length. The central zone occupies the remaining 60% of the body length and contains coarser trabeculae. The hemocytopoetic spaces are larger and

more irregular toward the midsection of the body. Secondary horizontal trabeculae provide support and stability to the primary vertical trabeculae (Arnold, 1970).

The bony end plate which lies beneath the cartilaginous end plates is perforated by many holes (Calve and Galland, 1930). The peripheral holes are larger than the central holes under the nucleus pulposus. Bone marrow contacts the cartilaginous end plate through these holes and provides nutrition for the cartilage and the disc above. At the junction between the cartilage and bone, the bone is thrown up into radial elevations which fit into corresponding furrows on the cartilaginous plate (Donisch and Trapp, 1971). The cartilaginous plate is attached to the bone by a thin calcified coating (Calve and Galland, 1930).

The cartilaginous end plate was a subject of controversy regarding whether it was a portion of the intervertebral disc or the vertebral body. It is now accepted to be a portion of the vertebral body (Higuchi, et al., 1982). The plate functions in endochondral growth of the vertebral body (Bick and Copel, 1950; Calve and Galland, 1930; Coventry, et al., 1945a; Coventry, et al., 1945b; Peacock, 1951). The plate also serves as an anchor for the intervertebral disc (Harris and Macnab, 1954), as a barrier between the vertebral body and the disc, and as a possible source for the production of matrix of the nucleus pulposus (Higuchi, et al., 1982). The cartilaginous plate thins with age and may completely disappear around age 40 in the human (Coventry, et al., 1945b).

The morphologic zones of the cartilaginous end plate have been described in the marmoset (Bernick, et al., 1980), rhesus monkey

(Nussbaum, 1981), mouse (Higuchi, et al., 1982), and human (Bernick and Cailliet, 1982; Coventry, et al., 1945b). The marmoset cartilaginous plate consists of an outer articular zone next to the intervertebral disc and an inner growth zone next to the bone of the vertebral body.

The marmoset articular zone has scattered chrondrocytes and is homogeneous in appearance. With age, staining of the articular zone changes. Stainable chondroitin sulfate and keratosulfate decrease while PAS positive neutral mucopolysaccharides and sialic acid increase. Fine, argyrophilic collagen fibers with associated calcified "droplets" appear. These changes in the cartilage matrix create an environment for subsequent mineralization (van den Hooff, 1964) which occurs from 1-3 years of age (Bernick, et al., 1980).

The inner growth zone of the marmoset has three regions: 1) columns of proliferating cells, 2) 2-3 layers of hypertrophic cells, and 3) a thin calcifying zone next to the vertebral body. This inner growth zone is similar to the cartilaginous epiphyseal plate of long bones. Histochemically, the growth zone is strongly alcian blue positive.

The maturation of the marmoset cartilaginous plate has been divided into four stages. Stage I represents active growth at 3 to 6 months of age. The cartilage contains predominately type II collagen and chondroitin-sulfate in the ground substance. The maturation phase (stage II) is typified by a decrease in cartilage width and a change to heavier collagen fibers and neutral mucopolysaccharides in the ground substance. By the adult stage (stage III, 1-3 years of age), only isolated areas of growth cartilage remain. The articular

cartilage matrix is calcified, and a bony annular epiphysis has appeared. Stage IV (middle to old age) is characterized by resorption of the calcified articular cartilage.

Nussbaum (1981) has described the cartilaginous end plate of the rhesus monkey. The plate has a heterogenous extracellular matrix with calcified struts separating proteoglycan enriched territorial zones. Nussbaum (1981) states that vascular invasion of the end plate results in progressive ossification of the plate and reestablishment of a blood supply adjacent to the disc. A growth zone is present between the plate and bone of the vertebral body.

Higuchi, et al. (1982) have described the zones of the mouse cartilaginous end plate. The outer articular zone is divided into a superficial region with flattened chondrocytes and a deep region with a calcified matrix. The calcified areas of the deep region are surrounded by a lamina limitans; calcification first appears in this region at one week of age. The formation of a secondary center of ossification occurs around 8 weeks with the appearance of blood vessels, osteoblasts and related cells in the deep portion of the outer articular zone.

The inner growth zone of the murine end plate is composed of chondrocytes arranged in columns. Near the vertebral bone, the chondrocytes are more degenerate and are surrounded by a lamina limitans. The inner growth zone thins with age.

The human cartilaginous plate is similar to the marmoset end plate (Bernick and Cailliet, 1982). An outer articular zone and an inner growth zone are present. The outer zone has elongated chondrocytes scattered throughout the matrix. The inner zone has

parallel columns of proliferating and hypertrophic chondrocytes. A thin zone of calcified cartilage is next to the subchondral trabeculae. Bernick and Cailliet (1982) describe mineralization of the articular zone beginning at 20-40 years of age, followed by resorption of the calcified cartilage in later years until only a thin layer separates the body of the vertebrae from the disc. They further suggest that this calcification along with vascular changes seen in older vertebrae may impede the passage of nutrients from the blood to the disc.

Vascular channels are present in the cartilaginous end plate (Coventry, et al., 1945b; Donisch and Trapp, 1971; Harris and Macnab, 1954; Hirsch and Schajowicz, 1953; Holman and Duff, 1939; Peacock, 1951). Distribution of the vessels is described by Donisch and Trapp (1971). The vessels usually disappear by 10 years of age in humans, but may persist until age 20 (Beadle, 1931). The striated scars which remain may be weak points in the cartilaginous plate which may break down under stress (Harris and Macnab, 1954).

Remnants of the notochord may persist in the cartilaginous end plate as well as in the remainder of the vertebral body and the disc (Peacock, 1951; Walmsley, 1953). Persistence of this tissue may inhibit normal changes in cartilage and the formation of bone. The steak stains lightly basic, is acellular, and has longitudinal striations.

Ossification gaps in the growth layer of the cartilaginous end plate are observed in humans starting about 8 years of age (Schmorl and Junghanns, 1959; Coventry, et al., 1945b). The gaps have horizontal bands of fibrillated cartilage matrix and are acellular.

Although they appear about the time that vascular obliteration begins, they are not located in the vascular passages. The gaps are not present in adults. The significance and origin of the gaps is not known, but they may be weak areas in the plate subject to stress.

The articular zone of the cartilaginous end plate also contains the epiphysis for the vertebral body. All mammals except the anthropoid apes and man have disc-shaped epiphyses on the surfaces of the vertebral bodies (Schmorl and Junghanns, 1959). Humans, orangutans, gorillas, and marmosets have been reported to have a ring-shaped epiphysis referred to as the annular epiphysis (Schmorl and Junghanns, 1959; Bernick, et al., 1980). The ossification center for the annular epiphysis has been reported to appear as early as eight years of age in the human and three years of age in the marmoset. The human annular epiphysis fuses with the rest of the vertebral body around 25 years of age and creates a rim around the margin of the body within which the cartilaginous plate resides (Beadle, 1931).

Intervertebral Disc

The intervertebral disc is divided into a central nucleus pulposus which develops from notochordal remnants, and a peripheral annulus fibrosus which develops from surrounding mesoderm (Coventry, et al., 1945a). The annulus consists of collagenous fibers arranged in annular layers which run obliquely between the vertebral bodies (Harris and Macnab, 1954). The fibers are anchored to the cartilaginous end plate and the anterior and posterior longitudinal ligaments (Coventry, et al., 1945b). The dorsal or posterior portion of the annulus is narrower than the ventral or anterior portion

(Hirsch and Schajowicz, 1953). Nerve fibers (Hirsch and Schajowicz, 1953) and peripheral blood vessels are also present in the annulus (Peacock, 1951).

The collagenous fibers are primarily type I collagen in the periphery of the annulus while type II collagen predominates in the inner portion of the annulus (Adams, et al., 1977). Collagen increases peripherally in the annulus as well as downward along spinal levels with age.

In the feline annulus, hexosamine levels were higher in the cervical and thoracic annuli compared to the lumbar region (Butler and Wels, 1971). Within an individual rabbit disc, keratosulfate levels were found to increase toward the center of the disc (Antonopoulos, et al., 1964). The highest value of hexosamines was found in the inner annulus which supports the basophilia observed histologically (Butler and Wels, 1971; Hirsch and Schajowicz, 1953).

The cells of the annulus fibrosus in the rabbit actively produce chondroitin sulfate in the inner two-thirds of the annulus and have been designated as chondrocytes (Souter and Taylor, 1970). The fibroblast cells in the peripheral one-third of the annulus are less active in mucopolysaccharide production.

In the feline, four cell types have been described in the annulus (Butler and Smith, 1965). Type I cells, which stained orthochromatically with toluidine blue, were present in both the nucleus and cytoplasm. A fine capsule, which was sometimes present around the cell, was metachromatic. Type II cells were surrounded by a small amount of homogeneous or granular metachromatic material that appeared basophilic with hematoxylin and eosin (H&E) stain. Type III

cells were surrounded by an increased amount of metachromatic material. Type IV cells were completely metachromatic, and appeared as a basophilic mass with H&E stain.

The nucleus pulposus of the disc is formed from notochordal tissue which undergoes mucoid degeneration (Peacock, 1951). The notochord is thought to contribute to nuclear matrix in fetal and postnatal life by some authors (Wolfe, et al., 1965), while other authors feel that nuclear matrix is contributed by the chondrocytes of the cartilaginous end plate (Higuchi, et al., 1982). The shape of the nucleus pulposus changes from rectangular to oval with age (Coventry, et al., 1945b). The nucleus is avascular throughout its development (Peacock, 1951).

The fibers of the nucleus pulposus become coarser with age (Coventry, et al., 1945b). Type II collagen predominates in this portion of the disc of humans (Adams, et al., 1977).

The ground substance of the nucleus pulposus contains hyaluronate (Adams, et al., 1977), chondroitin sulfate, and keratosulfate (Souter and Taylor, 1970). Studies of human discs show that hyaluronate increases with age (Adams, et al., 1977). In the rabbit disc, the ratio of keratosulfate to chondroitin sulfate increases with age (0.4 to 2.8) (Davidson and Small, 1963). A similar change in ratio was also shown in human discs by Hallen (1958). Unlike the annulus, the distribution of hexosamines in the nucleus does not seem to change with the level of the vertebral column (Butler and Wels, 1971).

The nucleus pulposus has large, pale-staining multinucleated cells with vacuolated cytoplasm which are classed as chordal cells.

These embryonic cells disappear during the first year of life in the human (Peacock, 1951). Fibroblasts and chondrocytes have also been observed in the nucleus (Coventry, et al., 1945b).

Zygapophysial Joints

The zygapophysial joints are synovial joints located posteriorly between the articular processes of adjacent vertebrae (Lewin, 1964). The joints develop from mesoderm which chondrifies and forms the developing vertebrae (Parke, 1975). The inferior articular facet surface is convex while the superior facet has a concave surface.

The articular cartilage covering the facet is thickest near the center (about 2 mm) (Fick, 1904). Three zones are present in the central region of the articular surface of human lumbar zygapophysial joints (Lewin, 1964). The superficial zone is composed of 3-4 layers of elongate oval cells. An intermediate zone with chondrocytes arranged in groups of 2-3 cells lies deep to the superficial zone. The thickest zone is the deep zone with groups of 6-8 chondrocytes arranged perpendicular to the articular surface. About 1/6 of the articular cartilage thickness is composed of the calcified portion of the deep zone adjacent to the subchondral bone. Vascular buds from the underlying bone protrude into the calcified layer. In peripheral regions of the articular cartilage, the uncalcified deep zone is not present.

At the superior and inferior ends of the zygapophysial joints, there are two articular recesses (Lewin, et al., 1961). The recesses provide a site for joint capsule attachment and a synovial fat pad for lubrication during locomotion.

The joint capsule provides for longitudinal (sagittal) mobility and transverse (horizontal) stability (Lewin, et al., 1961). The capsule is fibrous and very thick on the dorsal part of the joint (Guntz, 1934).

Blood supply to the human zygapophysial joint is derived from branches of the lumbar arteries (Lewin, et al., 1961). The lumbar artery passes through the intervertebral foramen and gives off a branch which pierces the intertransverse ligament to supply the joint capsule.

The innervation of the zygapophysial joints in the rhesus monkey has been documented by Stilwell (1956). The dorsal ramus of the spinal nerve arises just distal to the spinal ganglion. The ramus divides into several branches. Major branches from each spinal nerve supply two successive articulations, and therefore, each joint has bisegmental innervation. A single lumbar spinal nerve supplies an articulation near its emergence and another joint one vertebra cadually.

Rhesus Monkey Vertebral Column

The vertebral formula for the rhesus monkey is $C_7T_{12}L_7S_3Cd_{+20}$. Sherrington (1892) and Schultz (1930) have reported individual variation in the formula at different levels of the column. An excellent discussion of the specific gross anatomy of the rhesus monkey vertebral column has been published by Sullivan (1969) and will not be repeated here. The histology and ultrastructure of the rhesus monkey cartilaginous end plate has been reported by Nussbaum (1981). Other basic histology and electron microscopy of the rhesus monkey vertebral column could not be found in

the literature. It is the objective of this study to report the radiology, posterior innervation, histology, histochemistry, and scanning electron microscopy of the normal rhesus monkey vertebral column.

Materials and Methods

The vertebral columns of five clinically normal, rhesus monkeys (Macaca mulatta) were collected and frozen. Anterior-posterior, lateral and oblique radiographs were taken.

The nerve supply to the posterior zygapophysial joints was dissected at several lumbar levels. Attempts to dissect musculature were unsuccessful because freezing made the tissue too friable.

The vertebral column was slabbed with a meat saw into smaller sections for scanning electron microscopy and light microscopy. The scanning electron microscopy samples were etched in sodium hypochlorite prior to fixation. Following fixation in 10% neutral buffered formalin, the samples were dehydrated, critical point dried, coated with gold palladium, and examined with the scanning electron microscope. The samples for light microscopy were fixed in 10% neutral buffered formalin, decalcified in formic acid-sodium citrate solution, dehydrated, and embedded in paraffin. Individual sections were stained with hematoxylin and eosin (H&E), alcian blue-van Gieson (AB-VG), safranin O-fast green (SO-FG), alcian blue-PAS (AB-PAS), or alcian blue critical electrolyte concentration method (AB-CEC).

All samples were examined and representative photomicrographs were recorded. Slides stained with AB-CEC were quantitated with the microscope-photometer system to evaluate staining for chondroitin and keratosulfates in the intervertebral disc, cartilaginous end plate and trabecular bone of the vertebral body. Analysis of variance was used to statistically evaluate the data from the quantitative histochemistry.

Results

Radiology

Radiographs of the lumbar region of the normal rhesus monkey spine are shown in figures 1-4. The vertebral bodies were square to rectangular in shape and symmetrical. The disc spaces and vertebral processes were of normal conformation. No osteophytes were present. One zygapophysial joint (T_{12}-L_1) of one animal (RM5) was fused; the rest were within normal limits.

Gross Dissection

The distribution of the dorsal and ventral rami of the spinal nerves as determined by dissection is shown in figure 5. The dorsal ramus of the spinal nerve branches to supply epaxial muscles in the area as well as the posterior zygapophysial joint at the level of the emergence of the spinal nerve and the zygapophysial joint immediately caudal.

Scanning Electron Microscopy

Vertebral body. The cortical bone of the vertebral body was perforated by numerous vascular channels on the periosteal surface (fig. 6). The mineralization pattern of the bone of the anterior wall consisted of an irregular surface of rounded projections (fig. 7). Numerous resorption cavities covered the endosteal surface of the cortical bone (Fig. 8).

The trabecular bone of the vertebral body was divided into two end zones and a central zone (fig. 9). The end zones consisted of trabeculae surrounding cuboidal or spherical hemocytopoetic spaces (figs. 9 and 10), in contrast to the central zone which has larger, more irregularly arranged hemocytopoetic spaces. The channel of the

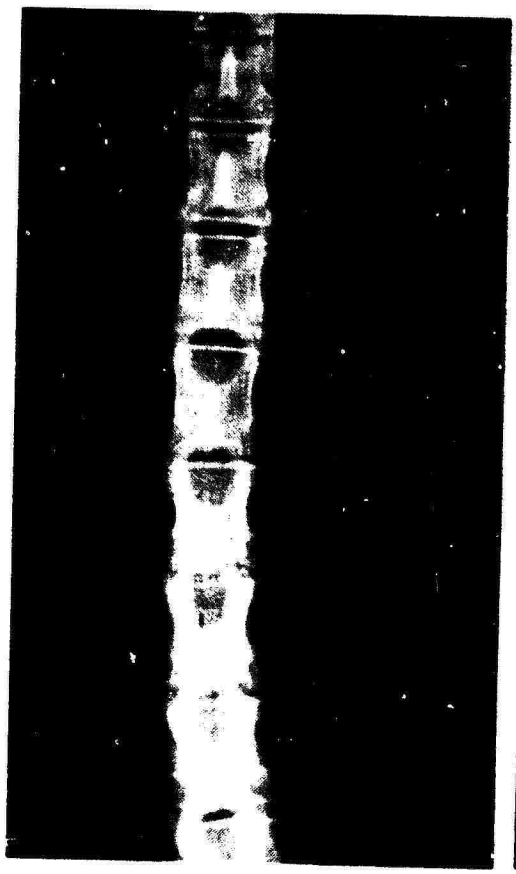

Figure 1. A-P radiograph of T_{11}-L_7, normal rhesus monkey.

Figure 2. Lateral radiograph of T_{12}-L_7, normal rhesus monkey.

Figure 3. Right oblique of T_{11}-L_7, normal rhesus monkey.

Figure 4. Left oblique of T_{11}-L_7, normal rhesus monkey.

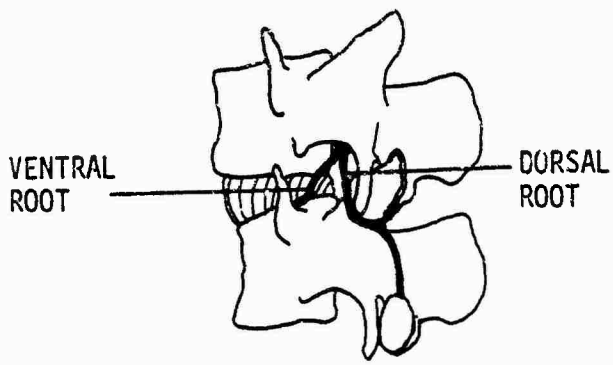

Figure 5. Sketch of the innervation to the posterior facet of the rhesus monkey.

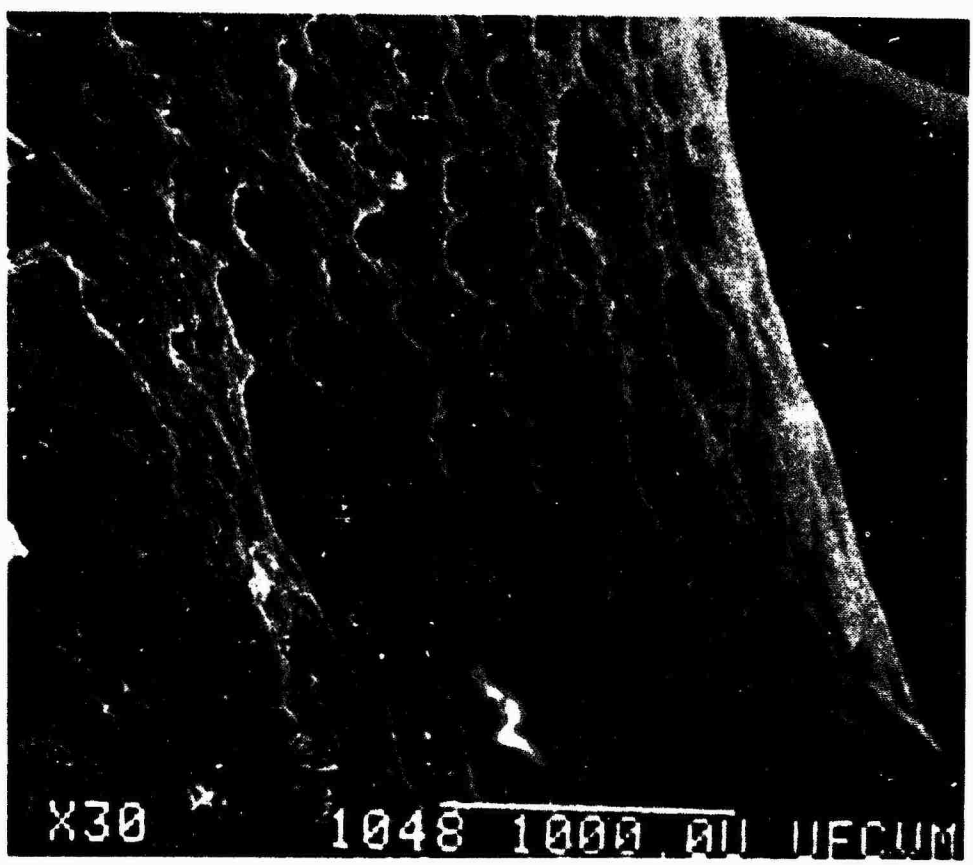

Figure 6. SEM of the anterior cortex of the vertebral body, RM4, T_{10-12}.

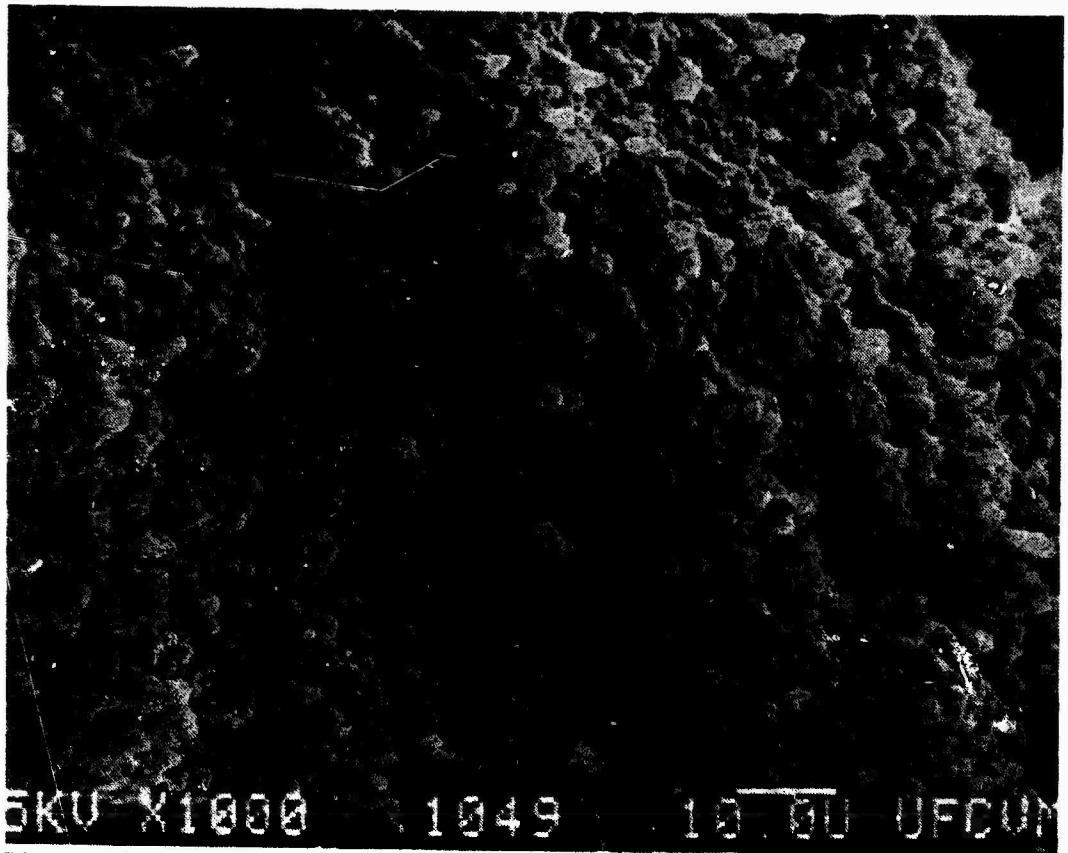

Figure 7. SEM of the mineralization pattern of the bone which forms the anterior cortex of the vertebral body. RM4, T_{10-12}.

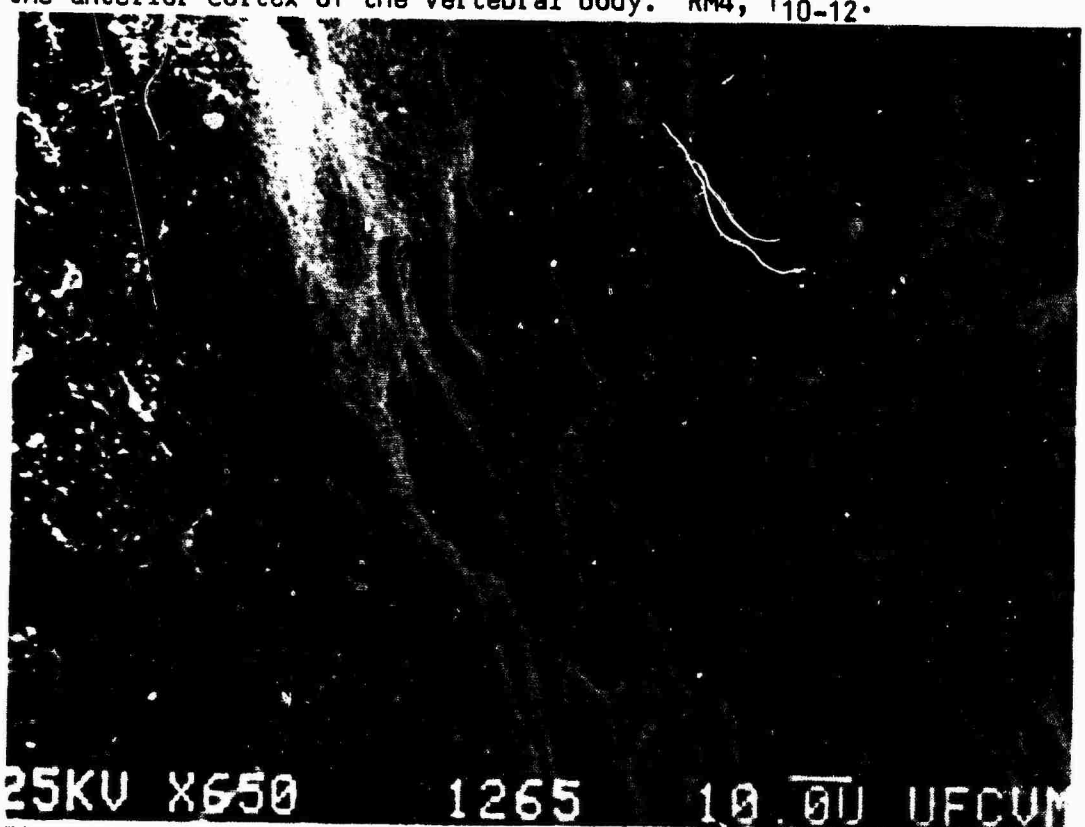

Figure 8. SEM of the endosteal surface of the cortex of the vertebral body. R=resorption cavity. RM1, L_{1-2}.

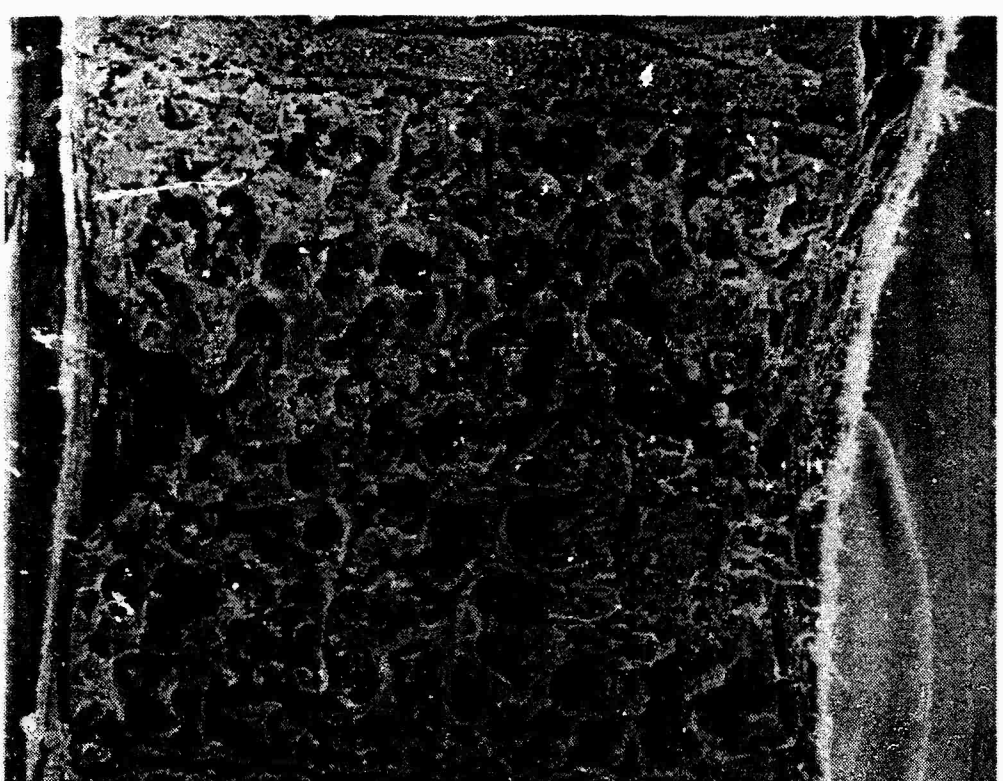

Figure 9. SEM of vertebral body. A=anterior cortex; C=cartilaginous end plate; E=end zone; Ce=central zone. RM3, C_6.

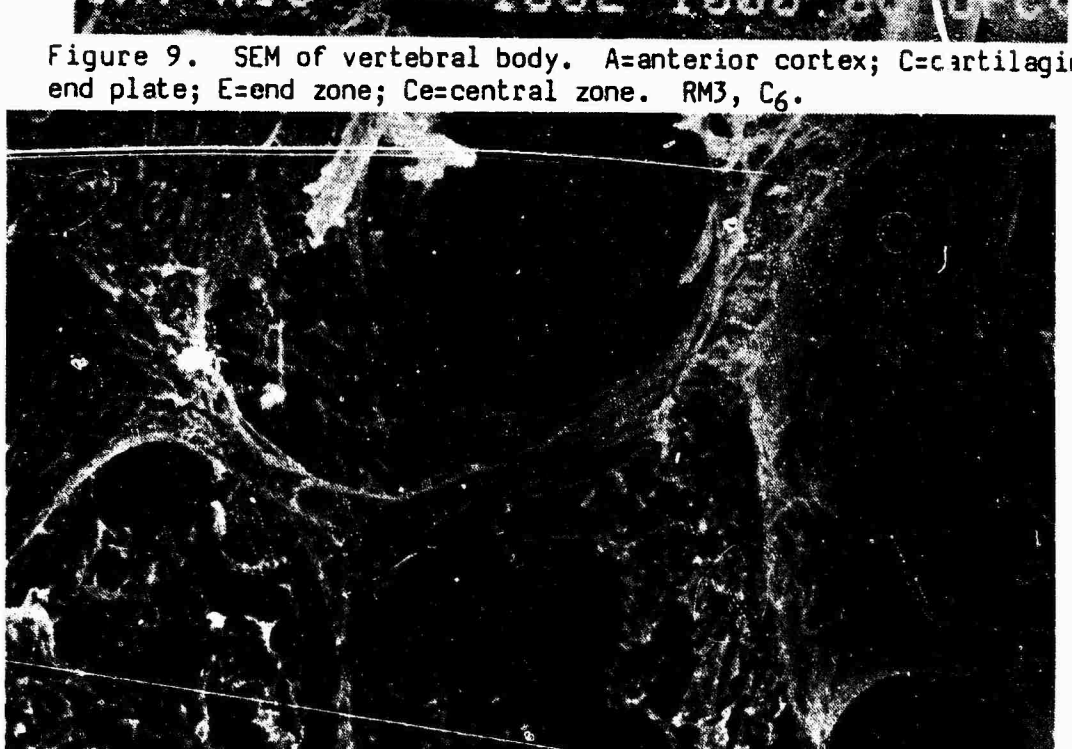

Figure 10. SEM of end zone of vertebral body. RM1, L_1.

basivertebral vein was clearly visible, exiting along the posterior aspect of the body. Anterior and posterior longitudinal ligaments were also present.

The cartilaginous end plates separated the end zones of trabecular bone from the intervertebral disc. Three zones of the cartilaginous end plate were present (fig. 11). The outer non-calcified zone had a homogeneous matrix with scattered, oval lacunae. Fibers from the annulus fibrosus could be seen passing through the outer zone into deeper regions of the plate (fig. 12). The middle calcified zone had scattered islands of mineralization separated by areas of cartilage with a homogeneous matrix and scattered lacunae (figs. 11 and 13). The inner growth zone width was variable and frequently distorted due to processing artifacts (fig. 14). Vertical columns of cartilage, which occasionally surrounded blood vessels, traversed the nuclear region of the end plate (fig. 15). An annular epiphysis of trabecular bone was frequently present in the anterior cartilaginous plate.

Intervertebral disc. The intervertebral disc was composed of an annulus fibrosus of layered collagenous fibers. Anchoring of these collagenous fibers into the cartilaginous end plate of the vertebral body was discussed above. Nuclear material of the disc was removed by processing for SEM, leaving a large cavity in the disc. Fragments of cartilaginous or bony appearing material were observed in the disc of one animal (RM3, T_{8-10}) (fig. 16).

Zygapophysial joint. The articular surfaces of the zygapophysial joint varied from relatively smooth (figs. 17 and 18) to extremely fibrillated (figs. 19 and 20). Intermediate surfaces had

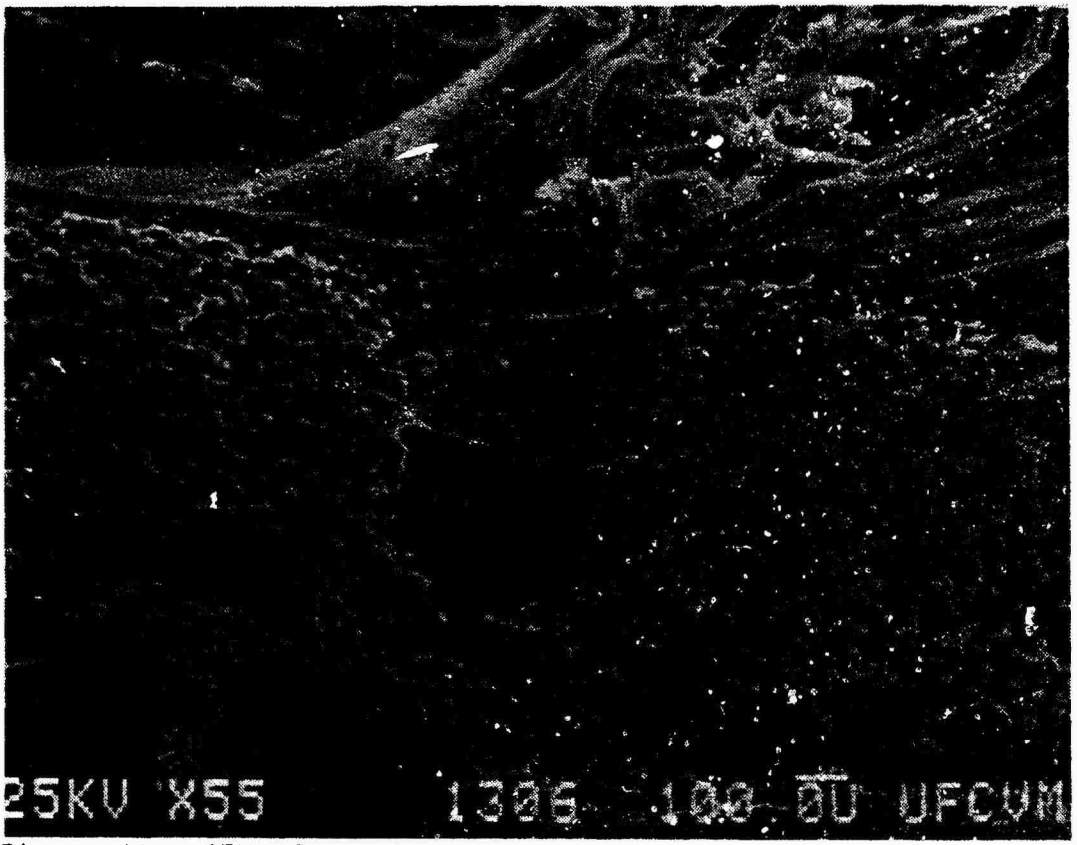

Figure 11. SEM of cartilaginous end plate. 1=outer non-calcified zone; 2=calcified zone; 3=growth zone;v=vertical column. RM3, L_{1-2}.

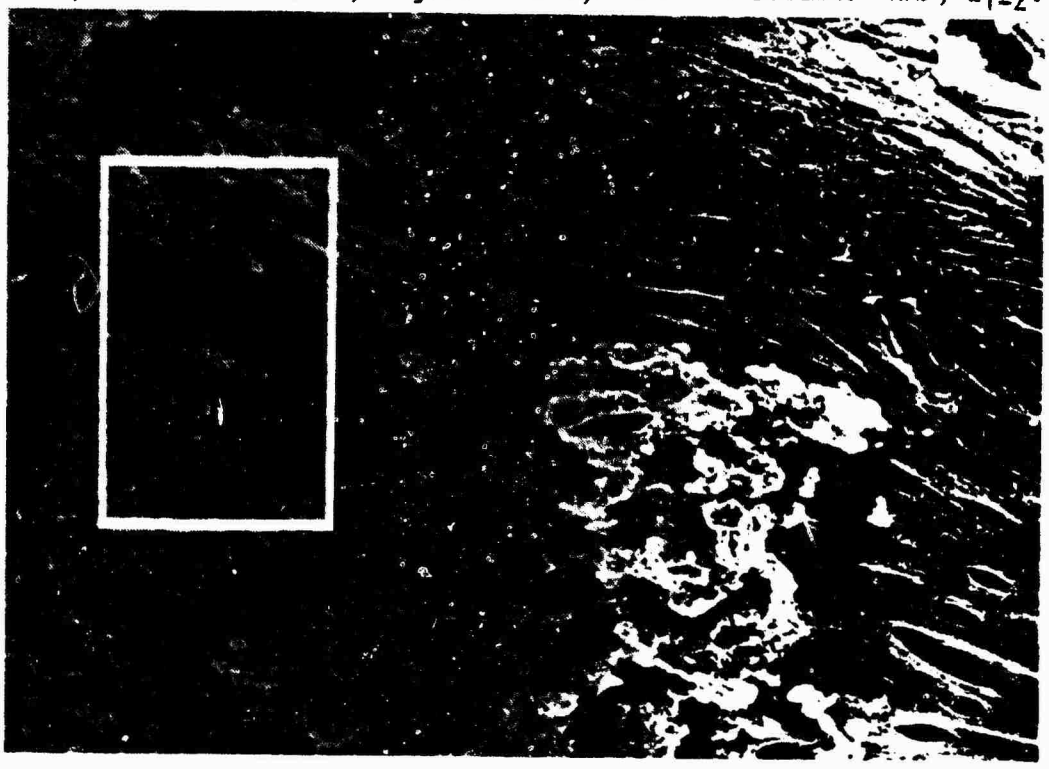

Figure 12. SEM of fibers from the annulus fibrosus passing into the cartilaginous end plate. Higher magnification of area in box shown on the right. RM2, L_{5-6}.

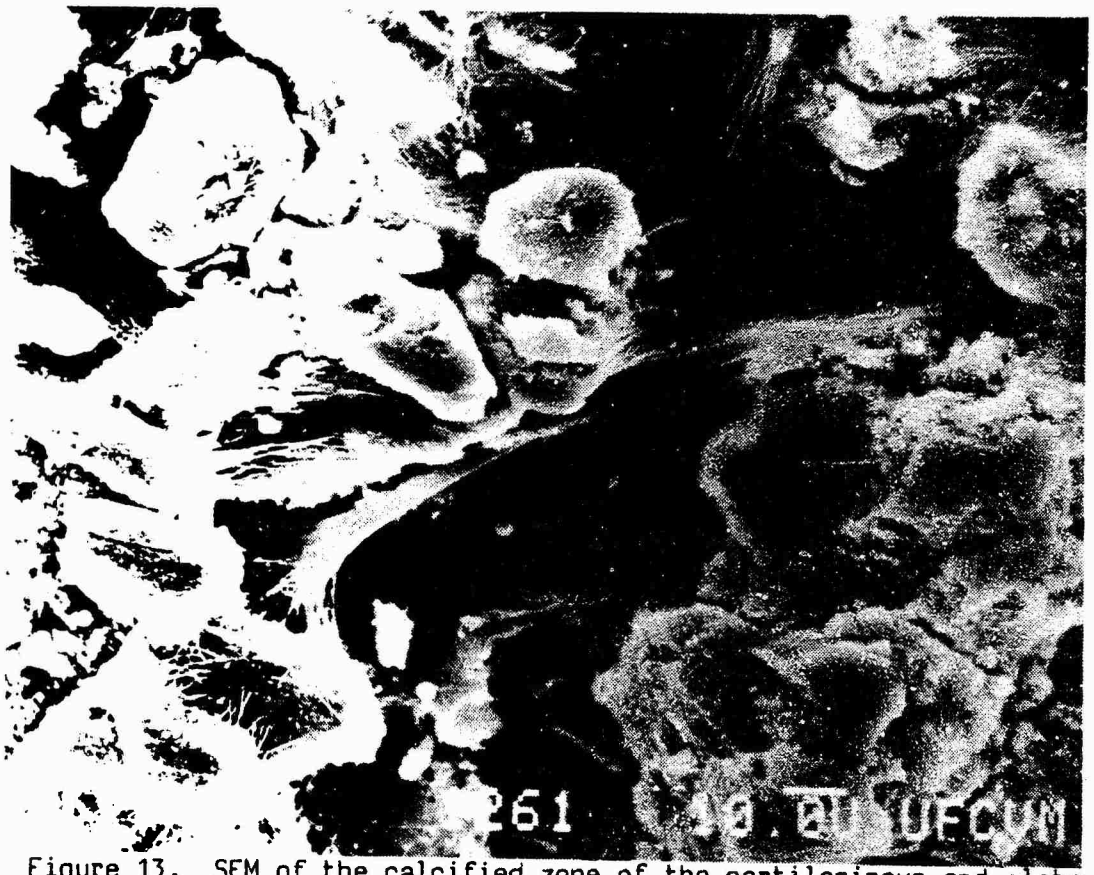

Figure 13. SEM of the calcified zone of the cartilaginous end plate. M=island of mineralization; U=unmineralized cartilage. RM1, T_{12}-L_1.

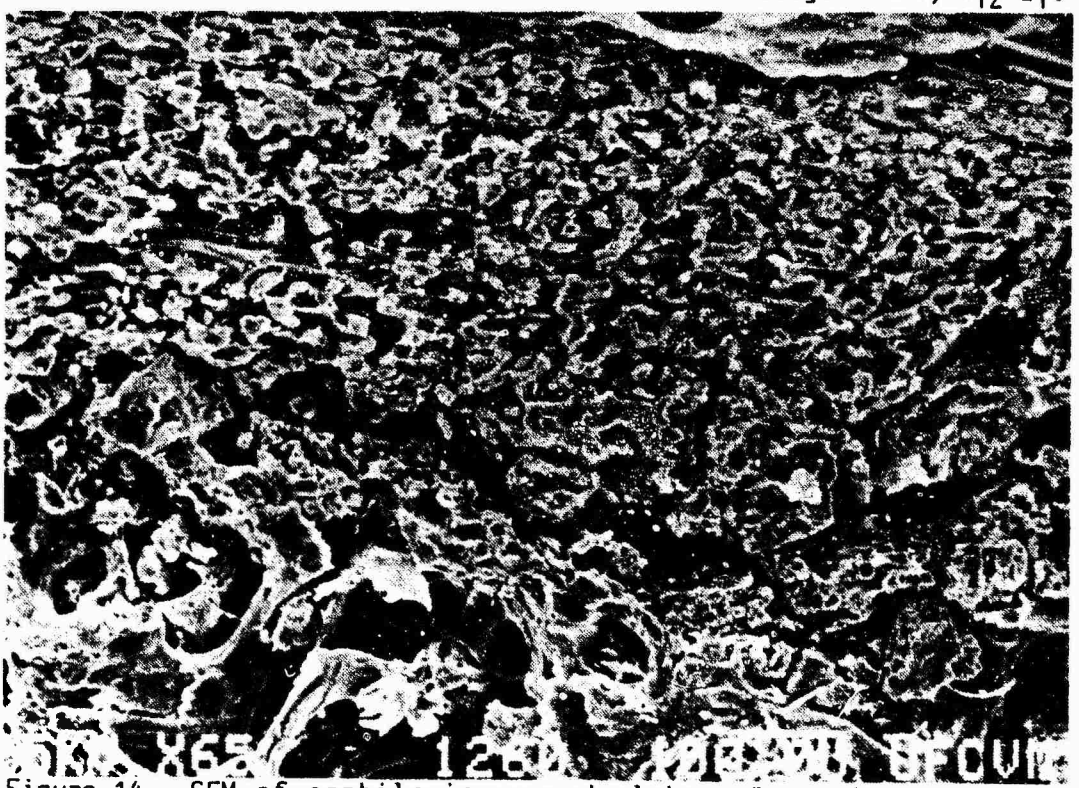

Figure 14. SEM of cartilaginous end plate. G=growth zone. RM1, T_{12}-L_1.

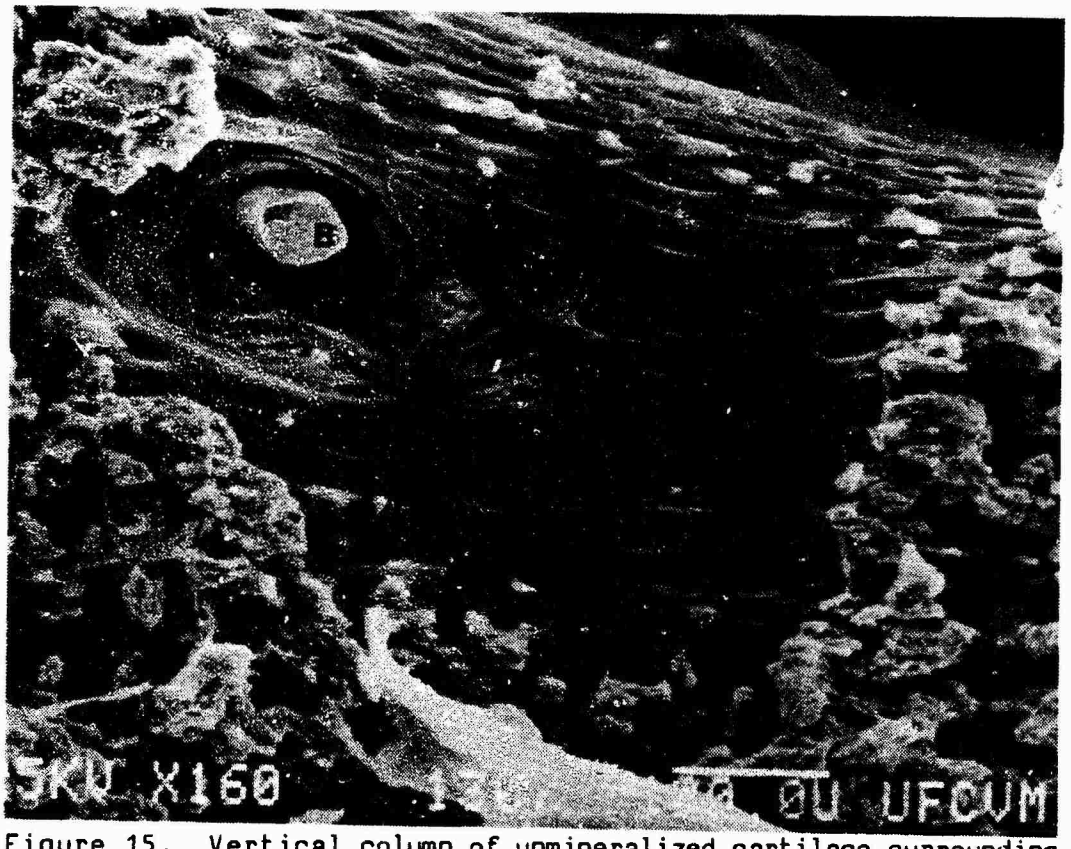

Figure 15. Vertical column of unmineralized cartilage surrounding a blood vessel (B). RM3, L_{3-4}.

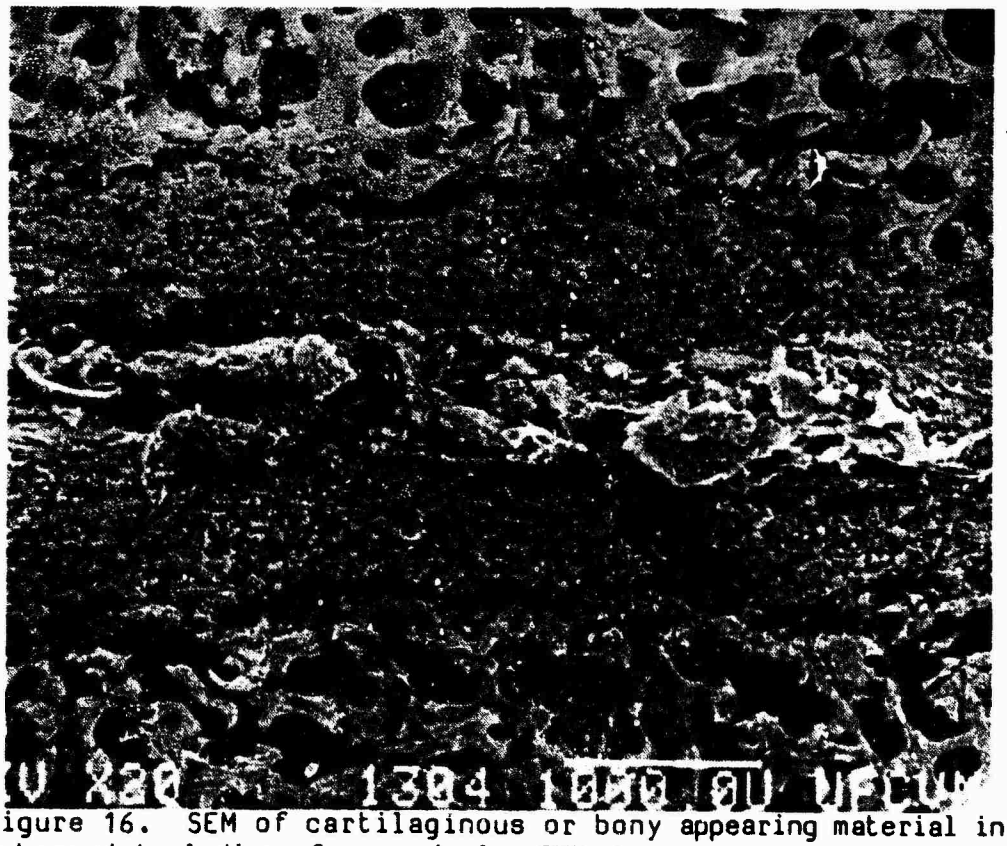

Figure 16. SEM of cartilaginous or bony appearing material in the intervertebral disc of one animal. RM3, T_{8-10}.

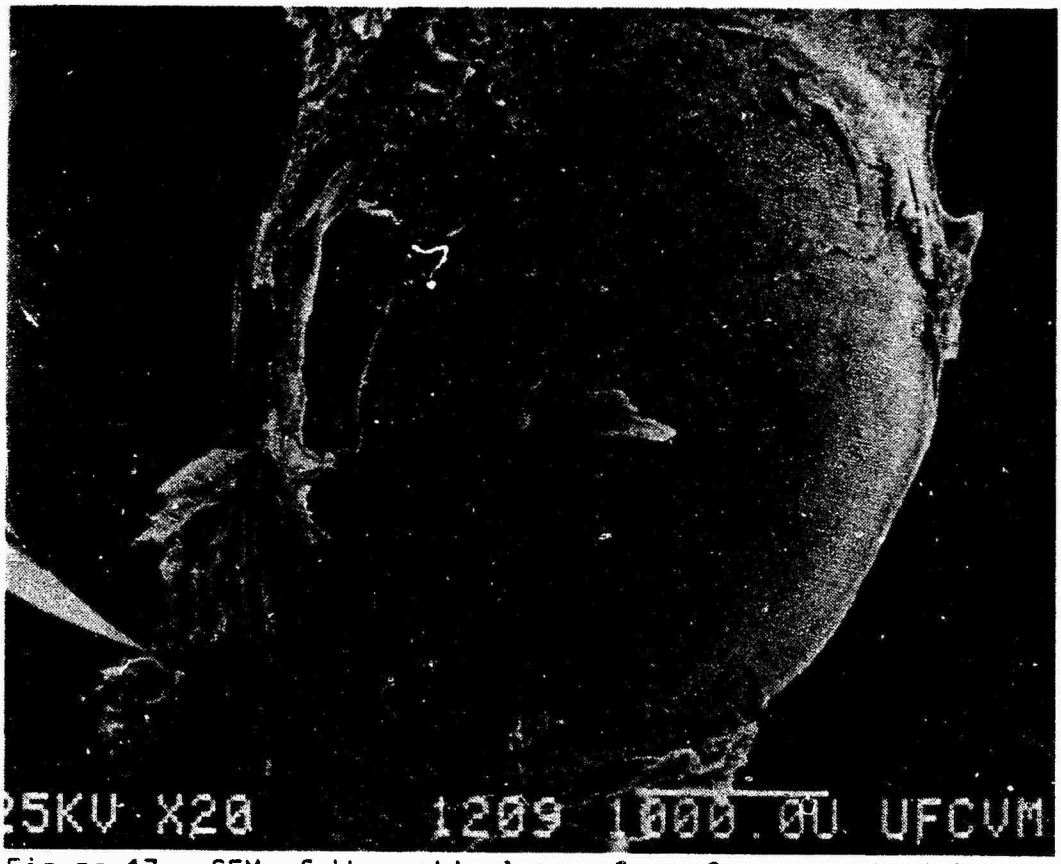

Figure 17. SEM of the articular surface of a zygapophysial joint. RM4, L_1 inferior.

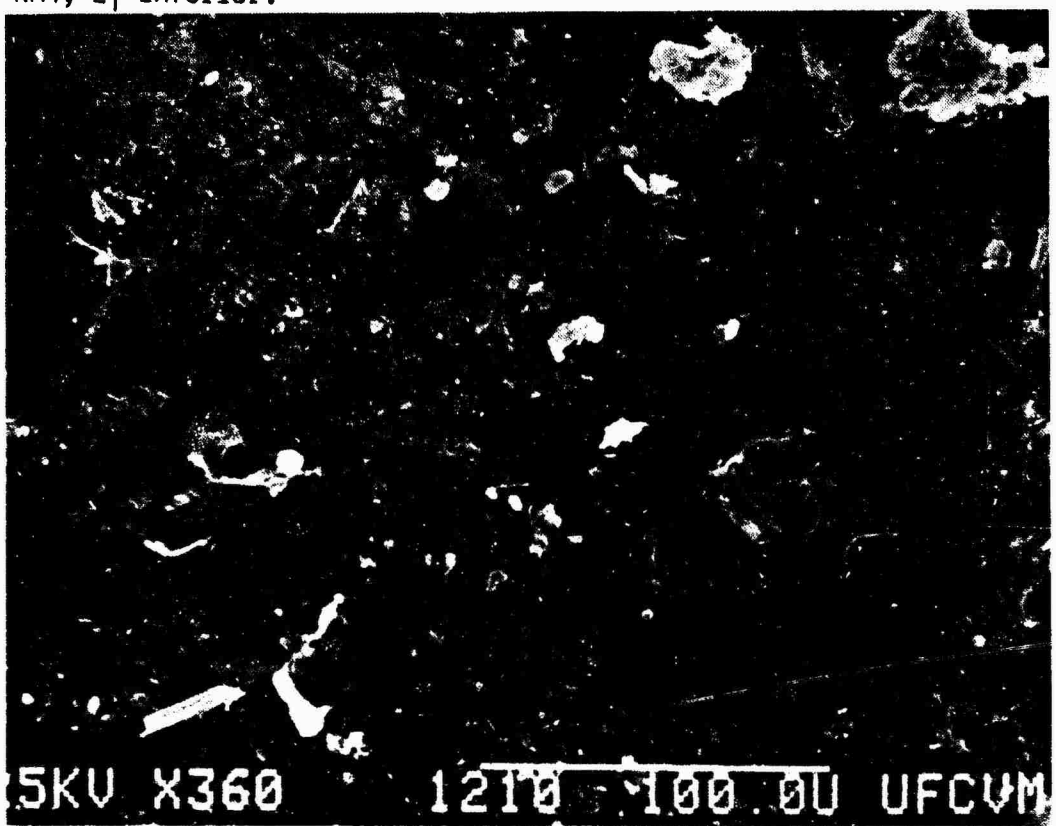

Figure 18. Higher magnification of joint surface shown in figure 17.

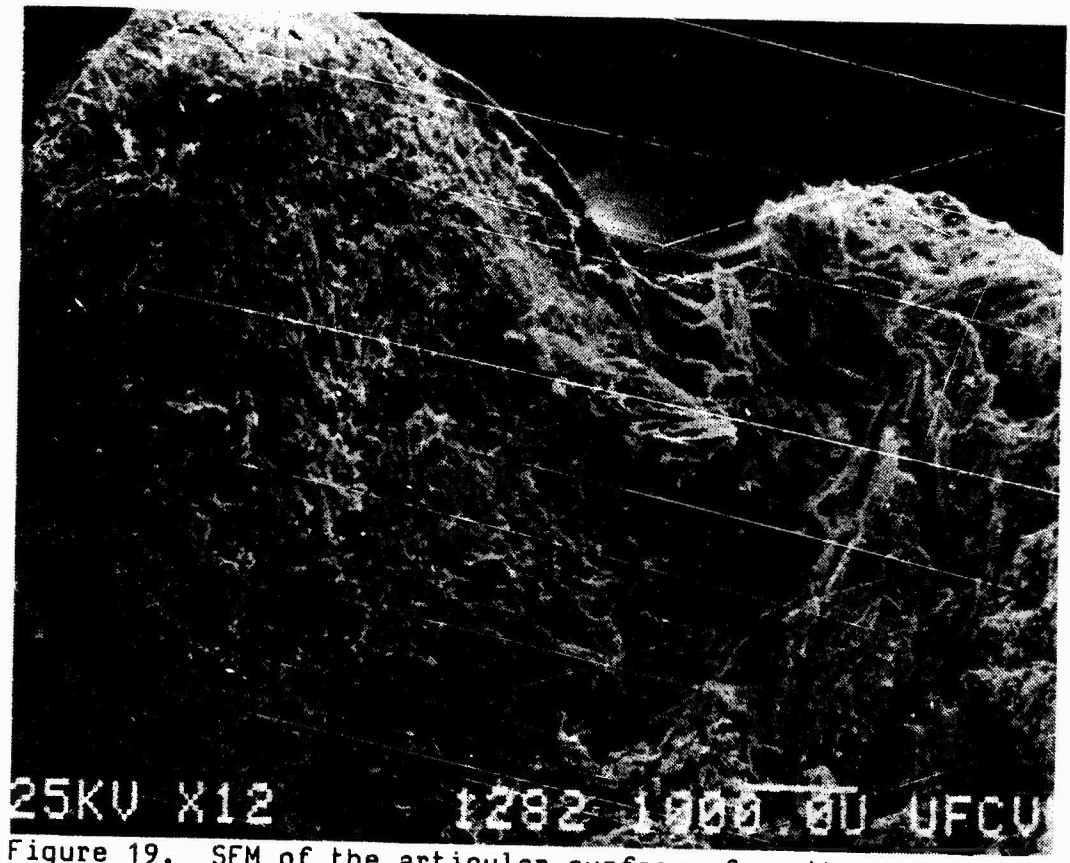

Figure 19. SEM of the articular surface of another zygapophysial joint. RM5, L_1 inferior.

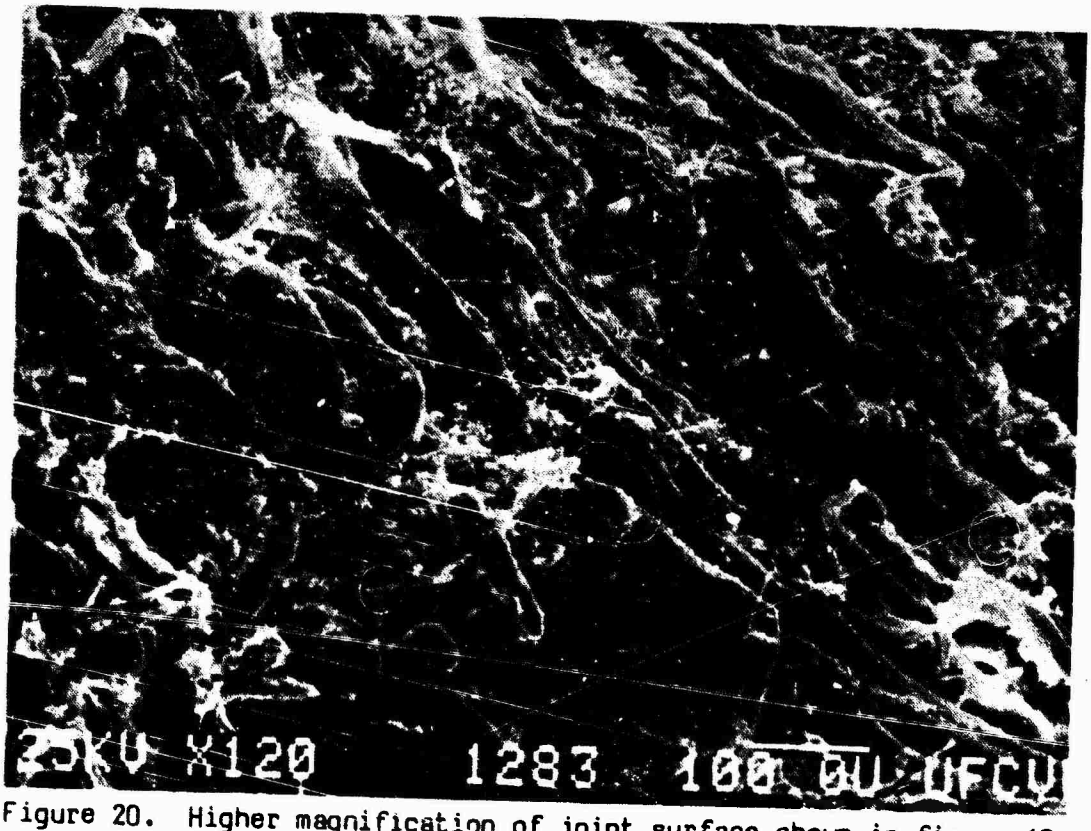

Figure 20. Higher magnification of joint surface shown in figure 19.

slight fibrillation and evidence of underlying chondrocytic lacunae indicating a thinned articular surface (figs. 21 and 22). Isolated cyst-like elevations were noted on some joint surfaces (fig. 23), and others had evidence of focal erosion (figs. 24 and 25).

Light Microscopy

Vertebral body. The vertebral body consisted of anterior and posterior cortices of dense bone. The exterior portion of the anterior cortex was composed of dense woven bone, while the interior portion was composed of lamellar bone (fig. 26). The woven and lamellar bone were separated by a basophilic cement line. The outer surface of the cortex was covered by a dense periosteum. The cells of the inner layer of the periosteum were surrounded by large, empty lacunar-like spaces (fig. 27).

The trabeculae in the center of the vertebral body were arranged in three zones, although the zones were not as obvious as with SEM. Trabeculae in the central zone were surrounded by elongated hemocytopoetic spaces, while the end zones had ovoid or square hemocytopoetic spaces. Overall, the trabeculae were shorter and more numerous in the end zones. Some trabeculae near the cartilaginous end plate had central cores of calcified cartilage. The trabeculae in the center of the body were composed of lamellar bone. The bony plate beneath the cartilage was perforated by several holes, such that bone marrow was in contact with the cartilage. Hemocytopoetic bone marrow was present in the spaces between trabeculae.

The cartilaginous end plate had three morphologic zones (fig. 28). The outer non-calcified zone consisted of hyaline cartilage. The chondrocytes were oval and flattened. There were two populations

Figure 21. SEM of the articular surface of a zygapophysial joint with evidence of underlying chondrocytic lacunae (arrow). RM4, L_2 inferior.

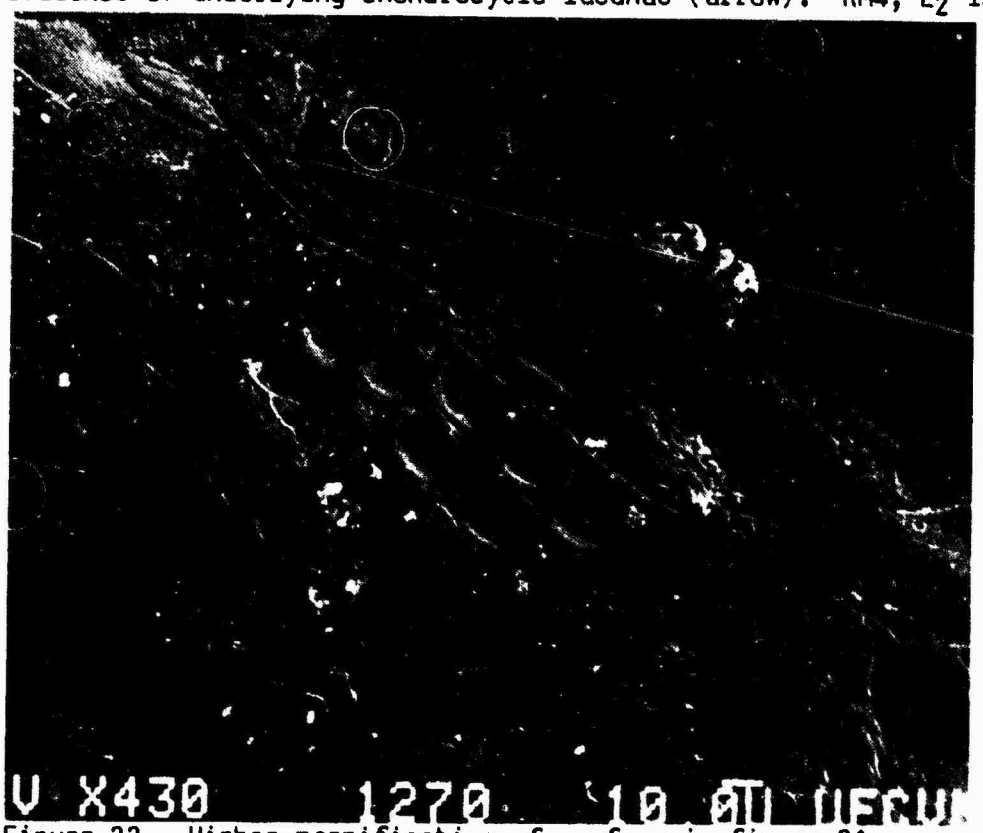

Figure 22. Higher magnification of surface in figure 21.

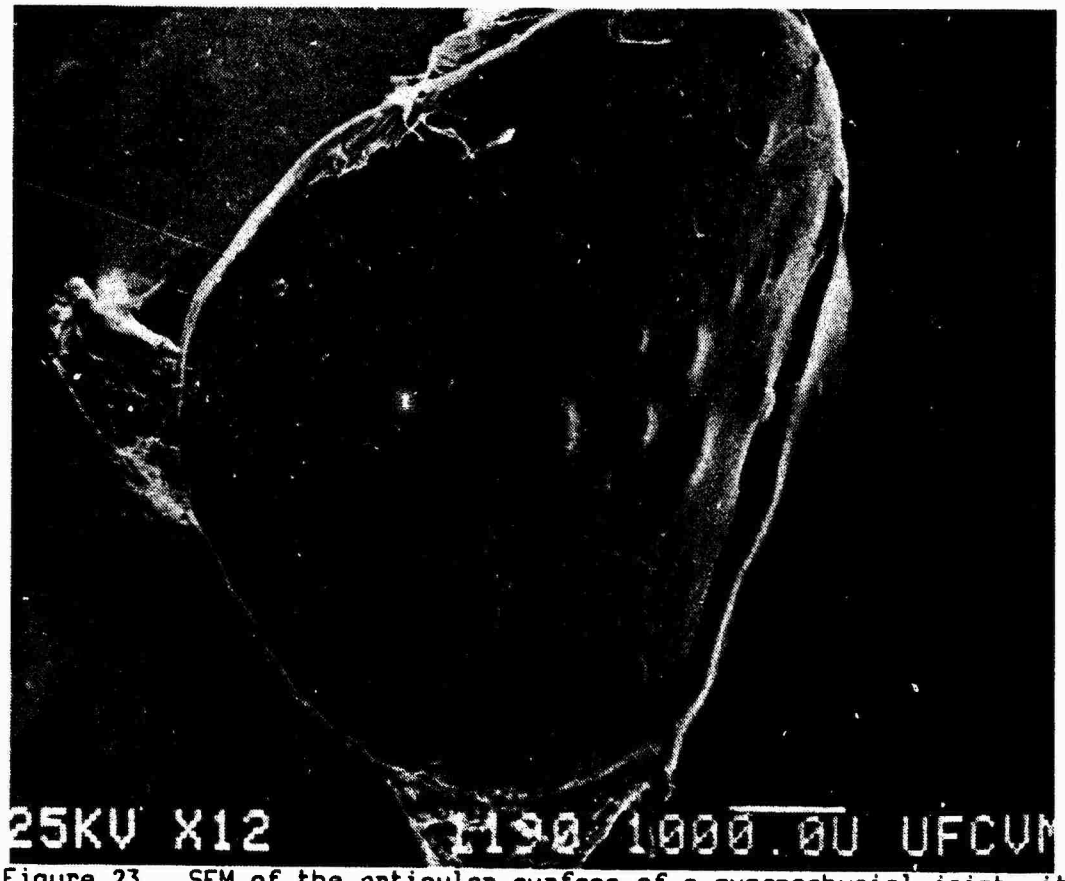

Figure 23. SEM of the articular surface of a zygapophysial joint with cyst-like elevations. RM4, L_6 inferior.

Figure 24. SEM of the articular surface of a zygapophysial joint with focal erosion. RM4, L_2 superior.

Figure 25. Higher magnification of eroded area indicated in figure 24.

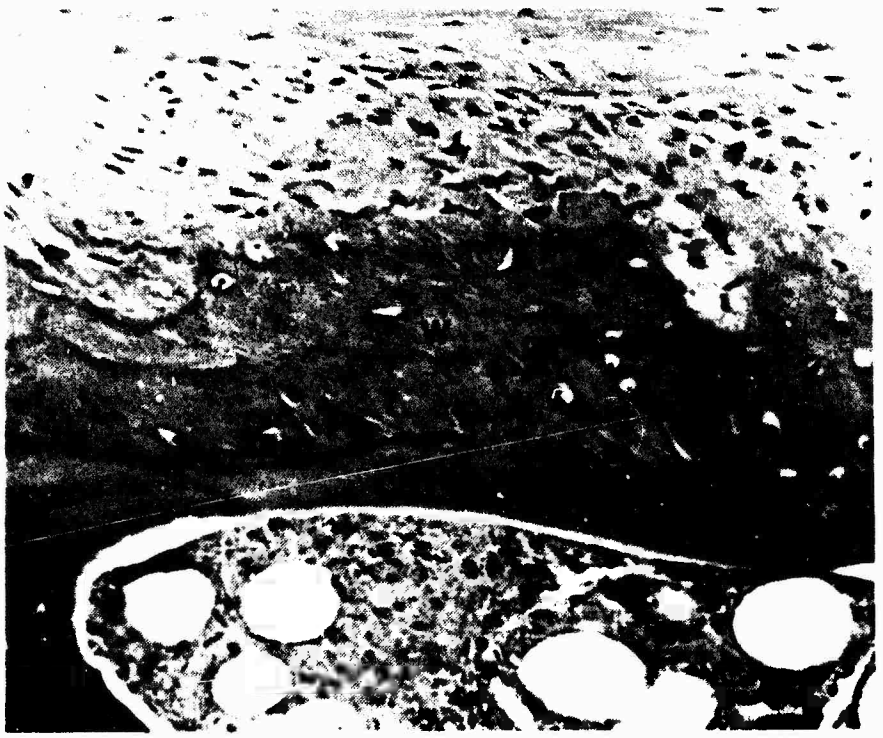

Figure 26. Anterior cortex of vertebral body. Outer bone is woven (W) while inner bone is lamellar (L). RM1, C_{6-T_3}.

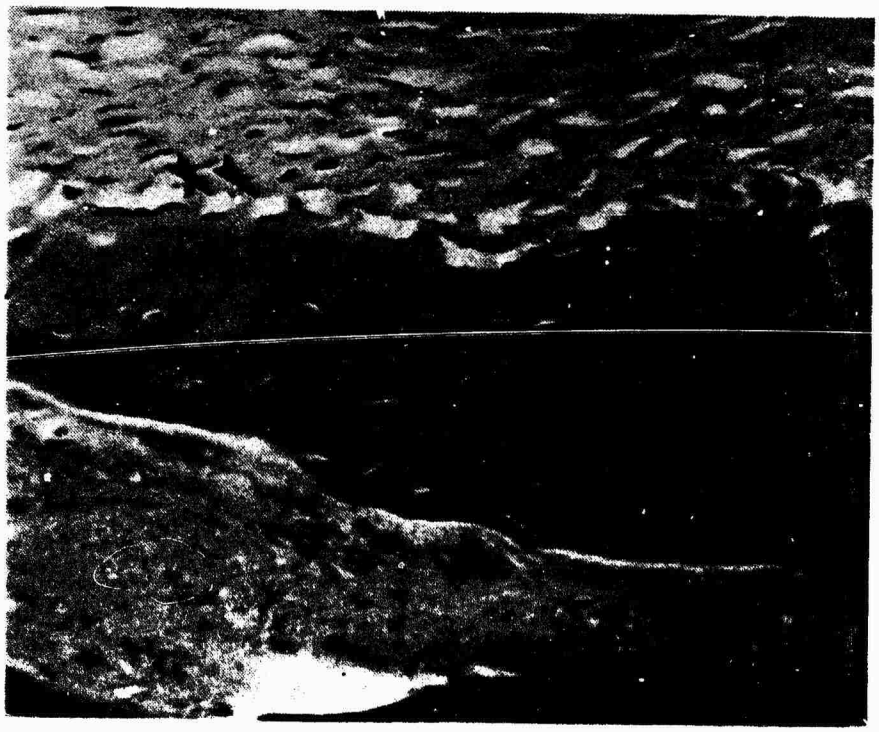

Figure 27. Cells of the inner layer of the periosteum of the vertebral body cortex which are surrounded by large lacunae (arrow). RM1, C_6-T_3.

Figure 28. The end zones of the cartilaginous end plate. 1=outer non-calcified cartilage; 2=calcified cartilage; 3=growth zone. RM1, C_{3-6}.

of cells present: 1. intensely PAS positive cells, and 2. alcian blue positive cells which were surrounded by an intensely alcian blue positive territorial matrix. This territorial matrix was also saffranin O positive. The interterritorial matrix was fast green positive and stained red with AB-VG. The non-calcified zone was approximately 0.06 mm thick.

The middle zone of calcified cartilage had islands of basophilic matrix surrounded by a lamina limitans (fig. 29). The islands were pale red to intense blue with AB-VG and red with SO-FG. Cells were absent from the islands, but they were present in the homogeneous matrix which surrounded the islands. The middle zone was approximately 0.50 mm thick, and it had bands of basophilic granules adjacent to the inner and outer zones.

The inner growth zone had a region of non-calcified cartilage (fig. 30). The outer area of non-calcified cartilage was relatively acellular, while the inner area had chondrocytes arranged in irregular columns. The cells were somewhat flattened in this region, and the matrix stained palely green with SO-FG or pink with AB-CG. The deeper portion of the growth zone had a calcified matrix which stained intensely blue with AB-VG or red with SO-FG. The cells were hypertrophied. Ossification gaps of basophilic lamellated matrix crossed the growth zone in scattered locations.

Scattered vertical columns of hyaline cartilage were noted in the cartilaginous end plate of some of the animals (fig. 31). The columns seemed to localize in the area of the nucleus pulposus, and they sometimes contained remnants of blood vessels.

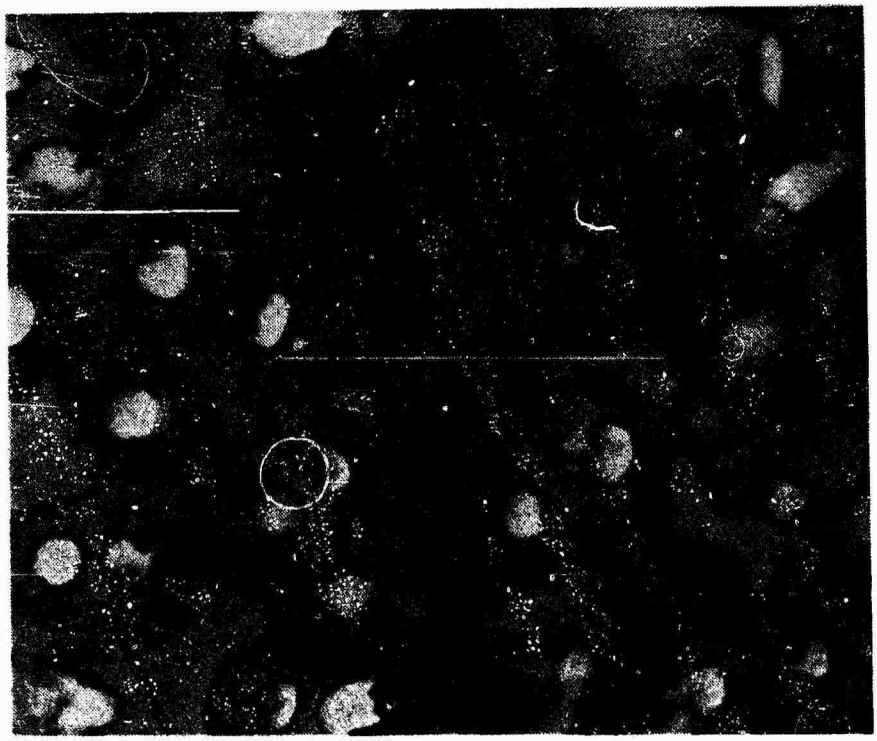

Figure 29. Higher magnification of calcified cartilage. M=island of mineralization; U=unmineralized cartilage; C=chondrocyte lacuna.

Figure 30. Higher magnification of growth zone. O=outer area of non-calcified cartilage; I=inner area of non-calcified cartilage; C=calcified cartilage; S=subchondral bone.

Figure 31. Vertical column of hyaline cartilage (arrow) traversing the cartilaginous end plate. RM2, L_{5-6}.

Trabecular bone of the annular epiphysis was present in RM2, RM4, and RM5 (fig. 32). The annular epiphysis was located in the anterior cartilaginous plate, and had started to fuse with the underlying trabecular bone of the vertebral body in some instances. In one animal (RM2) only one inferior annular epiphysis (L_6) was present, while in RM4 four interior (T_{10}, T_{12}, L_5, and L_6) and one superior annular epiphyses were present. The superior epiphysis of RM4 was present on L_7. RM5 had both inferior and superior annular epiphyses which were well developed throughout the lumbar region.

Intervertebral disc. The intervertebral disc consisted of a layered annulus fibrosus which was eosinophilic peripherally and basophilic centrally. Chondrocytes were scattered throughout the annulus between the layers of connective tissue.

The nucleus pulposus consisted of lightly basophilic amorphous material with scattered cells (fig. 33). The cells were oval and had an intensely stained cytoplasm. Frequently, clusters of cells were present.

Zygapophysial joint. The articular cartilage of the zygapophysial joint had three zones (fig. 34). The superficial zone consisted of scattered, round chondrocytes. The zone was approximately 0.4 mm thick, and a lamina splendens was present in the upper portion. The intermediate zone contained groups of 3 to 5 chondrocytes arranged in columns or clusters. The zone was approximately 2.0 mm thick. The columns of cells were vertically oriented in the center of the articular cartilage, but near the margins, the columns were angled toward the periphery. The deep zone of articular cartilage consisted of a superficial uncalcified region

Figure 32. The annular epiphysis of RM5, L_{3-4}.

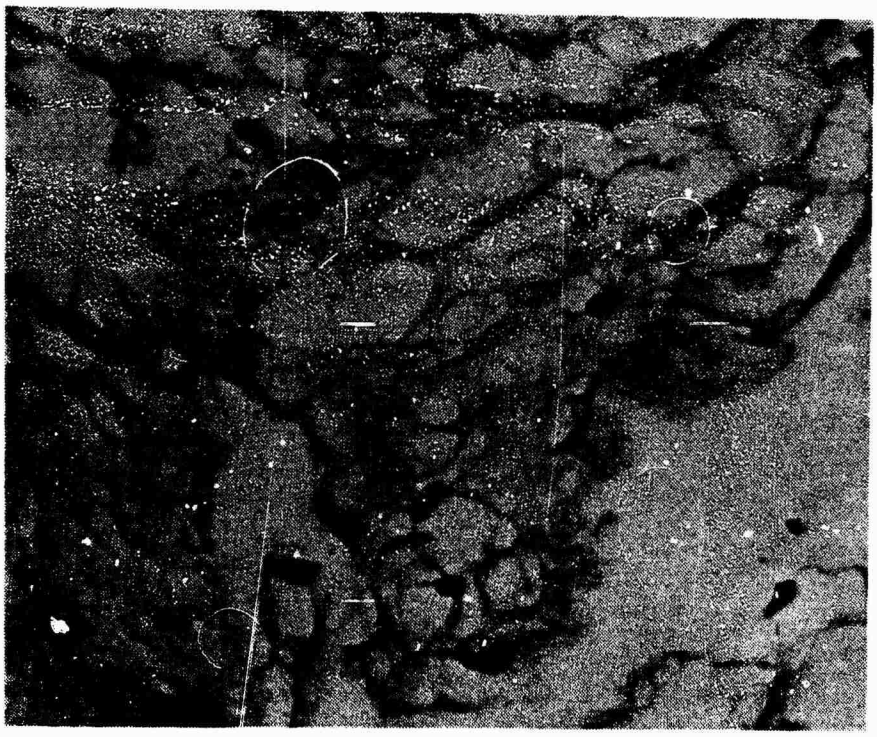

Figure 33. The nucleus pulposus of RM4, L_{2-3}.

Figure 34. The articular cartilage of the zygapophysial joint. S=superficial zone; I=intermediate zone; D=deep zone; T=tidemark. RM4, L_6 inferior.

similar to the intermediate zone, and approximately 1.0 mm thick. The deeper calcified region contained degenerating chondrocytes and a more intensely stained matrix. The calcified and uncalcified regions were separated by a basophilic tidemark. In some regions, multiple tidemarks were present. The articular surface had fibrillated areas in some samples.

Quantitative Histochemistry

The annulus fibrosus had high levels of keratosulfate and moderate levels of chondroitin sulfate (fig. 35). The outer non-calcified cartilage of the cartilaginous end plate had low levels of both chondroitin and keratosulfate. The calcified cartilage had moderate levels of chondroitin sulfate and low levels of keratosulfate. The growth zone had high levels of chondroitin sulfate and moderate levels of keratosulfate. Trabecular bone of the vertebral body had little, if any chondroitin or keratosulfate.

The growth zone of the end plate had significantly higher ($p<0.05$) levels of chondroitin sulfate when compared with the other regions analyzed. Bone had significantly less ($p<0.05$) chondroitin sulfate than the other regions.

The annulus fibrosus had significantly more ($p<0.05$) keratosulfate than the growth zone. When compared to the calcified and uncalcified zones, the growth zone was significantly higher in keratosulfate. All zones had more keratosulfate than bone.

In summary, the annulus fibrosus had higher concentrations of keratosulfate than chondroitin sulfate; the reverse was true in the

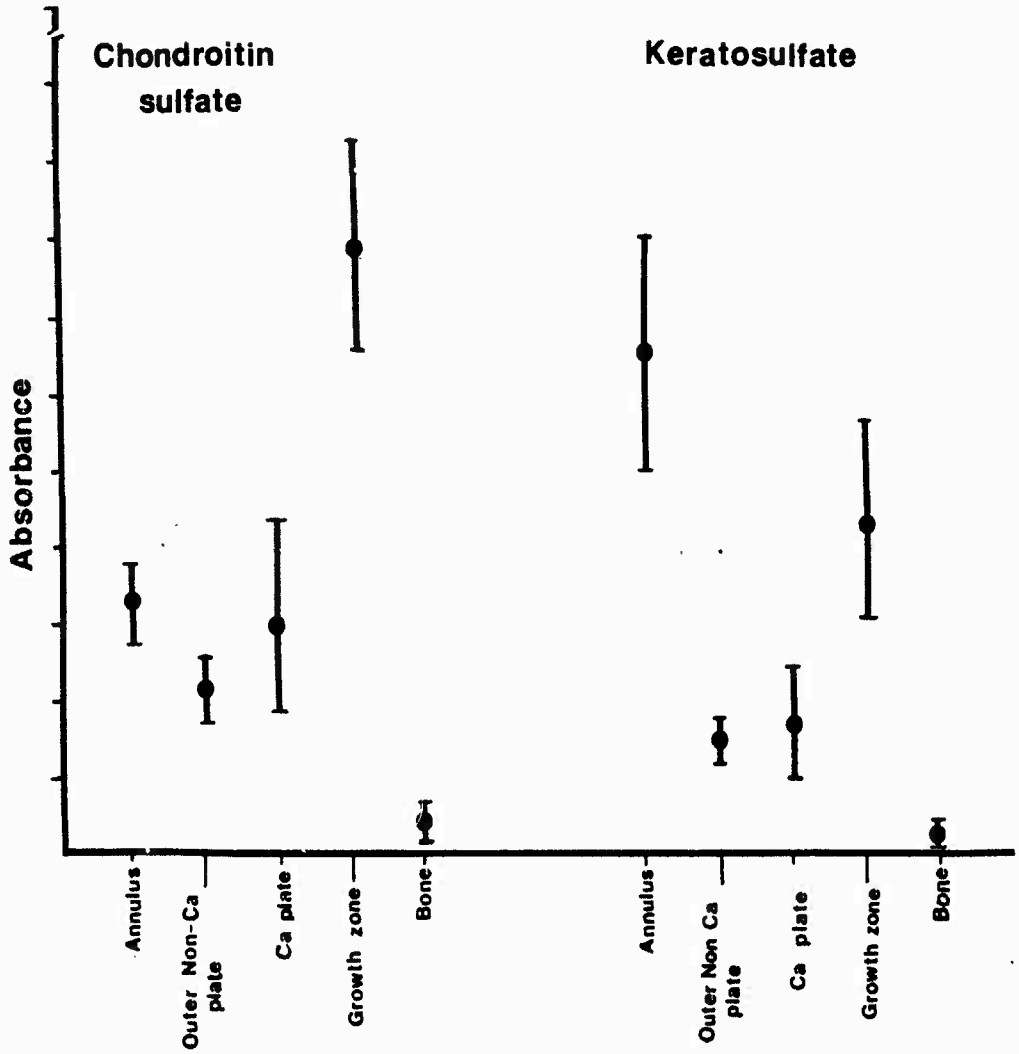

Figure 35. Graph of chondroitin and keratosulfate levels in the vertebral column of the rhesus monkey.

end plate area. Moving from the outer to the inner zones of the end plate region, the amount of chondroitin sulfate increases. The amount of keratosulfate also increases from the calcified to the growth zone.

In regard to variation between levels of the vertebral column, keratosulfate was significantly higher ($p<0.01$) in the thoracic and lumbar annulus fibrosus than in the cervical annulus. Chondroitin sulfate was significantly higher ($p<0.001$) in the calcified zone of the cervical region than in the thoracic region; the calcified zone of the thoracic region was higher than in the lumbar region.

Discussion

The radiology of the rhesus monkey vertebral column correlated with previously described gross anatomy of the rhesus monkey spine (Sullivan, 1969). The single observation of fusion of a zygapophysial joint was probably the result of a previous injury to RM5, and resulted in minimal impairment of vertebral column function such that the animal appeared normal until radiographed.

The innervation to the zygapophysial joints is as previously described by Stilwell (1956). Each zygapophysial joint has a dual nerve supply arising from two separate spinal nerves.

The vertebral body had features typical of a growing bone. The cortical bone was modeling by resorption of the endosteal surface to enlarge the marrow cavity as noted with SEM. The external cortical surface was forming new bone by intramembranous ossification. The osteogenic cells of the periosteum were surrounded by lacunae as they formed the osteoid of woven bone. This woven bone will eventually be remodeled to lamellar bone as observed nearer to the marrow cavity of the vertebral body. The body was increasing in length through growth at the cartilaginous end plate.

The zones of the trabecular bone were as previously described by Eurell and Kazarian (1982). This arrangement of trabecular bone allows the vertebral body to resist deformation by external forces. The majority of the forces from compression of the column are dissipated in the denser end zones of the vertebral body.

The bony end plate was perforated with holes as reported in other species (Calve and Galland, 1930). This perforation creates pathways for exchange between the bone marrow and the cartilaginous end plate.

The cartilaginous end plate of the rhesus monkey vertebral body is a unique structure. Based on this study, it is proposed that the end plate has three zones. The outer articular zone of uncalcified cartilage is located next to the intervertebral disc. The heterogenous population of cells in the outer zone suggests that one group of cells is actively producing sulfated mucopolysaccharides while the other is producing neutral mucopolysaccharides. Bernick and Cailliet (1980) have noted a shift toward the production of neutral mucopolysaccharides with ageing of the marmoset cartilaginous end plate in preparation for mineralization of this area. These two cell types may be related to this change in mucopolysaccharides.

The middle zone of calcified cartilage in the rhesus monkey vertebra does not exist in human vertebrae. The deep regions of the human articular zone may become calcified with ageing (Bernick and Cailliet, 1982; Coventry, 1945a), but a calcified pattern as seen in the rhesus monkey juvenile is not described. As the rhesus monkey has only an annular epiphysis, this middle zone of calcified cartilage may be a functional equivalent to the bony epiphysis of other species. Absence of this type of calcified cartilage in man is unexplained. The islands of calcification in the middle zone are surrounded by a lamina limitans which suggests that the mineralization process has arrested (Scherft, 1972). The unmineralized channels between the calcified islands provide a pathway for nutrients from the marrow cavity of the vertebral body to the unvascularized disc. Bernick, et al. (1980) describe calcification of marmoset cartilaginous end plates. The six-month-old marmoset end plate strongly resembles the rhesus monkey end plates in this study. The areas of collagenous

fibers in the intercellular matrix correspond to areas of calcified cartilage in the rhesus monkey. The cement line described by Bernick, et al. (1980) as separating the intercellular matrix from the lacuna is probably the lamina limitans which surrounds the calcified cartilage of the rhesus monkey.

The growth zone was as described for other species such as the marmoset (Bernick, et al., 1980) and the mouse (Higuchi, et al., 1982). The cartilage of this zone undergoes endochondral ossification to form the bone of the vertebral body.

All rhesus monkeys in this study were close to skeletal maturity, therefore it remains to be determined what happens to the cartilaginous end plate with ageing. Bernick, et al. (1980) stated that the mineralized articular cartilage of the marmoset is resorbed by osteoclastic activity leaving a thin layer of cartilage which separates the disc from the underlying bone in the 10 year old animal. The rhesus monkeys in this study were not old enough to have thinning of the articular zone as growth zones were still present. Higuchi, et al. (1982) have described ossification of the deep articular zone in the mouse. This ossification represents formation of a complete bony epiphysis in the mouse, a structure which is not present in the rhesus monkey. Nussbaum (1981) describes progressive ossification of the rhesus monkey end plate, but frontal sections of the cartilaginous end plate are not convincing; the example shown may well be a section through the anterior portion of the annular epiphysis which does extend completely across the vertebral body at that location. Further studies are indicated to determine if, with ageing, the middle zone of calcified cartilage and is resorbed as proposed by Bernick, et al.

The vertical columns of cartilage which occasionally surrounded blood vessels were probably remnants of embryonic blood vessel pathways. These structures and the ossification gaps of the growth zone of the end plate may be biomechanically weak areas of the vertebral column as suggested by other workers (Schmorl and Junghanns, 1959; Harris and Macnab, 1954).

The annular epiphysis has been previously reported in humans, orangutans, gorillas, and marmosets (Schmorl and Junghanns, 1959; Bernick, et al., 1980). The annular epiphysis of the rhesus monkey seems to appear close to skeletal maturity, and forms in the lumbar and lower thoracic vertebrae first. Appearance of the inferior epiphysis seems to precede the superior epiphysis. The epiphysis fuses with the trabecular bone of the vertebral body. Schmorl and Junghanns (1959) indicate that union of the annular epiphysis with the vertebral body takes place last in the lumbar segments. A pattern of fusion at specific levels could not be established in the juvenile rhesus monkeys of this study.

The intervertebral disc of the rhesus monkey was like that previously described for other species. Only one cell type was observed in the disc. Fragments of bone and cartilage in the disc were probably artifacts due to sawing.

Innervation of the rhesus monkey zygapophysial joint as described by Stilwell (1956) was confirmed in this study.

The articular cartilage zones were as previously described in other species such as the human (Lewin, 1964). Variation in the articular surface of the zygapophysial joints indicates that a wide range of cartilage degeneration can be present in a clinically normal

animal. Since these joints are apparently degenerating, and the animals are juveniles, it raises questions as to the cause of the degeneration, and the long range health of the vertebral column.

THE RESPONSE OF THE PRIMATE VERTEBRAL COLUMN TO COMPRESSIVE LOADING

Introduction

The vertebral column consists of vertebrae, intervening intervertebral discs, posterior zygapophysial joints, and associated ligaments. The column provides support for the body trunk, protection for the spinal cord, and an attachment for ribs and muscles. The anterior portion of the column is composed of vertebral bodies and intervertebral discs. Anatomically, the vertebral body is primarily trabecular bone surrounded by a collar of compact bone (Kazarian, 1978). The trabecular bone is organized into a central zone and two adjacent end zones on the basis of morphology. The end zones are porous allowing diffusion of nutrients from the body into the disc. Between the cartilaginous plates are an outer annulus fibrosus and an inner nucleus pulposus. The nucleus pulposus contains collagenous fibers in a mucopolysaccharide gel (Coventry, 1969). The anterior portion of the column is, by nature of its structure, more compressible than the posterior part of the spine (Kazarian, 1978). Therefore, the response of the anterior column is of primary interest in the initial modeling of compression injuries.

Response of a spinal unit (two intact vertebrae plus the intervening disc) to forces of different magnitudes and direction has been reported at the gross and radiographic levels (Roaf, 1960). Under vertical compression, the annulus bulges initially. The end zones of the body deform, forcing blood out of the cancellous bone. With increasing pressure, the end zones crack and nuclear material

enters the vertebral body. In general, the intact disc is more resistant to vertical compression than the vertebral body.

Injury patterns reported in aircrewmen in association with emergency egress from military aircraft include vertical compression injuries, but hyperflexion and/or hyperextension may also occur and alter the injury pattern. Classified on an anatomical, kinesiologic, and pathologic basis, the vertebral body fracture patterns may be grouped as follows:

1. anterior wedge compression fractures
2. posterior height compression fractures
3. combined anterior wedge/posterior height compression fractures
4. burst injuries

Anterior wedge compression fractures are associated with column hyperflexion while posterior height compression fractures are associated with column hyperextension. Combined fractures are the result of hyperflexion and hyperextension acting in sequence. Burst injuries occur when loading is applied with minimum angulation (Kazarian, 1978).

The purpose of this study was to further evaluate and characterize the response of the primate vertebral column to compression loading. Isolated vertebral bodies, isolated spinal units, and intact vertebral columns in vivo were studied following loading with radiology, light microscopy, scanning electron microscopy, and polarizing light microscopy.

Compression of the Isolated Vertebral Body

Introduction and Literature Review

The vertebral body is a cylindrical structure composed of a lateral wall of cortical bone surrounding a central core of cancellous bone. The cancellous bone in the vertebral body is reinforced by the intimate association of crystals and fibers in its structure. The collagen fibers present in cancellous bone can be stretched with difficulty, whereas the hydroxyapatite crystals are stiff. Moreover, there are strong bonds between the fibers and crystals which make the combination of the two more resistant to deflection of deformation than either would be in isolation.

The macroscopic overall trabecular pattern within the body resembles a three-dimensional latticework. When viewed in sagittal section, the body is composed of three regions: cranial end zone, central zone, and caudal end zone (fig. 36). The trabeculae are fine and the marrow spaces regular and relatively small in the end zones. Each end zone extends about 20% of the body length (Arnold, 1970). The central zone occupies the remaining 60% of the body length and contains coarser trabeculae. The marrow spaces are larger and more irregular toward the mid-section of the body. Secondary horizontal trabeculae provide support and thereby stabilize the primary vertical trabeculae. This arrangement of trabecular bone allows resistance of the vertebral body to deformation by external forces.

The blood supply to the vertebral body is via the segmental artery (Parke, 1975). The segmental artery branches to form several nutritional vessels which perforate the bony cortex and course through

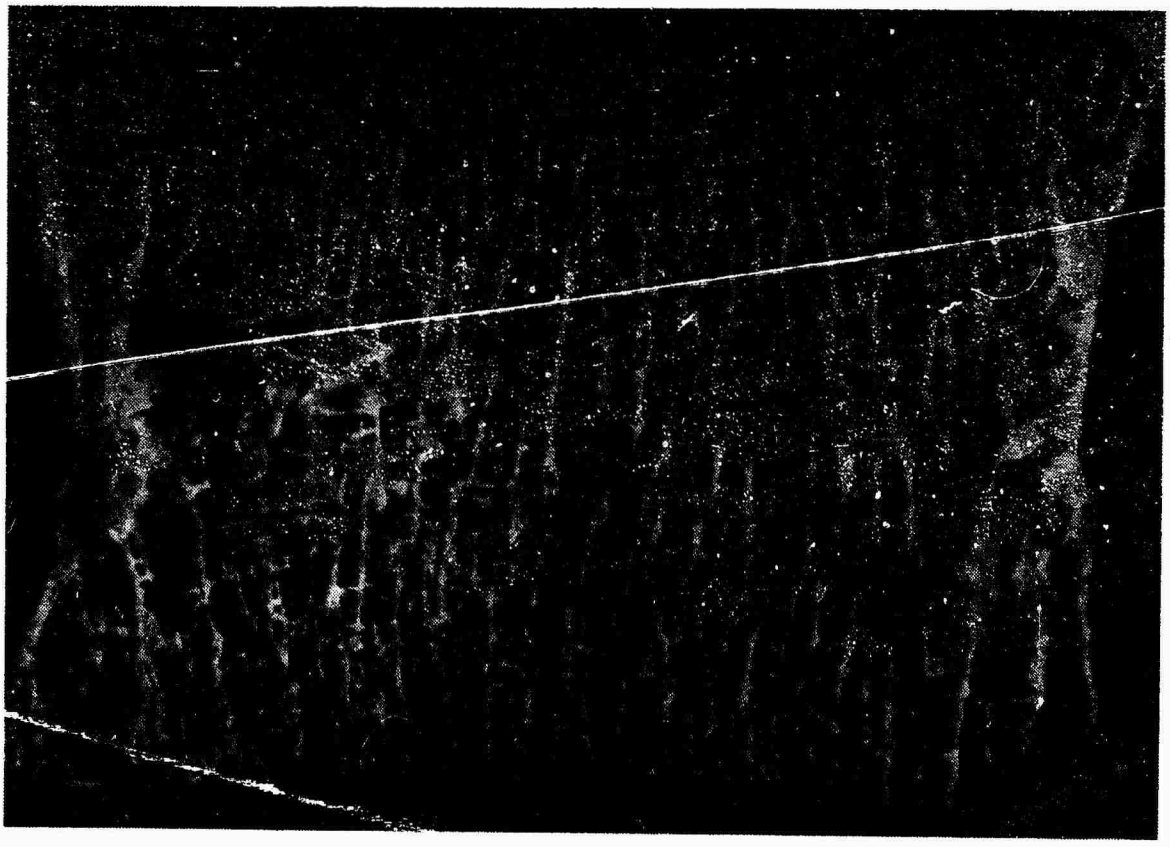

Figure 36. Photograph of a sagittal section through a vertebral body showing the cranial end zone (A), central zone (B), and caudal end zone (C). Area of exit of basivertebral vein through mid-dorsal cortex is present at D.

the mid-section of the vertebrae. The vascular channels converge toward the basivertebral vein which exits along the mid-dorsal surface of the body.

Scanning electron microscopy has been used to study the structure of normal human lumbar vertebral bodies (Whitehouse, et al., 1971). The morphology is similar to that previously described by gross observation. The trabecular bone of the end zones is arranged in short cross-braced columns with small spaces between as if it were designed for strength and rigidity. The central region contains larger marrow spaces bordered by thinner trabeculae.

Vertebral bodies have been shown to regain 76% of their original height within 72 hours following mechanical compression of up to 50% of their original height (Kazarian and Graves, 1977). In this study, scanning electron microscopy was used to determine the effect of compression at different displacement rates on the structure of trabecular bone in vertebral bodies.

Materials and Methods

A total of forty nine rhesus monkey, baboon, and human vertebral bodies were dissected, and the posterior aspects removed leaving the vertebral body intact. The samples were radiographed in the anterior-posterior position, measured, and divided into sub-groups for compression testing (Table 1). The vertebral bodies were mounted in dental acrylic and machined to insure uniform loading (fig. 37). A high performance electro-hydraulic closed-loop test system (Model 810 Material Test System, MTS Systems Corporation, Minneapolis, Minnesota) was used to compress each sample (fig. 38). With the machine in the displacement control mode, a linear ramp function was used to strain each test specimen. The ultimate ram displacement (specimen deformation) was set at 50% of the original specimen height. The strain rates are indicated for each sample in Table 1. All samples were compressed in a cranial to caudal direction. The imposed time dependent displacement and resultant compressive loads were measured and recorded. Included as part of the test system was a linear variable differential transformer. Ram displacements were measured by the linear variable differential transformer while the specimen reacted against a four arm bridge strain gauge load cell located above the specimen. A multi-channel FM magnetic tape recorder (Model 392A, Electro-Mechanical Research, Inc., Sarasota, Florida) and a multi-channel transient recorder were used to store test results. Load and displacement data were recorded directly on a recorder (Hewlett-Packard Model 136A recorder, Hewlett Packard, Inc., San Diego, California) for the low speed tests, but for the intermediate and high speed tests the data were stored in the digital memory of the

Table 1. Heights of recovered and unrecovered vertebral bodies.

Sample number	Compression rate(m/sec)	Original height (mm)	Recovered height (mm)	% of original height recovered
GROUP I				
1				
2		Control animals - no measurements taken		
3				
4				
Y304L6	8.89×10^{-3}	17.6	15.2	86
Y304L4		17.7	15.1	85
134BL5		21.3	broken	-
134BL3		19.0	14.5	76
230AL7		17.7	15.5	88
230AL5		20.8	broken	-
Y44L3		22.1	19.0	86
Y44L5		25.3	20.1	79
Y44L7		18.7	16.0	86
SERGT5		19.5	14.1	72
			mean	82
SERGT7	8.89×10^{-1}	24.8	17.9	72
ANTLT6		28.4	22.1	78
Y44L6		22.7	17.6	78
230AL4		20.1	15.6	78
Y304L3		17.3	13.3	77
Y304L5		17.9	14.	81
Y304L7		16.0	13.3	83
230AL6		20.3	broken	-
598AL7		18.1	15.8	87
134BL6		20.8	16.4	79
			mean	79

GROUP II		Unrecovered height	Recovered height	% difference in recovered vs. unrecovered
Baboon				
F54L1	8.89×10^{-5}	11.0	12.0	9%
F12T11		10.0	10.0	0
F50L6		15.0	16.5	10
F52T13	8.89×10^{-3}	12.5	13.5	8
F10L2		14.5	14.0	-3
F62L5		17.5	19.0	9

F50L5	8.89×10^{-1}	14.5	15.0	7
F52T11		9.5	11.0	16
F04L2		14.0	14.5	4
F62L7		14.5	15.0	3
Rhesus monkey				
F08T12	8.89×10^{-5}	12.0	13.0	8
F08L2		19.0	20.0	5
F08L3		21.0	22.5	7
F08L6		22.0	23.0	5
F08L7		22.0	22.0	0
F60T10		12.5	13.5	8
F60T11		15.0	16.5	10
F60T12		17.0	18.0	6
F60L2		20.0	21.0	5
F60L3		22.0	21.0	-5
F60L5		25.0	26.5	6
F60L6		23.5	25.0	6
F08L4	8.89×10^{-1}	21.5	25.0	5
F088L5		21.0	22.0	5

Figure 37. Vertebral body with dental acrylic end plates in place.

Figure 38. High performance electro-hydraulic closed loop test system used to compress samples.

transient recorder for playback at reduced speeds into the X-Y recorder. The FM tape recorder was used as a back-up recorder on the high speed tests. In this manner, a hard copy record of specimen loads and deformation was obtained for each test. A typical test curve drawn by the X-Y recorder is shown in figure 39. The test specimen load is plotted on the ordinate versus ram displacement on the abscissa. Four dependent variables (ultimate load, deformation to ultimate load, stiffness, and energy to ultimate load) were extracted directly from the test curves. The first point on the load deformation test curve following the elastic section where a tangent to the curve becomes parallel to the deformation axis of the plot (abscissa) was defined as the ultimate load. The deformation at this point was defined as the deformation to ultimate load. The test specimen stiffness was determined by fitting the linear elastic section of the load deformation test curve with a least squares linear fit curve. The energy to ultimate load was defined as the area under the load versus deformation test curve from the point of zero deformation up to the ultimate load.

During the compression process, high speed photography was used to record vertebral response (fig. 40). Upon deloading, the samples were placed in a plexiglas jig (Group I-fig. 41) or an aluminum plate jig to prevent recovery until post-compression radiology was completed.

Group I samples were sawed in half in an anterior to posterior direction. The right half of the body was placed in compression while the left half was allowed to recover for 72 hours above saline in a sealed jar.

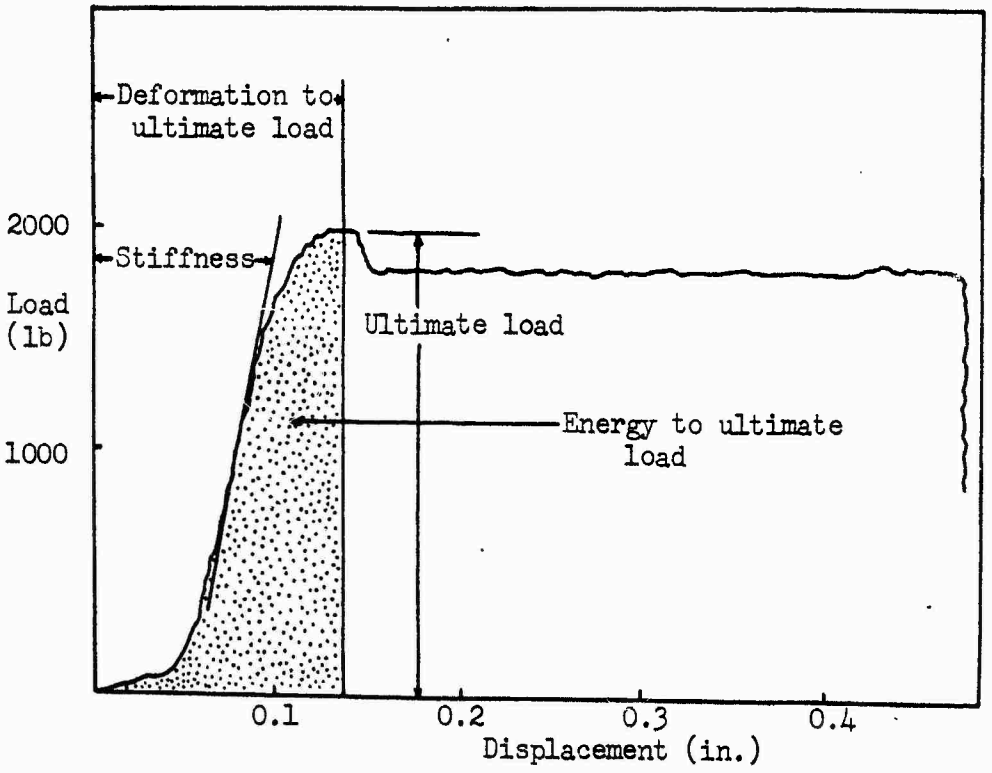

Figure 39. Typical test curve resulting from compression of a vertebral body.

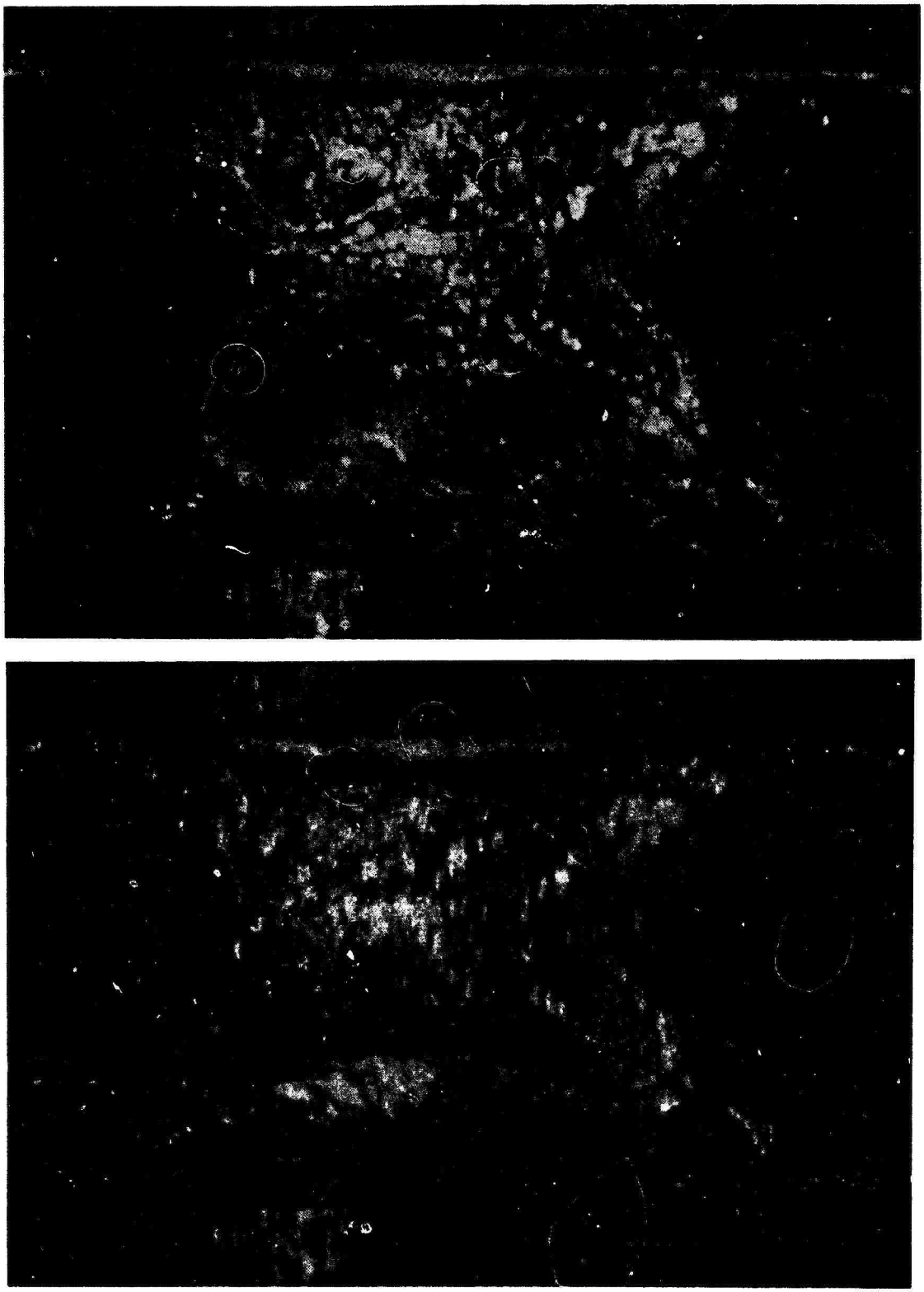

Figure 40. A series of four photographs of vertebral body reaction to loading at 8.89×10^{-1} m/sec (frame rate=1500 frames/sec).

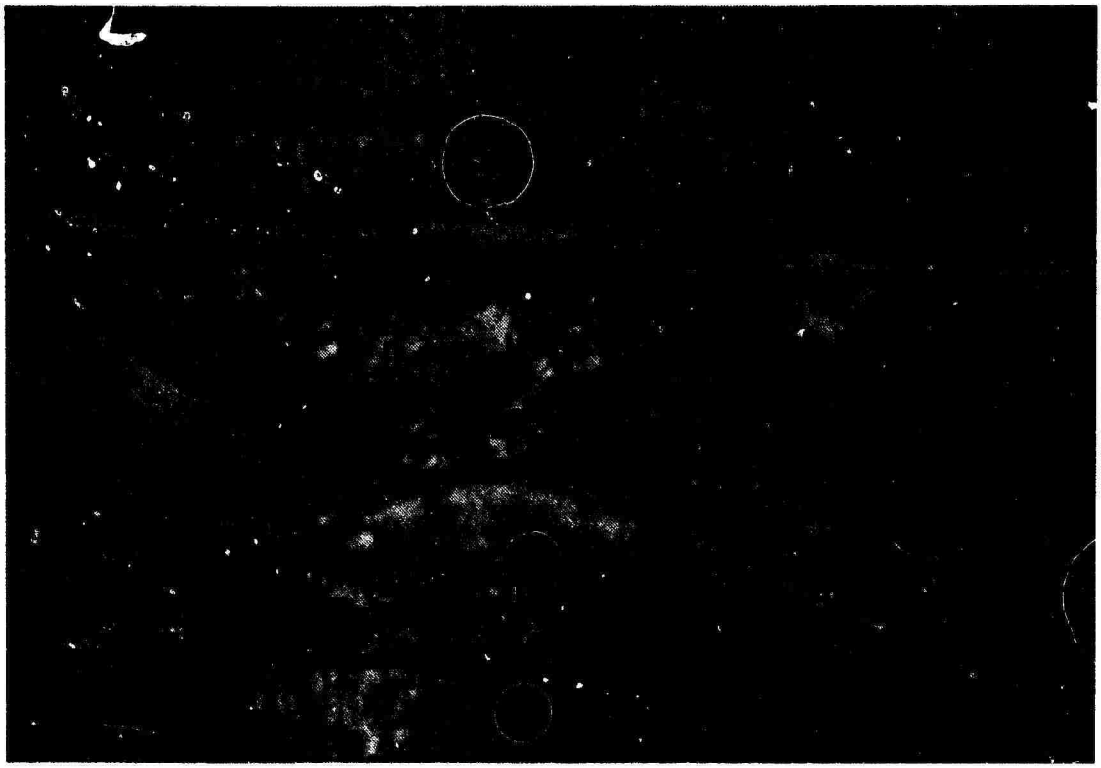

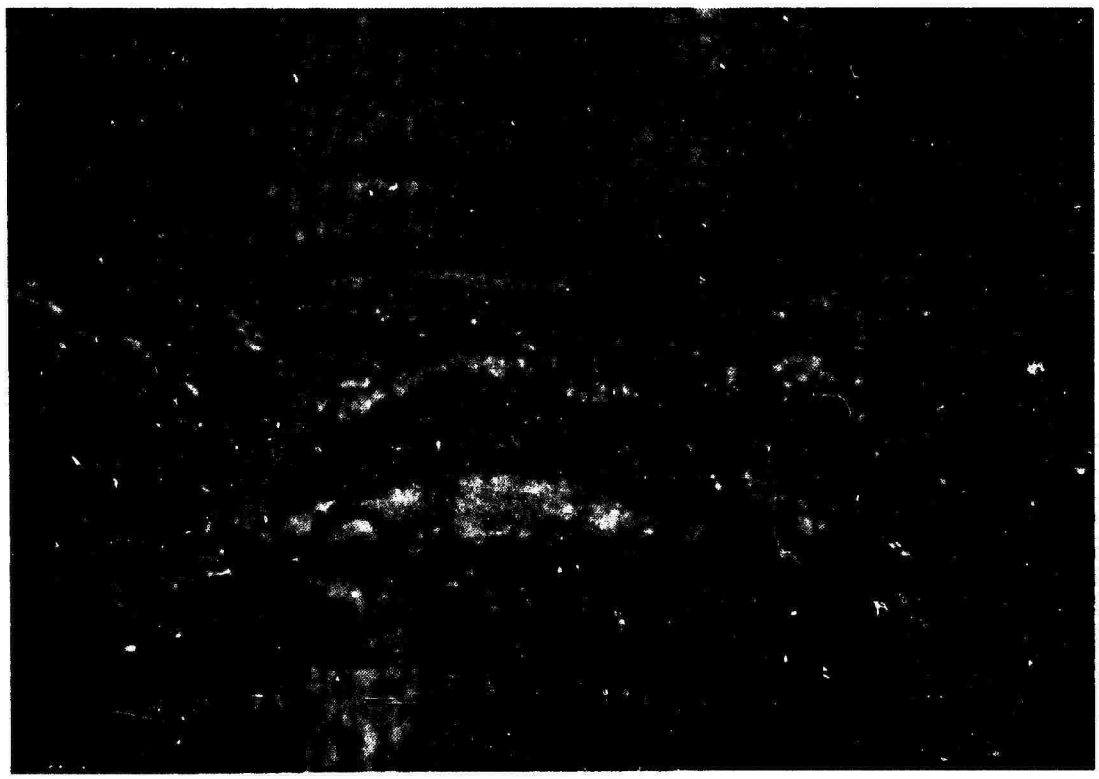

Figure 40 (cont'd)

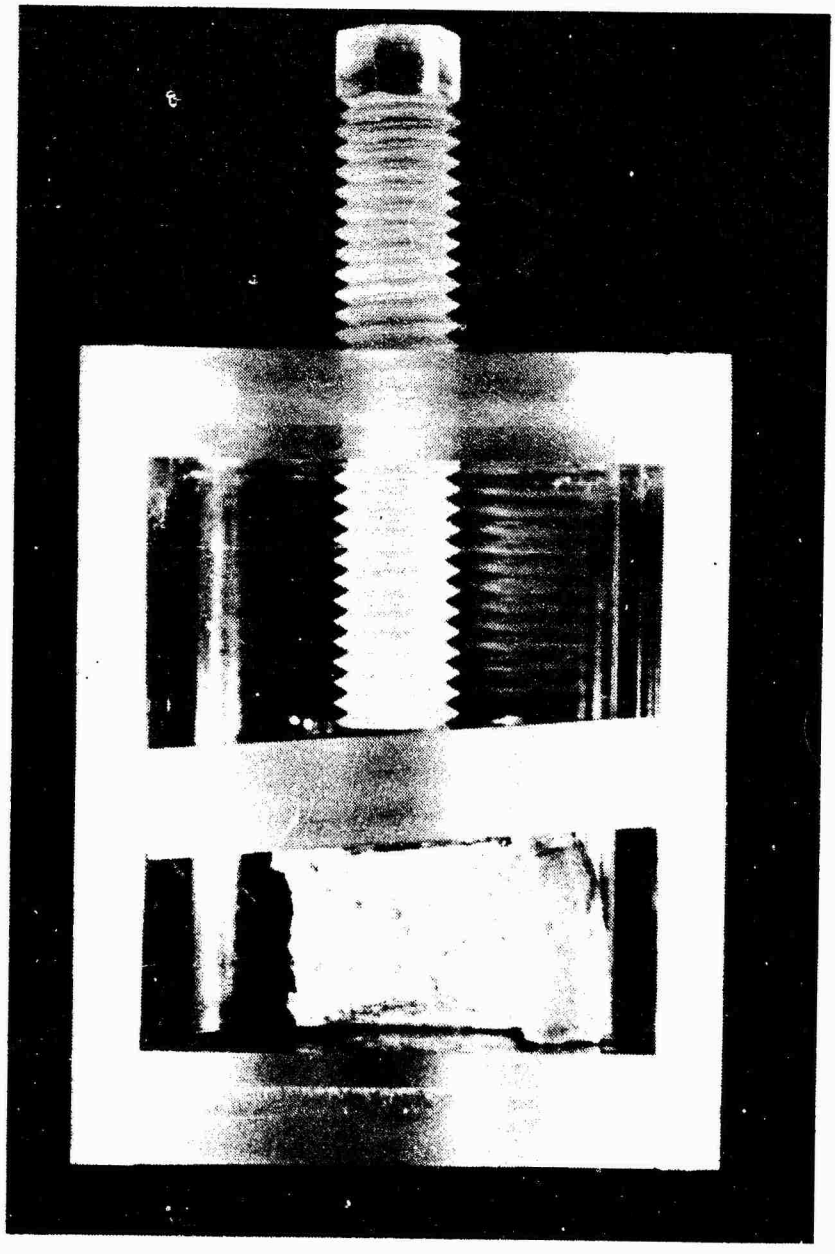

Figure 41. Plexiglas jig used to prevent recovery of samples.

Group II samples were held in compression by the aluminum plate jigs, frozen, and shipped to the investigator. The samples were subdivided into two additional groups for sectioning either laterally or anterior-posteriorly (fig. 42). One half of the body was allowed to recover outside the jig for 24-48 hours while the other half was fixed in 10% neutral buffered formalin.

All samples were measured at the end of the recovery period (Table 1), and then further divided for scanning electron microscopy and histochemistry. All samples were fixed in 10% neutral buffered formalin.

Samples for scanning electron microscopy were etched by a modified Boyde technique to remove hemocytopoetic tissue (Boyde, 1972), and then post fixed by the thiocarbohydrazaide-mediated osmium binding method (OTO) to reduce charging (Kelley, et al., 1975). A coating of gold-palladium was also utilized to reduce charging following critical point drying. Samples were scanned at 15 kV in a scanning electron microscope.

Histochemical samples were divided into a section for routine decalcification, embedding, and sectioning and a section for plastic embedding and grinding. Six micrometer routine sections were stained with hematoxylin and eosin, toluidine blue O, Gomori's silver stain, or alcian blue methylation/saponification (pH 2.5). Hematoxylin and eosin were chosen as routine morphologic stains, toluidine blue O to demonstrate collagen, Gomori's silver stain to demonstrate reticular fibers, and alcian blue methylation/saponification to identify and separate chondroitin sulfates and keratosulfate. Undecalcified

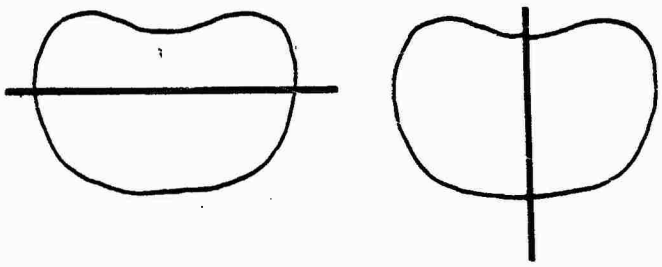

Figure 42. Diagram of sample sectioning.

sections to be ground were embedded in butoxyethanol glycol methacrylate and shipped to Roberts Petrographic Section Service for further processing.

Results

Control group. The trabeculae in the central zone of the control animals were long, narrow and mostly vertical in orientation (fig. 43). They were separated by large marrow spaces that were elongate in shape. Trabeculae of the end zones were thicker and shorter than those found in the central zone (fig. 44). Vascular spaces were round or slightly oval in shape. Scattered small cracks were apparent in the matrix surface of the control samples. Osteocytic lacunae and numerous canaliculi opening on the trabecular surface could also be observed.

Group I - 8.89×10^{-3} m/sec. Samples were primarily deformed in the caudal central zone. The long trabeculae of the central zone underwent S-shaped bending (figs. 45, 46 and 47) with laminar separation, cracks, and fractures apparent at higher magnification (figs. 48-51). In both cranial and caudal end zone regions, trabeculae were relatively normal in appearance except for occasional scattered fractures of horizontal trabeculae (fig. 52) and some evidence of slight S-shaped bending of vertical trabeculae. Recovered samples in this group regained 82 per cent of their original height. The appearance of recovered samples was the same when compared to samples held in compression, except that hemocytopoetic spaces in the central zone were larger and trabeculae were further apart.

Group I - 8.89×10^{-1} m/sec. Overall, samples in this group were more severely deformed than the previous group (8.89×10^{-5} m/sec strain rate). Numerous fractures were present (figs. 53 and 54). Trabeculae were compressed closer together and the

Figure 43. SEM of the central zone of a control vertebral body. 80X.

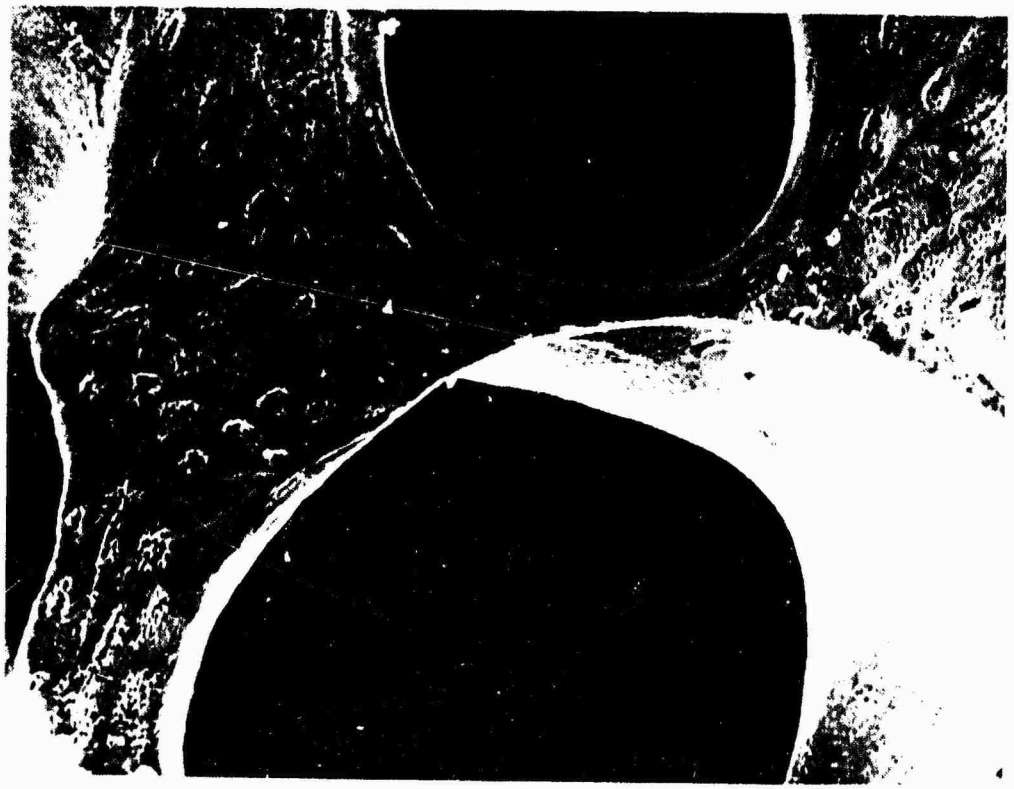

Figure 44. SEM of the end zone of a control vertebral body. 200X.

Figure 45. SEM of the central zone of a vertebral body compressed at 8.89×10^{-3} m/sec. 80X.

Figure 46. SEM of the central zone of a body compressed at 8.89×10^{-3} m/sec showing S-shaped bending of trabeculae. 55X

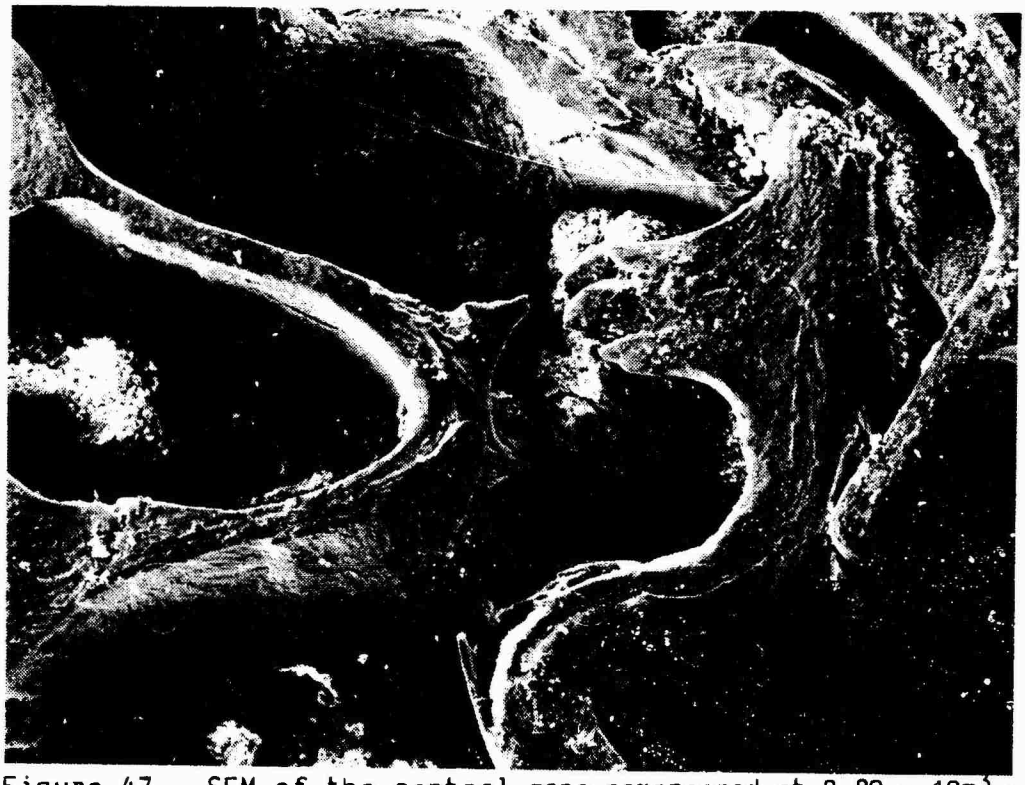

Figure 47. SEM of the central zone compressed at 8.89×10^{-3} m/sec showing S-shaped bending of trabeculae. 55X.

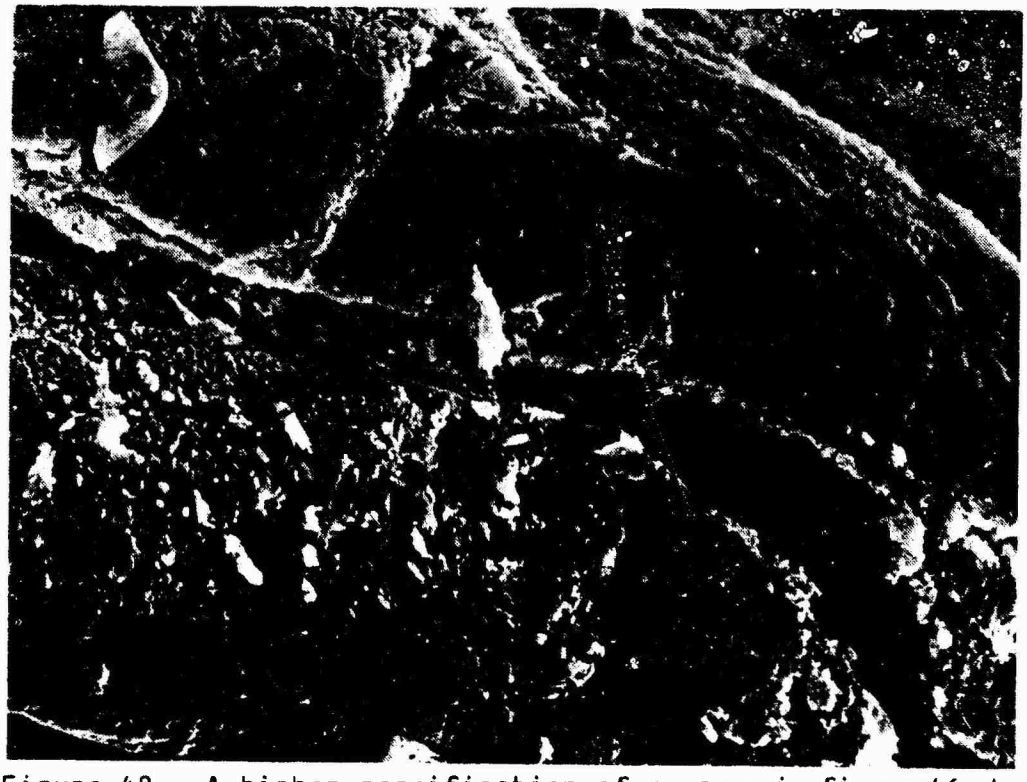

Figure 48. A higher magnification of an area in figure 46 showing laminar separation. 540X.

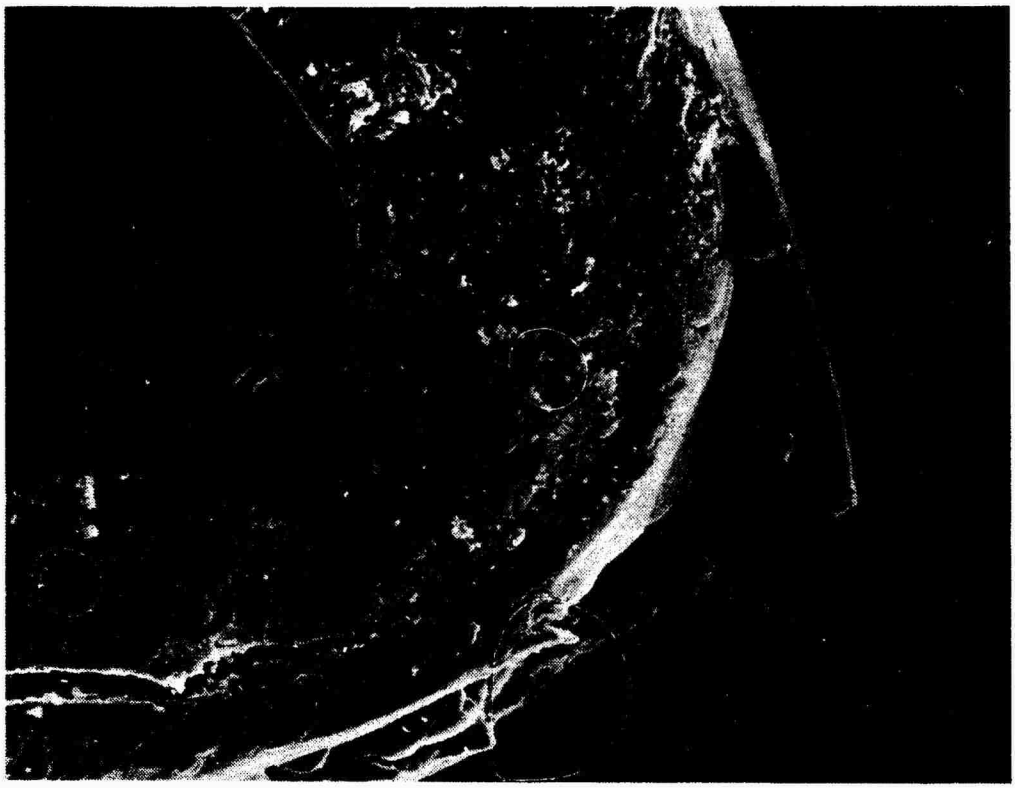

Figure 49. A higher magnification of an area in figure 47 showing laminar separation and fracture. 200X.

Figure 50. SEM of a trabecula in the central zone showing bending and laminar separation. 200X.

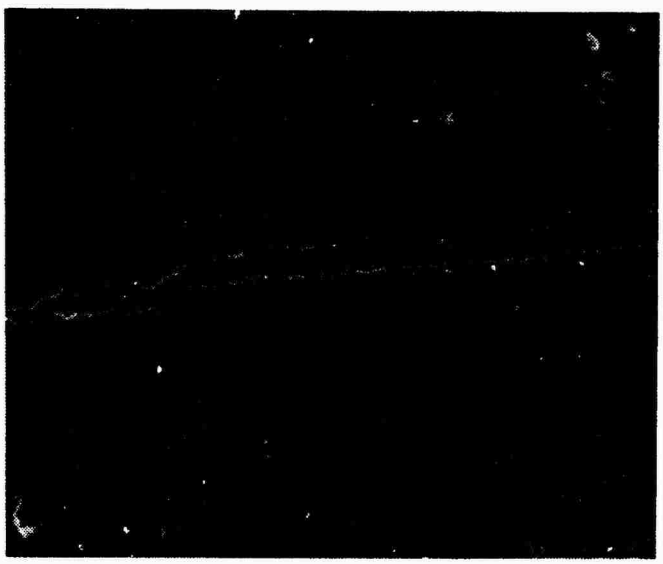

Figure 51. SEM of a crack in a trabeculae. 360X.

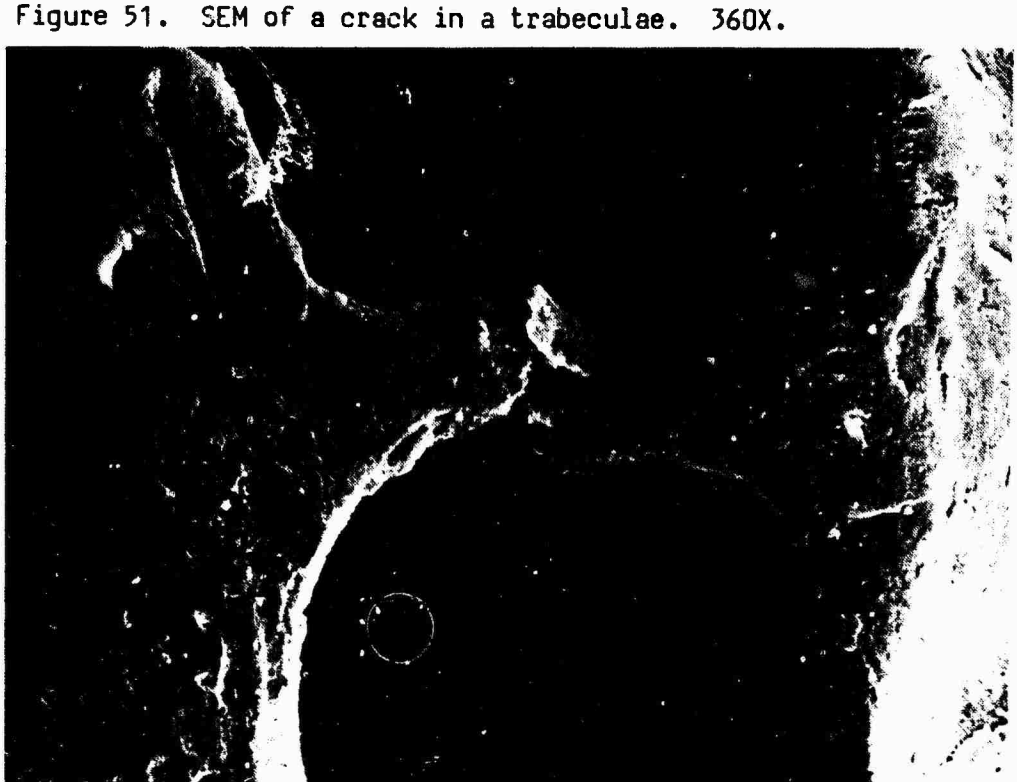

Figure 52. SEM showing a fractured horizontal trabeculae in the end zone. 220X.

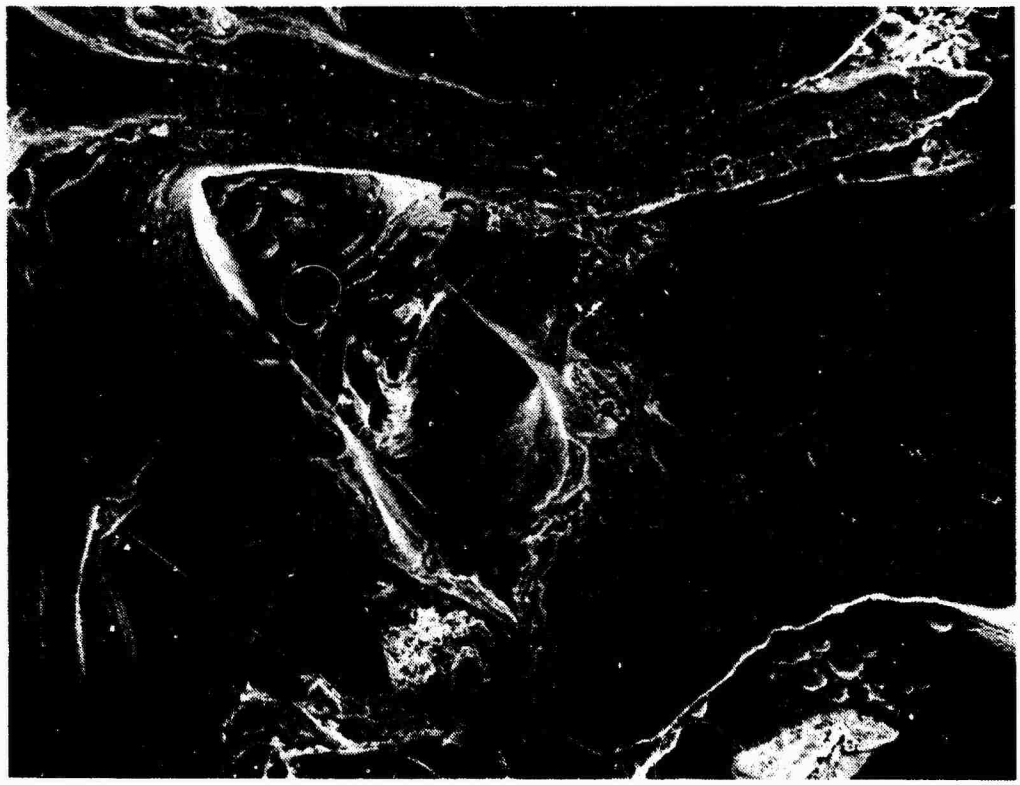

Figure 53. SEM of the central zone of a vertebral body compressed at 8.89×10^{-1} m/sec. 80X.

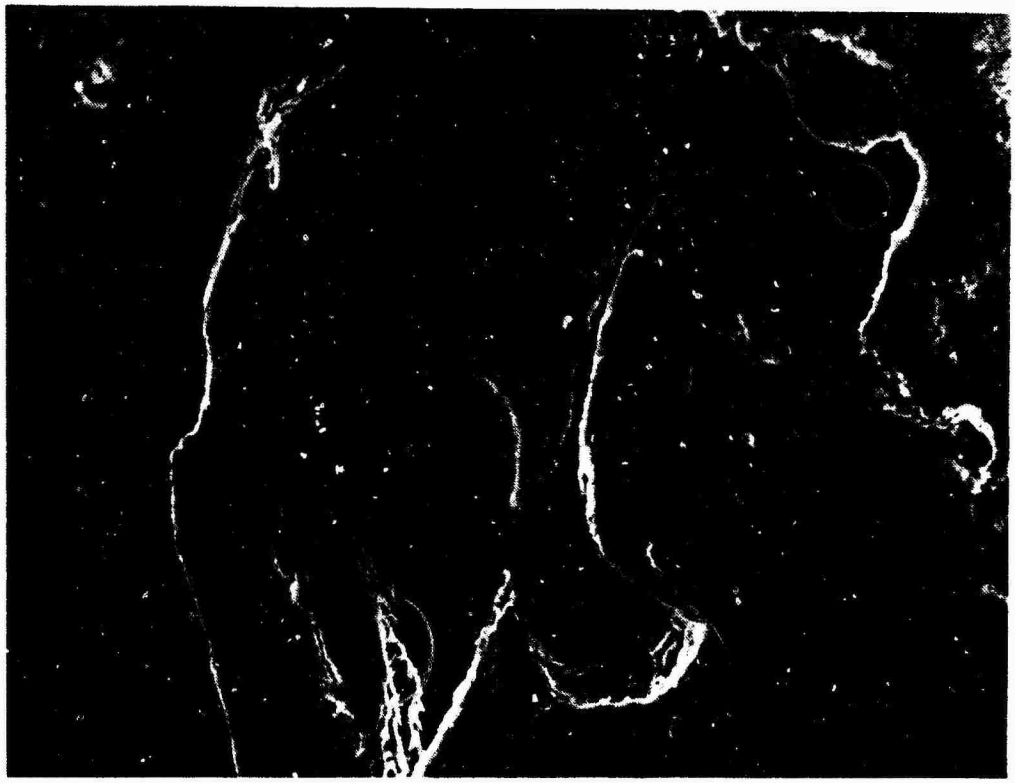

Figure 54. Higher magnification of the central zone of a vertebral body compressed at 8.89×10^{-1} m/sec. 220X.

hemocytopoetic spaces almost obliterated. The bony end plates had numerous fractures which occurred in the regions of the end zones adjacent to the central zone. S-shaped bending and trabecular disorientation were also present to a greater degree than in the above sub-group. Recovered samples in this group returned to 79 per cent of their original height. The trabeculae in the central zone were further apart and the vascular spaces were larger in recovered animals.

Group II. An overall evaluation with SEM of samples sectioned in the anterior-posterior direction revealed more deformation of the bony trabeculae than in samples sectioned in the lateral direction. In samples sectioned in the anterior-posterior direction, the outer collar of cortical bone forming the posterior surface of the vertebral body deformed by concave bending or collapse in the area of the basivertebral vein (fig. 55). The anterior surface of the body collapsed concavely in the cranial end plate area or collapsed concavely in the cranial region and convexly in the caudal region (fig. 56). Figures 57 through 59 are representative scanning electron micrographs of the types of deformation of the outer bony collar of the compressed body.

Scanning electron micrographs of the cranial and caudal trabecular end plates of compressed bodies are shown in figs. 60 and 61. Overall, the caudal end plate was more severely damaged by compression than the cranial plate. Laminar cracking and fracture of the end plate trabeculae are shown in figure 62.

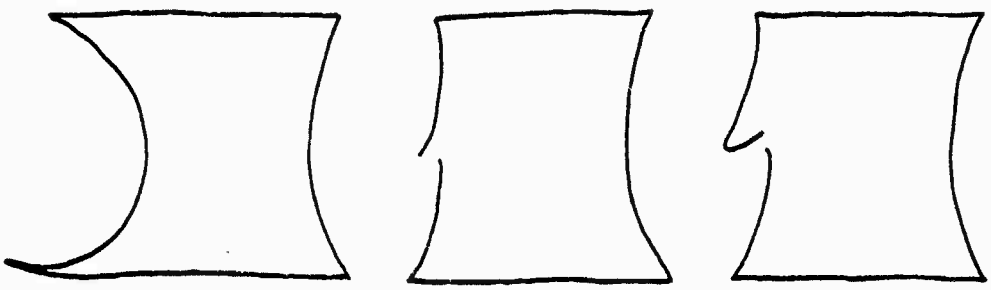

Figure 55. Diagram of types of deformation of the posterior surface of compressed vertebral bodies.

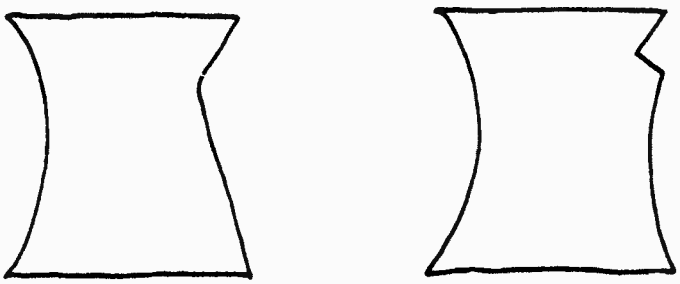

Figure 56. Diagram of types of deformation of the anterior surface of compressed vertebral bodies.

Figure 57. SEM of the superior anterior wall of a compressed vertebral body. F50 L_6, 8.89 x 10^{-5} m/sec. 9.0X.

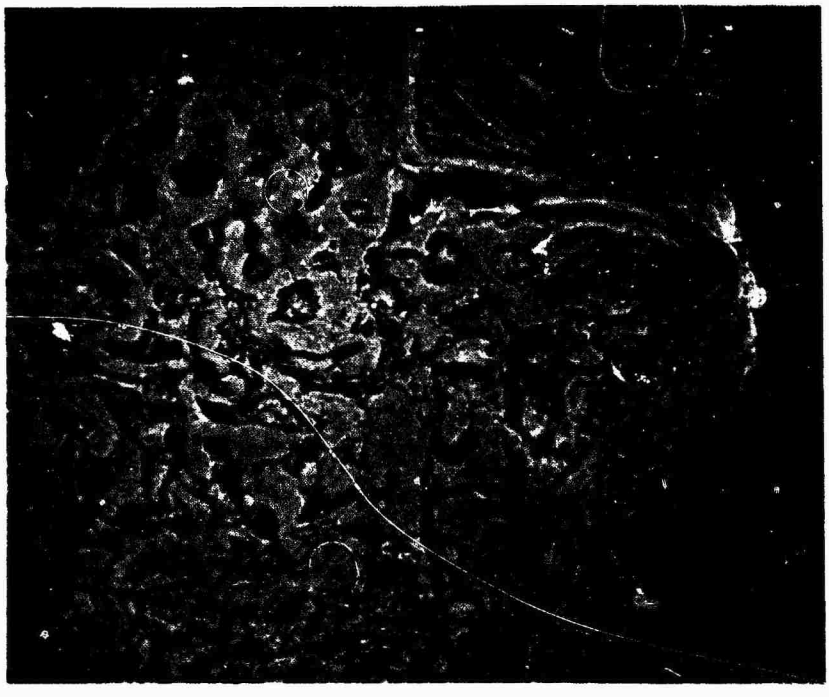

Figure 58. SEM of the posterior wall of a compressed vertebral body. F10 L_2, 8.89 x 10^{-3} m/sec. 8.4X.

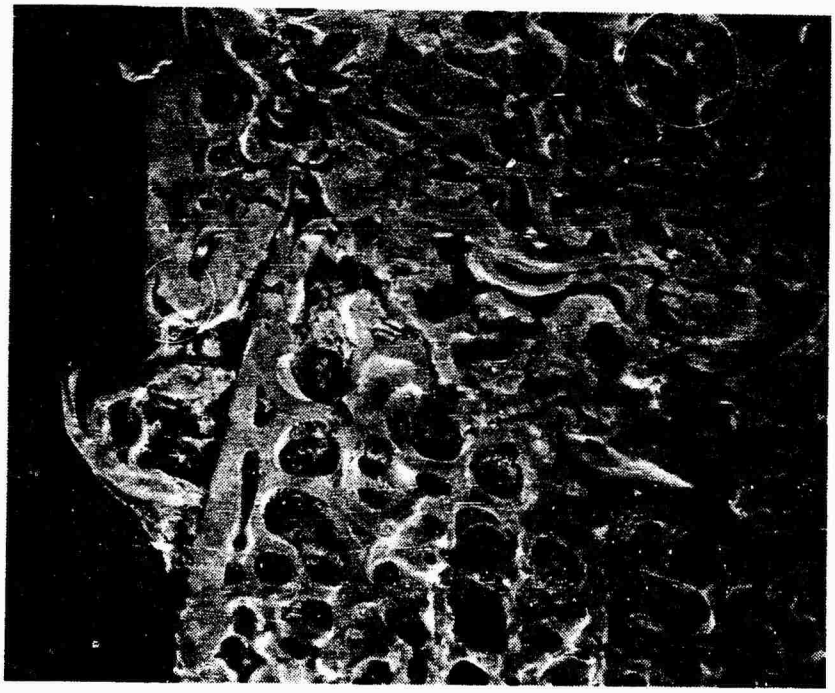

Figure 59. SEM of the posterior wall of a compressed vertebral body. F05 L_2, 8.89 x 10^{-1} m/sec. 8.3X.

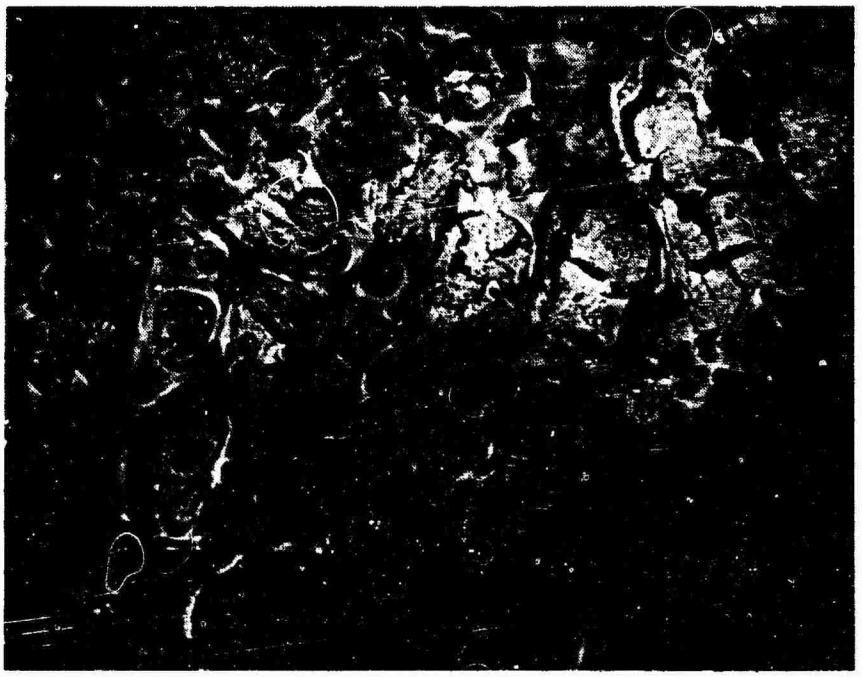

Figure 60. SEM of the superior end plate of a compressed vertebral body. F50 L_6, 8.89 x 10-5 m/sec. 8.7X.

Figure 61. SEM of the inferior end plate of a compressed vertebral body. F50 L_6, 8.89 x 10^{-5} m/sec. 8.9X.

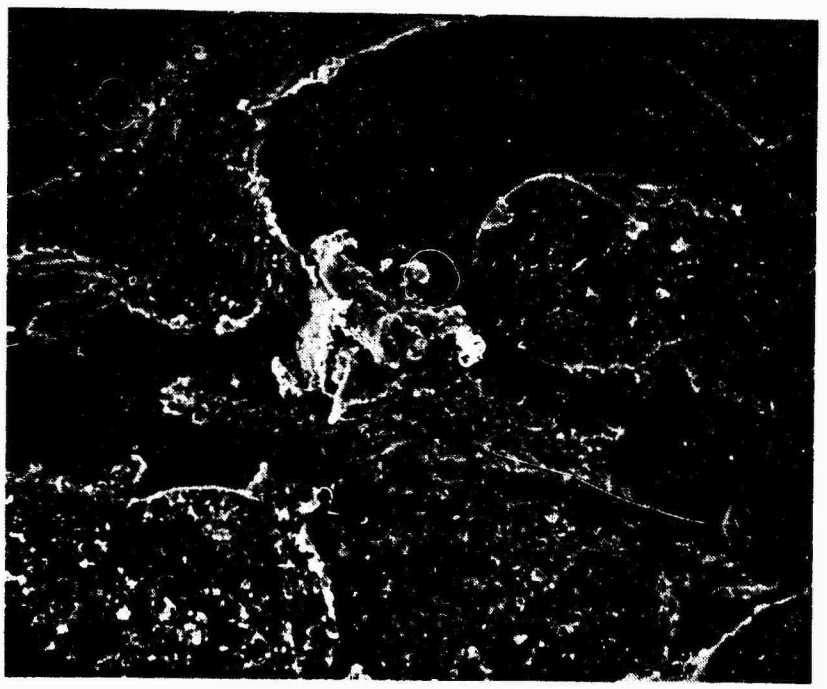

Figure 62. SEM of end plate trabeculae of a compressed body with laminar cracking and fracture. F10 L_2, 8.89 x 10-3 m/sec. 102X.

In the central zone of trabecular bone, bending of the trabeculae occurred at the lower compression rate (8.89×10^{-5} m/sec) (fig. 63). As the compression rate increased, the severity of damage increased to include fractures and more extreme disorientation of trabeculae (fig. 64). Collapse in the region of the basivertebral vein was also observed (fig. 65).

Figures 66 and 67 are representative scanning electron micrographs of compressed bodies sectioned in the lateral direction. Damage to trabeculae in these samples was much less evident.

Figure 63. SEM of trabeculae showing bending typical of lower strain rates. F50 L_6, 8.89 x 10^{-5} m/sec. 58X.

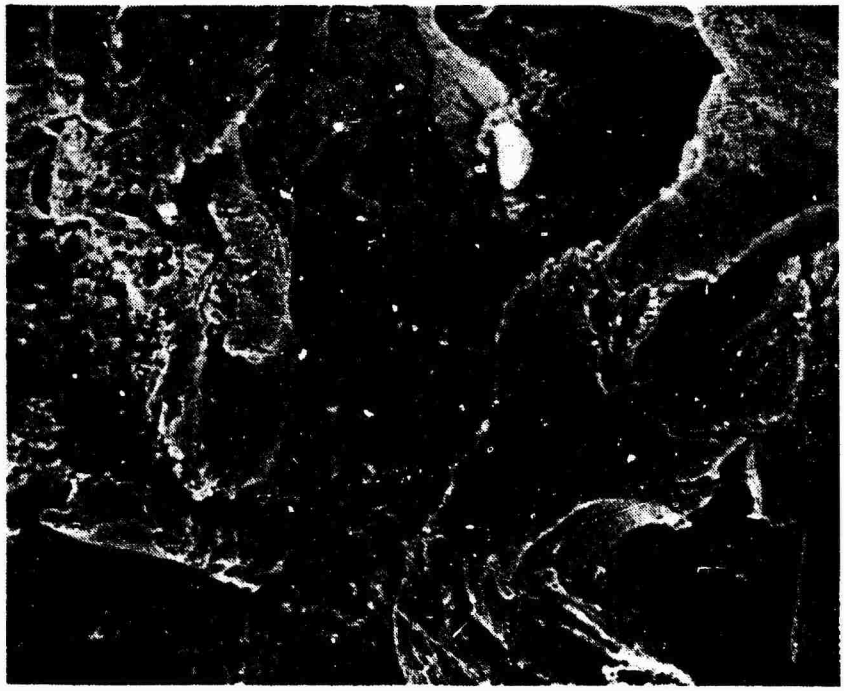

Figure 64. SEM of trabeculae showing fractures and extreme disorientation typical of higher strain rates. F62 L_7, 8.89 x 10^{-1} m/sec. 100X.

Figure 65. SEM showing trabecular collapse in the region of the basivertebral vein. F04 L_2, 8.89 x 10^{-1} m/sec. 10X

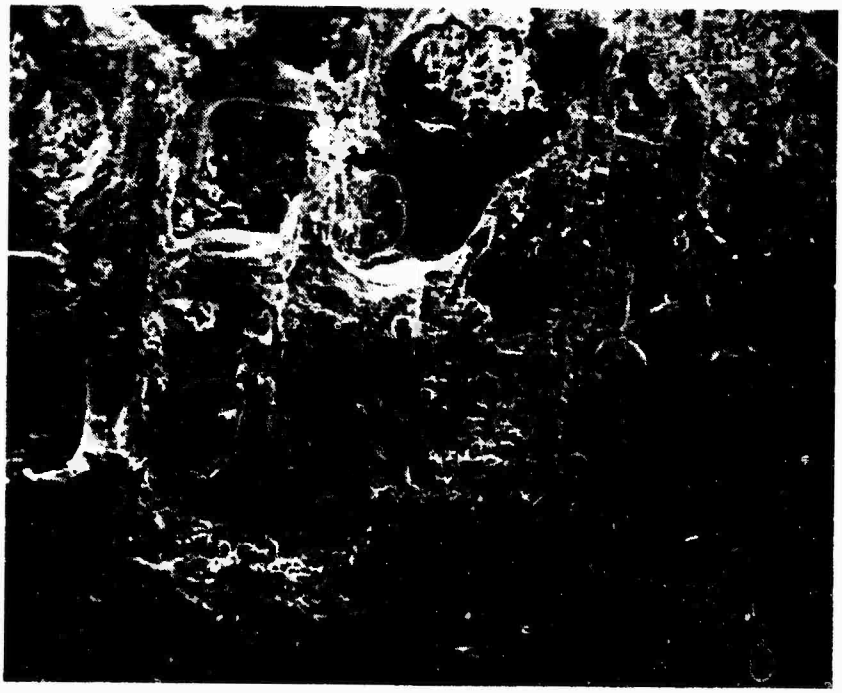

Figure 66. SEM of laterally sectioned compressed vertebral body. F08 T_{12}, 8.89 x 10^{-5} m/sec. 27X.

Figure 67. SEM of laterally sectioned compressed vertebral body. FO8 T_{12}, 8.89 x 10^{-5} m/sec. 18X.

Discussion

Control group. The general appearance of the control vertebral bodies was as previously described by Whitehouse, et al. (1971). Cracks occurring in the matrix surface were attributed to sample preparation. Osteocytic lacunae and canaliculi appeared as described in other work by Anderson and Danylchuk (1977).

Group I. The deformation pattern observed in the compressed vertebral bodies correlated well with observed morphology. Under compressive loading, the vertebral body acts as a pressurized vessel. The internal hemocytopoetic contents of the body are incompressible. Therefore, the body initially deformed, its contents were extruded from the cardiovascular channels, and the trabeculae bent or fractured. When a compressive load is applied, deformation begins in regions ventral to the load source. This reasoning would support the observation that most of the deformation occurred in the caudal central zone of the body which was loaded in a cranial-caudal direction.

The cracks present in the compressed bodies were largely a result of compressive loading. The cracks did not become self-propagating and spread explosively because strain energy within the cancellous bone does not become concentrated at the end of a crack so quickly as in a brittle, purely crystalline material. The strain energy is dissipated in overcoming frictional and viscous resistance to slipping between the components of the crack. When a crack front reaches a fluid-filled region, its energy tends to be absorbed into the fluid. Therefore, trabecular bone may be mechanically visualized to contain a

myriad of energy sinks that provide relative immunity to crack propagation.

Based on their appearance, recovered samples seemed to gain height by the unfolding of bent trabeculae in the central zone. It was also shown that vertebral bodies compressed at higher rates recovered less (fig. 68). This phenomenon is probably due to more severe trabecular damage (i.e., fracture vs. bending) occurring at higher compression rates.

Group II. Most vertebral body samples regained height during the recovery period following compression. Two baboon and two rhesus monkey recovered bodies did not gain or lost height when compared to unrecovered measurements. This gain in height could be due to an unfolding of trabeculae deformed by the compression loading as described above. In this group, a trend toward less recovery of height in bodies compressed at higher rates seemed to be present, but this finding was not consistent. This parameter may have been altered by measuring error or by post-compression freezing, a factor which was not present in Group I. No differences between species in amount of height recovered was noted. This is contrary to previous work by Kazarian (1979).

Samples sectioned in the anterior-posterior direction revealed more deformation than laterally sectioned samples due to the plan of deformation associated with the compression loading. Trabeculae of the bodies bent in an anterior-posterior plane under compression, and this deformation was more obvious when viewed from the side compared to head on (fig. 69).

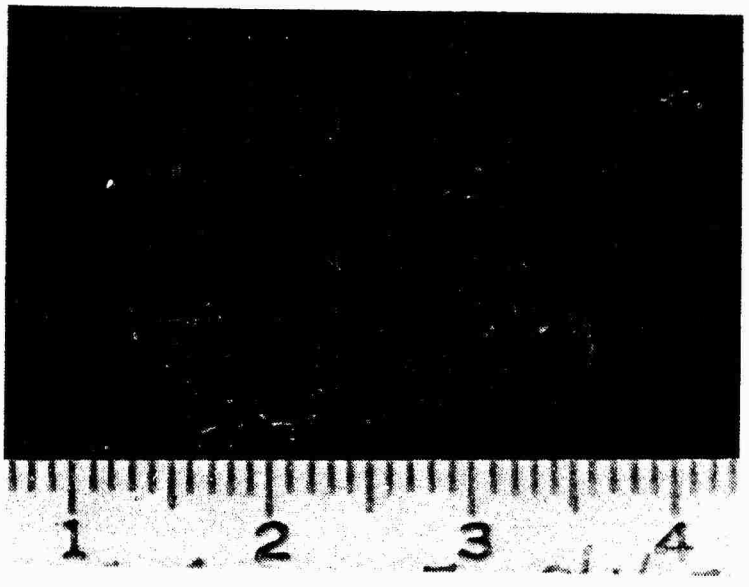

A

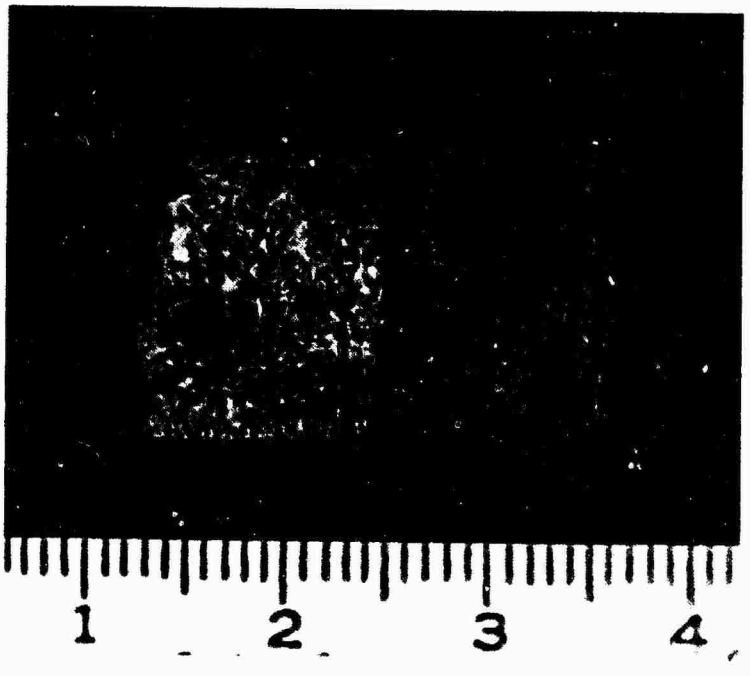

B

Figure 68. Photographs of samples showing difference in height between compressed and recovered samples. A=8.89 x 10^{-3} m/sec; B=8.89 x 10^{-1} m/sec. In A, recovered samples is on the left. In B, recovered sample is on the right. Scale is in centimeters.

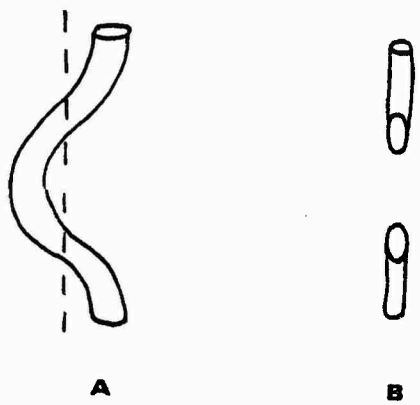

Figure 69. Diagram of deformation of trabeculae as seen from two different angles. A trabecula deformed in the anterior-posterior direction as viewed from the side is shown at A while the same trabecula sectioned along the dotted line and rotated 90 degrees is shown at B.

The deformation patterns of the outer collar of cortical bone probably occurred as a result of the loading forces interacting with the structural geometry of the bony wall. There may also be slight variations in matrical or ground substance components within the body wall which create weaker areas predisposed to failure.

The deformation of trabecular bone composing the core of the body followed patterns observed in Group I above. More severe damage of the caudal end plate was due to the method of loading. At lower compression rates, bending rather than fracture of trabeculae occurred. Bending deformation would account for greater recovery of height of the bodies in the lower compression rate groups as the trabeculae simply unfolded wherein fractured trabeculae lacked this potential.

Laminar cracks evident in higher magnification micrographs of the trabeculae correlate with previous transmission electron microscopy studies by Nussbaum (1977). The author reports "dislocation and fragmentation of the mineral phase" of compressed bone which would explain the cracks observed with scanning electron microscopy.

Compression of the Isolated Spinal Unit

Introduction and Literature Review

A spinal unit consists of two vertebrae plus their intervening disc. The intervertebral disc is composed of a peripheral annulus fibrosus, and a central nucleus pulposus. The annulus fibrosus consists of concentric laminae of collagenous fibers. The fibers interlace obliquely in an alternating fashion as they span the joint space (Eyring, 1969). The annulus inserts on the cartilaginous plates, bone of the body, and the longitudinal ligaments. The anterior annulus is thicker than the posterior (Turek, 1977).

The nucleus pulposus is located within the annulus between the cartilaginous plates. The nucleus is gelatinous and contains a few fine fibers and scattered cells (Turek, 1977).

A vertebra is composed of a body, posterior pedicels, laminae, spine, and zygapophysial joints. The vertebral body, when viewed in sagittal section, has three morphologic regions: cranial and caudal end zones and a central zone. Characteristics of trabecular bone of the zones have been described in a previous section of this report. The cartilaginous end plate and longitudinal ligaments all insert on trabecular bone of the end zones or the outer cortical wall of the vertebrae. A bony annular epiphysis is sometimes present surrounding the periphery of the anterior and lateral sides of the plate.

The cartilaginous end plate is composed of hyaline cartilage. The plate functions as an epiphysis contributing to endochondral growth of the vertebral body (Beadle, 1931; DePalma and Rothman, 1970), and as joint cartilage, creating a barrier between the active pressures of the nucleus pulposus and the vertebral body (Turek,

1977). The plate averages one millimeter in thickness, and it is thinner in the center than peripherally (Eyring, 1969). Fibers have been reported to pass from the nucleus pulposus (Eyring, 1969) and the annulus fibrosus into present between the trabecular bone and the plate (Spurling, 1953). In adolescents, peripheral radial grooves are present on the surface of the body beneath the cartilaginous plate. These grooves are filled with hyaline cartilage of the plate, and they are the site of secondary centers of ossification which later form the annular epiphysis (Beadle, 1931). Small pores have been reported to perforate the plate (Eyring, 1969). Blood vessels penetrate the plate in young animals but close off and disappear near maturity (Beadle, 1931; Eyring, 1969). Ossification gaps are often observed in the plate of young children. These clusters of cells have no bone formation associated with them. These gaps disappear in the adult but may result in weak areas of the plate (Beadle, 1931).

The discs in the thoracic region are thin and of equal height anteriorly to posteriorly. The lumbar discs are thicker than thoracic discs and individually, they are thicker anteriorly than posteriorly (Turek, 1977).

An important feature of trauma to the vertebral column is that changes in normal anatomy can occur without clinical symptoms (Hirsch and Nachemson, 1961; Laurell and Nachemson, 1963). For example, a Schmorl's node may form with disruption of the cartilaginous plate and bony trabeculae but with no symptoms of pain. Brown (1957) has also stated that symptoms can be present without visible changes in vertebral column anatomy. Along the same line, injury may occur with no symptoms initially and severe symptoms later on (Keyes and Compere,

1932). A patient with a Schmorl's node may not have pain with initial formation of the node, but pain may occur later as a result of the collapsed disc space and pressure on nearby nerve roots (Spurling, 1953).

Brown, et al. (1957) studied compression of spinal units and reported fractures and deformation of the cartilaginous end plates. Olin (1937) reported that 80% of the compression fractures of the vertebral column resulted in damage to the annulus fibrosus or cartilage plate with extrusion of the nucleus pulposus.

The purpose of this study was to evaluate the rhesus monkey spinal unit following compression using histology and scanning electron microscopy. Findings of this study were compared to results of compression of the independent vertebral body.

Materials and Methods

Group I. Samples were compressed at 8.89×10^{-3} m/sec or 8.89×10^{-5} m/sec to 50% of their original height in a caudal to cranial direction (opposite from the isolated vertebral body). The samples were air dried and shipped to the investigator in the dried state. The intervertebral discs had been removed by previous processing. Inferior and superior vertebral bodies were identified and sectioned in an anterior-posterior direction. The samples were processed for SEM utilizing techniques as previously described beginning with the OTO method.

Group II. A total of 18 frozen rhesus monkey spinal units were received from Wright Patterson AFB, following mechanical testing. Table 2 indicates the animal, level, and strain rate of testing. The samples were compressed to 50% of their original height in a caudal to cranial direction, frozen, and shipped to the investigator. Upon receipt, the samples were photographed, radiographed, and sawed in half in an anterior-posterior direction. The samples were fixed in 10% neutral buffered formalin for one week and then stored in 70% ethanol. Examination of samples using a dissection microscope was carried out prior to further processing.

Table 2. Spinal units and their rate of compression.

Animal N79-249		Strain rate (m/sec)
Level	T2-3	8.89×10^{-5}
	T4-5	8.89×10^{-1}
	T6-7	8.89×10^{-1}
	T8-9	8.89×10^{-3}
	T10-11	8.89×10^{-5}
	T12-L1	8.89×10^{-5}
	L2-3	8.89×10^{-1}

	L4-5	8.89×10^{-1}
	L6-7	8.89×10^{-1}
Animal	N78-304	
Level	T1-2	8.89×10^{-1}
	T3-4	8.89×10^{-5}
	T5-6	8.89×10^{-1}
	T7-8	8.89×10^{-3}
	T9-10	8.89×10^{-1}
	T11-12	8.89×10^{-1}
	L1-2	8.89×10^{-5}
	L3-4	8.89×10^{-3}
	L5-6	8.89×10^{-3}

One half of each spinal unit was processed for SEM. The SEM sample was dehydrated, critical point dried, and coated with gold-palladium to reduce charging. Samples were scanned at 30 kV in a scanning electron microscope and appropriate photomicrographs were recorded.

The opposite half of the sample was processed for light microscopy. This portion of the sample was decalcified by the sodium-citrate-formic acid method, dehydrated, and embedded in paraffin-plastic embedding material. Eight micrometer routine sections were cut on a rotary microtome and stained with hematoxylin and eosin. These sections were observed with routine transmitted light microscopy and polarized light microscopy. Appropriate sections were photographed.

Results

Group I. The difference in response of the bodies of a spinal unit subjected to compression at different rates is shown in the scanning electron micrographs in figures 70 and 71. At the higher compression rate (8.89×10^{-5} m/sec), damage was more severe. Nuclear material from the intervertebral disc herniated into the superior body forming a Schmorl's node. The disc material entered the body through the hemocytopoetic spaces between trabeculae in the end zone of the body. An anterior wedge compression fracture was observed in the inferior body. In general, compression damage to tissue of the inferior body of the spinal body was more severe than damage to the superior unit. One of the inferior bodies underwent posterior collapse following loading. Within individual bodies, the anterior portion was more severely disrupted than the posterior portion. The damage ranged from laminar cracking and separation to fracture.

Group II - radiography. Fracture, displacement, and/or bending of the anterior cortex such as seen in figure 72 was the most common radiographic finding in the compressed units. Indications of end plate disruption were also apparent in many of the units. The cortical fractures and end plate disruptions were present in all strain rate groups. At the higher strain rate, more severe damage to the unit was apparent and appeared radiographically as fragmentation of the body which was also grossly evident.

Group II - dissection microscopy. Examination of the spinal units with the dissection microscope confirmed the presence of cortical fractures and bending which was previously observed with radiography. Separation of the cartilaginous end plate from the bony

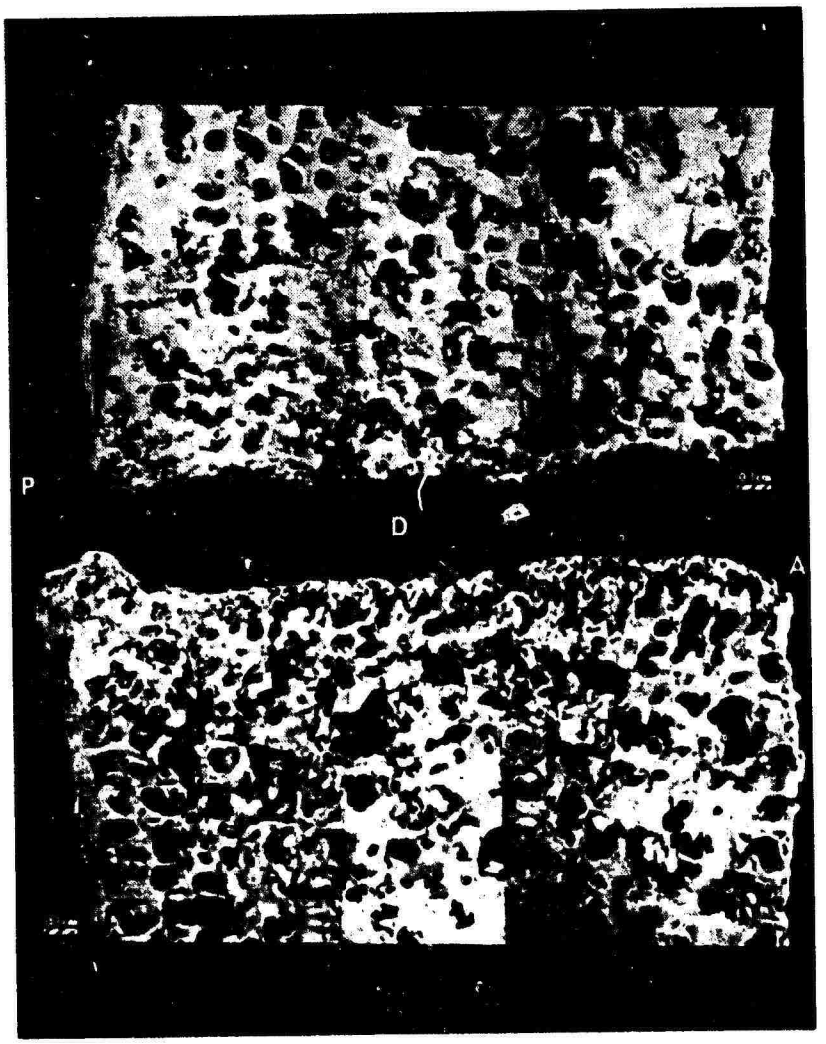

Figure 70. Montage of compressed spinal unit. 18 L_{3-4}, 8.89 x 10^{-5} m/sec. D=disc space; A=anterior; P=posterior.

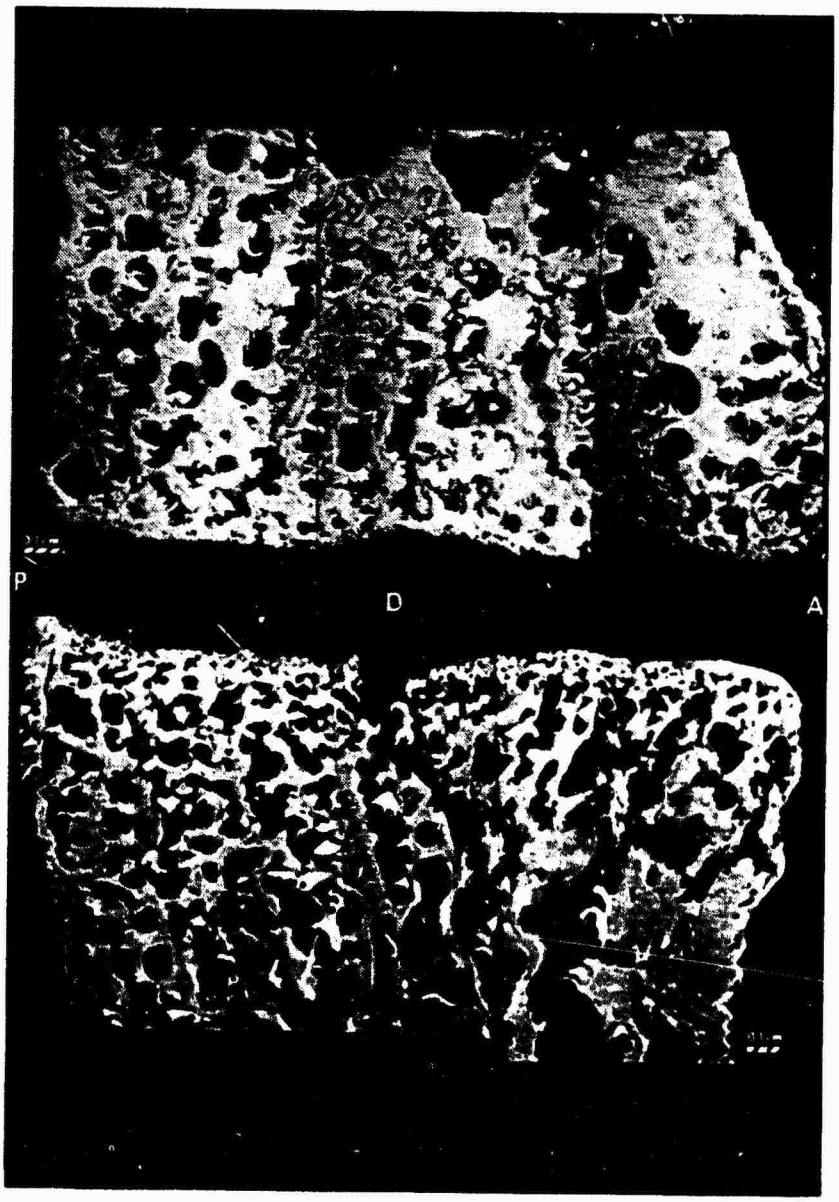

Figure 71. Montage of compressed spinal unit. A370 L_{2-3}, 8.89 x 10^{-3} m/sec. D=disc space; A=anterior; P=posterior; S=Schmorl's node; arrow=anterior wedge compression fracture.

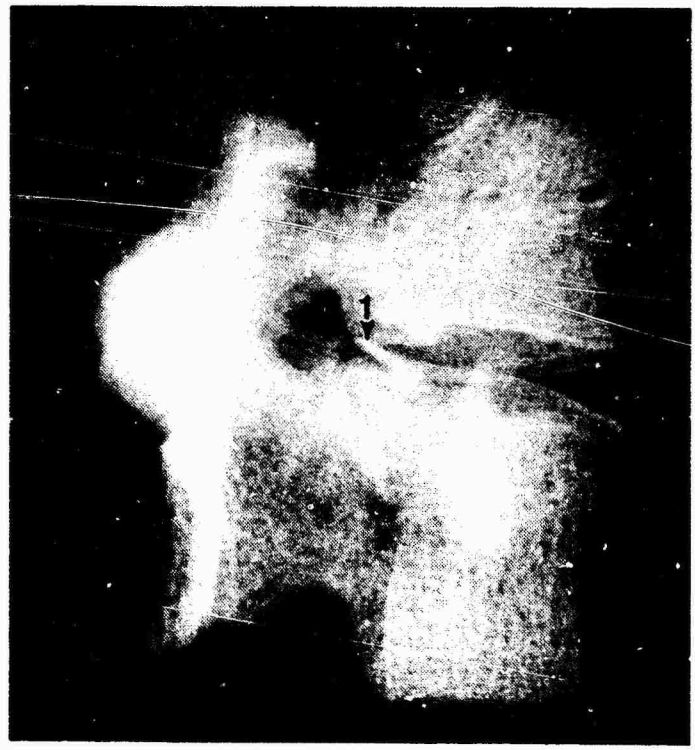

Figure 72. Post compression radiograph of L_{1-2}. 1=end plate disruption, 2=failure of cortical bone.

vertebral body was also apparent. The cartilaginous end plate was fractured, and herniation of disc material was noted.

Group II - scanning electron microscopy. Scanning electron microscopy confirmed that damage was more severe in the superior body of the compressed unit.

The cortical walls bounding the vertebral bodies failed by buckling or fracture. The types of cortical deformation are shown in figure 73. Again, the damage to the cortical wall was generally more severe in the superior body of the unit.

Figure 74 shows trabeculae of the posterior-inferior region within the superior body. Extensive trabecular fractures and collapse of hemocytopoetic spaces was observed in the superior body. In comparison, in the same region of the inferior body (fig. 75), moderate laminar cracking and scattered trabecular fractures were present. Some evidence of trabecular bending was present, but it was not as prominent as previously reported in the compression of single vertebral bodies (Eurell, 1977).

A separation between the bone of the vertebral body and the cartilaginous end plate was present in most compressed units (fig. 76). The separation traversed the entire unit from anterior to posterior. Integrity between the disc and vertebral bodies was maintained by the anterior and posterior longitudinal ligaments in most cases. However, ruptures of one or more of the ligaments was frequently present near their sites of attachment on the vertebral body or disc. A tight junction was always present between the annulus fibrosus and the cartilaginous end plate (fig. 77).

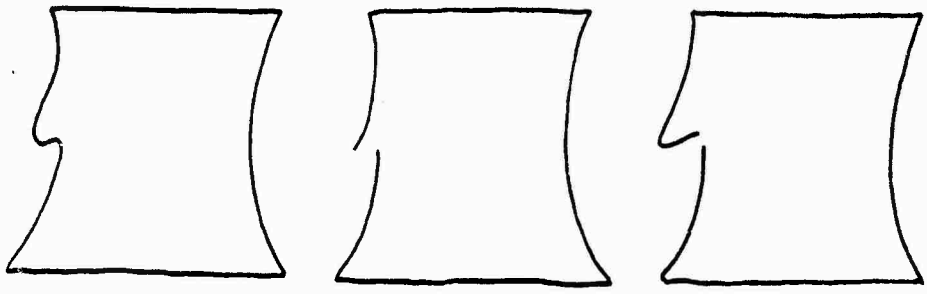

Figure 73. A schematic representation of cortical wall failure.

Figure 74. SEM of trabeculae in the posterior-inferior region of the superior body of a compressed spinal unit. Strain rate = 8.89 x 10^{-5} m/sec.

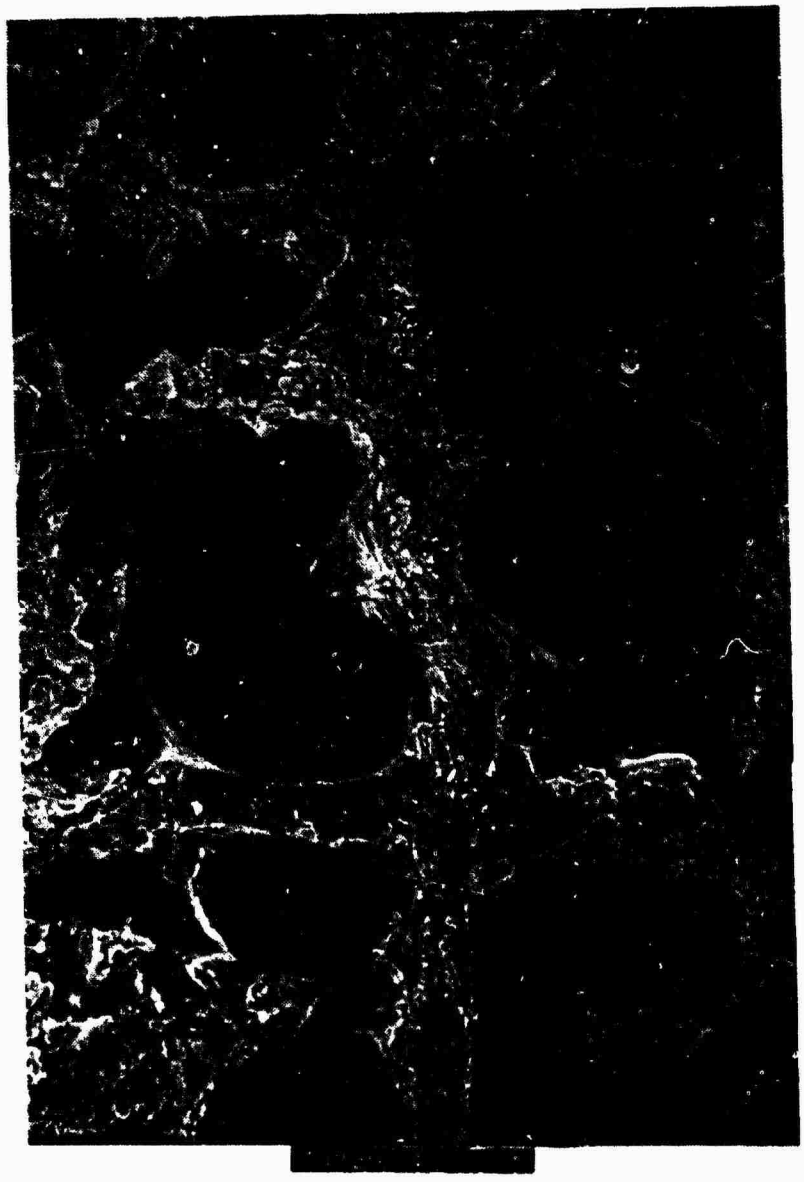

Figure 75. SEM of trabeculae in the same region as figure 74 of the inferior body of a compressed spinal unit. Strain rate = 8.89 x 10^{-5} m/sec.

Figure 76. The region of the intervertebral disc of L_{1-2} following compression. Strain rate = 8.89×10^{-5} m/sec. C=cartilaginous end plate; N=nucleus pulposus; A=annulus fibrosus; arrows indicate fractures and separation of the end plate from the vertebral bodies.

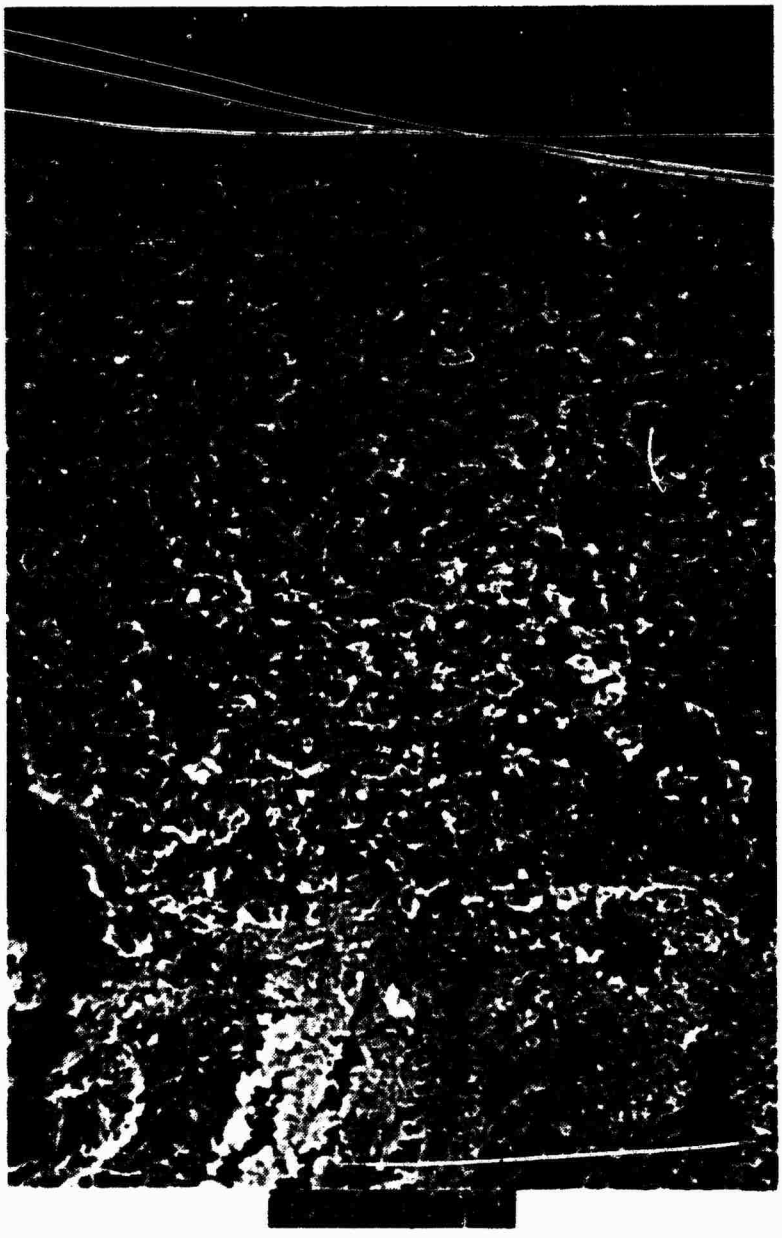

Figure 77. A higher magnification of the end plate region of L_{1-2} following compression. The separation from the vertebral body is apparent at the top of the photograph. Note the tight junction between the end plate and the rest of the disc.

In addition to the separation of the cartilaginous end plate from the vertebral body, the end plate was also usually fractured in a direction parallel to the axis of the unit. At the low strain rate, this fracturing ranged from a breaking off of fragments of the cartilaginous plate, leaving a continuous barrier between the vertebral body and the remaining disc (figs. 78 and 79), to multiple breaks in the plate which completely traversed it, creating pathways from the disc to the vertebral body (fig. 76). When the cartilaginous end plate was fragmented, the pieces were usually found embedded in the disc. Disc material was often noted penetrating breaks in the end plate. (The nature of this disc material was later confirmed using light microscopy. See below.) Although the fractures usually occurred in the cranial end plate of the disc (fig. 80), they were not limited to that region (fig. 76). The major fractures were usually associated with the central nucleus pulposus but smaller cracks were also noted in peripheral regions of the plate (approximately 1/3 of the way in from the anterior edge of the unit).

At the higher strain rate, damage to the disc region ranged from fractures of the end plate and displacement of vertebral trabecular bone into the nucleus pulposus and annulus fibrosus (figs. 81 and 82) to complete fragmentation of the disc with subsequent displacement of the fragments into the vertebral bodies (fig. 83) or outside the limits of the normal disc.

Group II - light microscopy. Due to prior mechanical testing, the cellular components of the spinal units had deteriorated, however, many of the features observed with SEM could still be confirmed.

Figure 78. SEM of T_{3-4} following compression at the low strain rate. The arrow indicates a fragment of cartilaginous end plate embedded in the disc.

Figure 79. Higher magnification of the cartilaginous fragment shown in figure 78.

Figure 80. Posterior disc region T_{10-11} following compression. Note the separation of the end plate and fracture of the superior plate.

Figure 81. Posterior disc region of T_{5-6} compressed at the high strain rate. Note the fragment of trabecular bone embedded in the disc.

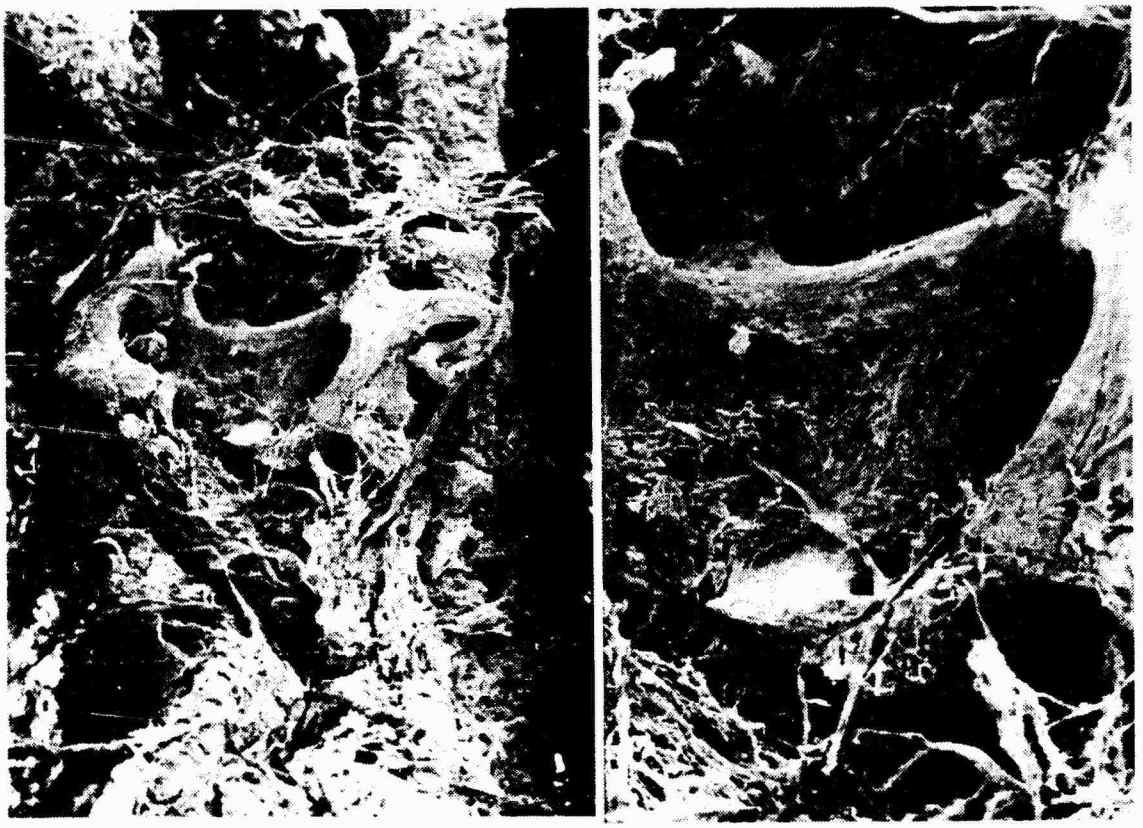

Figure 82. Higher magnifications of figure 81 showing detail of the body fragments.

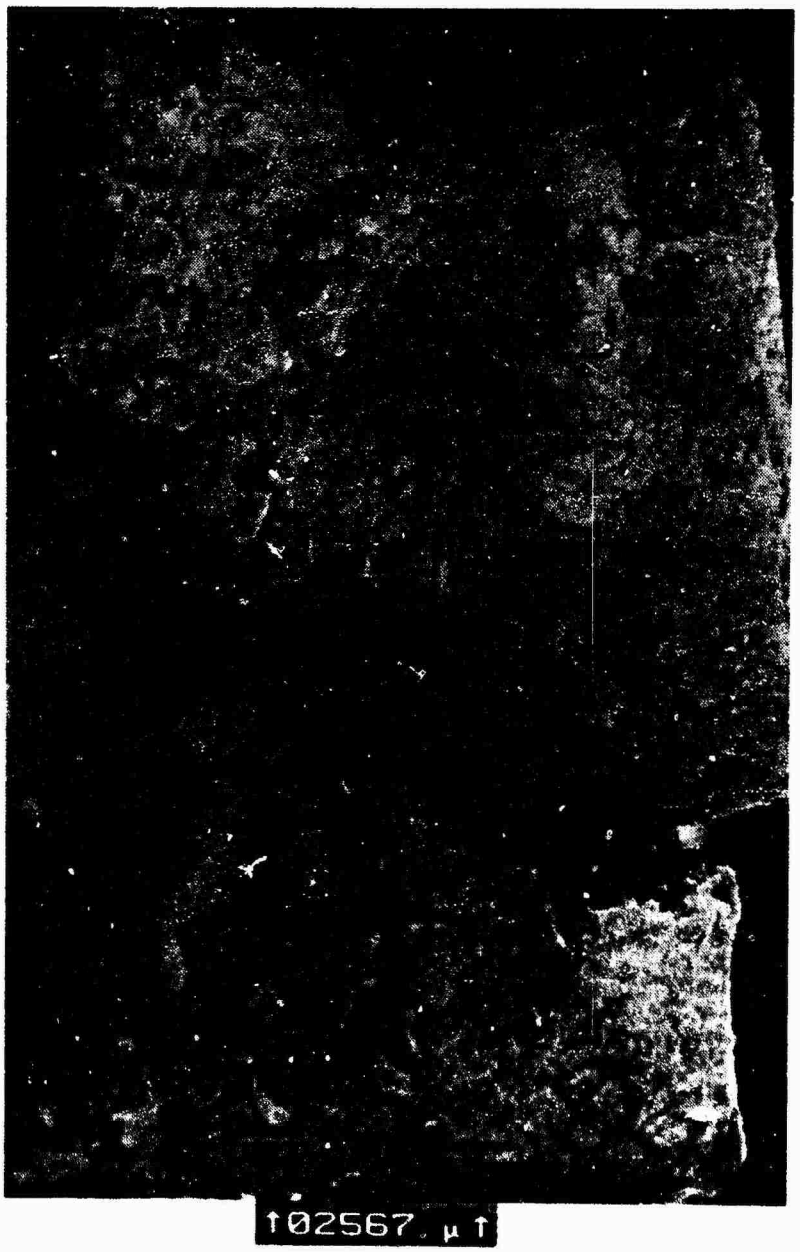

Figure 83. Disc region of T_{6-7} compressed at the high strain rate. Note that the posterior portion of the disc is compressed into the inferior vertebral body and the anterior portion of the disc is missing.

Separation between the cartilaginous end plate and the bone of the vertebral body was present. The separation occurred in the zone of junction between hyaline cartilage and trabecular bone.

Fractures of the end plates of units compressed at the lower strain rate were observed to contain nuclear material. When fractures of the plate were complete, disc material passed from the disc into the vertebral body above or below the fracture site.

Entire fragments of the disc including both end plate and the annulus were found embedded in the vertebral bodies of units compressed at the higher strain rate. These large disc fragments fractured and displaced trabeculae in their path as they penetrated the vertebral body.

Upon further examination of the spinal units at higher magnification, laminar cracks in the trabeculae of the vertebral bodies were observed. Bending of individual trabeculae was present as were some trabecular fractures.

Group II - polarizing light microscopy. Features observed with routine light microscopy at higher magnification were greatly enhanced with polarizing microscopy. Figure 84 is a typical example of a trabeculae from a compressed spinal unit. Numerous trabecular fractures were present. In areas of trabecular bending, laminar separations were noted. Also present were microfractures running at 45 degree angles to each other which were not previously observed with routine light microscopy.

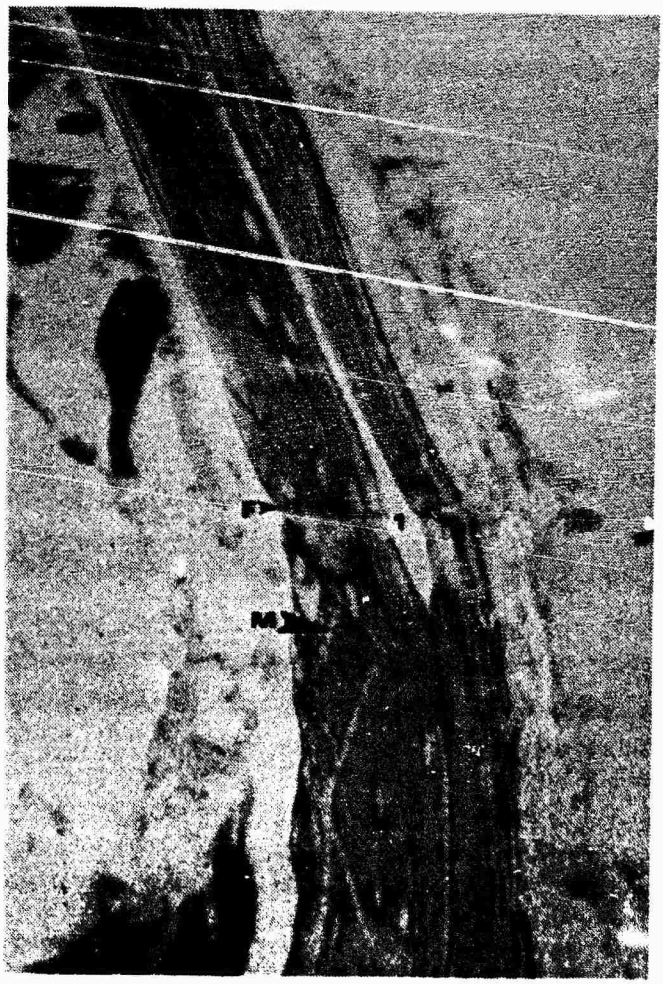

Figure 84. Polarizing light micrograph of a trabecula from a spinal unit (T_{12}-L_1) compressed at the lower strain rate. Note the laminar separations (1), fracture (F), and microfractures (M).

Discussion

Group I. Spinal unit samples were loaded with minimum angulation and they acted comparable to units loaded in that mode in vivo, i.e., burst injuries were observed. The injuries were most apparent at the higher compression rate (8.89×10^{-3} m/sec vs. 8.89×10^{-5} m/sec) further indicating more severe damage to spinal column structures at higher strain rates.

Formation of the Schmorl's node followed previously proposed patterns in which the relatively compression resistant nucleus pulposus herniated into the less resistant vertebral body (Roaf, 1960). Hemocytopoetic spaces between trabeculae provided the pathway for the projectile nuclear material.

Collapse of the anterior portion of the body with minimum angulation loading can be attributed to structural geometry of the vertebra. Additional protective support to the posterior body is provided by the posterior aspects of the column. However, there may be compositional differences which have not been previously investigated in the anterior body which might predispose it to collapse.

Increased damage in the inferior body of the unit was probably a function of the loading process.

Group II - radiography. Indications of cortical and end plate damage to the compressed vertebral units were present on radiographs following testing. The cortical bone often appeared fragmented and indentations in the trabecular bone underlying the end plate were observed. However, additional damage to the unit that did not appear on routine radiographs was seen later with other methods.

Fractures of trabeculae and herniation of disc material were not apparent using radiography only.

Group II - dissection microscopy. With the dissection microscope, the damage to the internal structure of the sectioned spinal unit could be better characterized. The "end plate disruptions" seen with radiography were found to be actual separations between the cartilaginous plate and the underlying bone of the vertebral body. Fractures in the end plate which created pathways for the escape of disc material into the associated vertebral bodies were also apparent.

Group II - scanning electron microscopy. During the compression sequence, the spinal unit was loaded in a caudal to cranial direction. The superior body absorbed most of the forces associated with the compression. These forces were dissipated by the superior body itself and the intervening disc prior to reaching the inferior body, thus explaining the more severe damage to the structures of the superior unit.

The patterns of failure of the cortical and trabecular bone of the vertebral body were similar to those observed previously in studies of the compression of individual vertebral bodies (see above). The decrease in overall severity of the damage to the bony structures of the compressed unit when compared to the single compressed body is probably due to the shock absorber action of the intervening disc.

The separation of the cartilaginous plate from the vertebral body in the compressed units occurs in an area similar to the zone of maturing cartilage in the growth plate of long bones. Epiphyseal separations due to shearing generally occur in the maturing zone of

long bones (Ham, 1979). This zone probably breaks down because of the difference in material properties of the calcified and uncalcified tissues which it links. Perforating fibers (Sharpey's fibers) which anchor the annulus fibrosus and nucleus pulposus to the cartilaginous plate help to maintain the continuity of the region which is not disrupted during compression.

Fractures of the cartilaginous plate resulted from forces generated by the compressive loading. The amount of damage to the plate was related to the strain rate, i.e., the higher the rate, the greater the damage. Because of the method of loading, the superior end plate of the disc absorbed more of the loading forces before they reached the inferior plate, and therefore the superior plate was usually more frequently fractured. The nucleus pulposus is relatively resistant to compression (Roaf, 1969). Fractures of the end plate were generally related to the nucleus because during compression, the plate deformed around the nucleus and eventually fractured.

The higher strain rates have been previously shown to cause more severe damage to the bone of compressed vertebral bodies (see above). Although the presence of the disc helps to dissipate some of these forces, the bodies may still be severely damaged and in turn cause damage to the disc as illustrated by the breaking off of bony fragments and their subsequent lodging in the disc. Even the lower strain rates, which result in cracks of the cartilaginous plates and escape of disc material, should be considered detrimental to the integrity of the unit.

Group II - light microscopy. The deterioration of the tissues was due to the length of time between harvest and fixation necessary

for mechanical testing. This factor must be considered in the final analysis of this study. Although effects on general morphology are somewhat minimal, other aspects, such as quantitative histochemistry, would be altered and were not pursued.

Fractures observed in the cartilaginous end plates created a pathway for escape of incompressible nuclear material through the plate and into the hemocytopoetic spaces of the vertebral body creating a Schmorl's node. Laminar cracking was found to be more extensive within trabeculae than was first apparent with SEM. The cracks were a result of compression and tension within trabeculae as they responded to loading.

Group II - polarizing light microscopy. With the use of polarizing light microscopy, the extent of damage to vertebral bone became much more apparent. The pattern observed in the compressed bodies was usually typical of bending failures as described by Frankel and Nordin (1980). The oblique microfractures occurred on the side of the trabecula subjected to compression during bending while the laminar separations occurred on the tension side. Often, bending resulted in fracture of the involved trabecula.

The Vertebral Column of *in vivo*-Impacted Baboons[1]

Introduction and Literature Review

Subcritical +Gz impact which produces no direct injury has been suggested as a likely cause for subsequent radiographic lesions of spondylosis deformans traumatica observed in vertically impacted baboons (Van Sickle and Kazarian, 1982; Van Sickle, 1984). Spondylosis deformans traumatica is characterized by bony osteophytes which develop at the junction of the cortex of vertebral bodies and the annulus fibrosus of degenerating discs. Baboons impacted at 40 Gs with a time of duration of 10-13 msec had radiographic spinal changes ranging from no apparent damage to minor subluxation immediately following impaction. Within 12 months, increased density of the anterior annulus fibrosus was apparent and by three years post-impaction, osteophytes had appeared. The bone of the vertebral bodies was also increased in density. Histopathology of the baboon tissue six years post-impaction confirmed the presence of osteophytes, collapsed intervertebral disc spaces, a Schmorl's node, and zygapophysial joint osteoarthrosis.

The objective of this study was to examine the vertebral columns of impacted baboons at intervals immediately, one month, three months, six months, and six years post-impaction with scanning electron microscopy to determine the effects of impaction on the column. Light microscopy of the vertebral colu was also included for comparison with scanning electron microscopy.

---

[1] A portion of the tissues for this study were contributed by Dr. D.C. Van Sickle, Purdue University.

Materials and Methods

Twelve male baboons (Papio anubis) weight 20 kg each were subjected to subcritical +Gz impact of 40 Gs for 10-13 msec using a seat-restraint impact vehicle. Five unimpacted control animals were also included in the study. Each test animal was radiographed at regular intervals following impaction until euthanasia. The test animals were euthanitized immediately, one month, three months, six months, or six years post-impaction (Table 3).

Table 3. Experimental groups of impacted baboons.

Interval post-impaction	Animal number	Animal weight at necropsy (lbs)
Control	G30	58.5
	G82	29.0
	H12	37.0
	H18	48.0
Immediate	H20	52.0
	H22	52.0
	H24	53.0
One month	H08	49.0
	H14	41.0
	H16	47.0
Three months	H10	27.0
Six months	G74	25.0
	G84	26.5
	G88	27.0
Six years	E18	?
	E34	95.0

At necropsy, tissues were collected for SEM and LM. The vertebral columns of all experimental animals were radiographed prior to sectioning. Anterior-posterior, lateral, and oblique projections were recorded. The vertebral columns were sectioned mid-sagitally and fixed in 10% neutral buffered formalin. SEM tissues were etched to

remove hematopoetic tissue, dehydrated, critical point dried, and coated with gold palladium. Tissues for LM were decalcified with sodium citrate-formic acid, embedded in paraffin-plastic, sectioned, and stained.

Results

Radiology. Control group. Radiographs of the control animals were within normal limits with the exception of animal H18. This animal had osteophytes on the anterior margin of T_{12}, L_2, and L_3. The intervertebral disc space of T_{12-13} was bridged by a large osteophyte anteriorly, and the space of L_{4-5} was obliterated by bony fusion of the vertebral bodies (fig. 85). The homogeneous calcified zone of the end plate was clearly visible in G82 (fig. 86). This zone of the end plate was separated from the rest of the vertebral body by a less dense zone.

Immediately post-impaction group. Radiographs of the immediately post-impaction animals were within normal limits with the exception of H24 which had numerous osteophytes along the anterior border of the vertebral column.

One month post-impaction group. Radiographs of the one month post-impaction animals were within normal limits with the exception of animal H14. This animal had irregular anterior margins of the lumbar vertebrae with lipping of the superior and inferior junctions at the disc. The central nuclear region of the disc seemed to extend into the cartilaginous end plate creating a less dense area (fig. 87).

Three months post-impaction group. Radiographs of the three months post-impaction animals were within normal limits.

Six months post-impaction group. Radiographs of the six months post-impaction animals were within normal limits except for G88. The end plates of G88 were irregularly mineralized (fig. 88) when compared to the control animal of similar weight.

Figure 85. Lateral radiograph of control baboon. Bony fusion of L_{4-5}. H18.

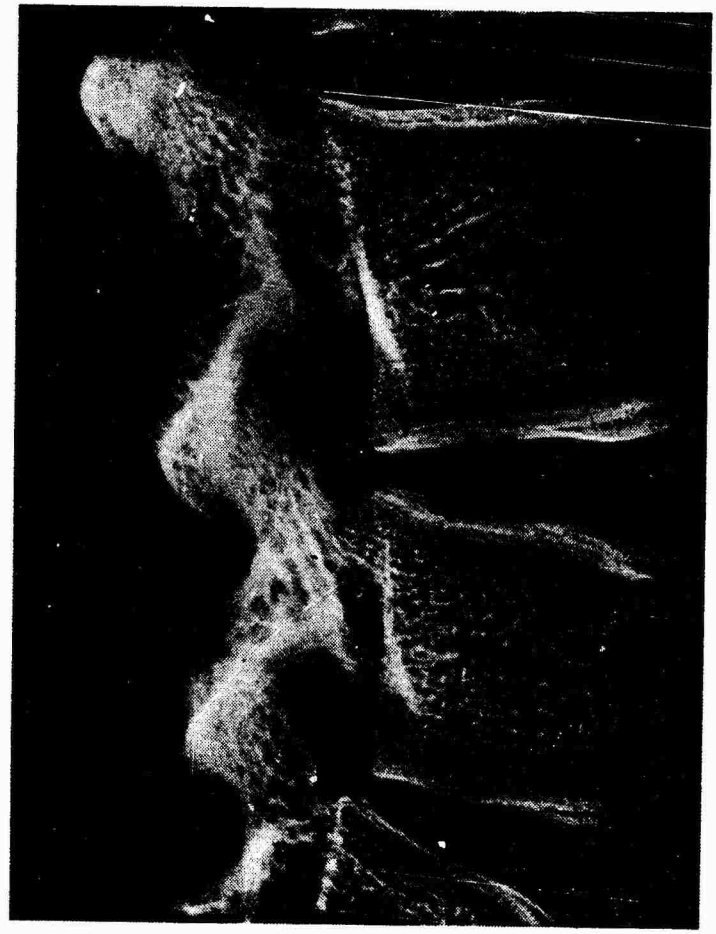

Figure 86. Lateral radiograph of control baboon (G82, upper lumbar level). Calcified zone of the cartilaginous end plate is indicated by the arrow.

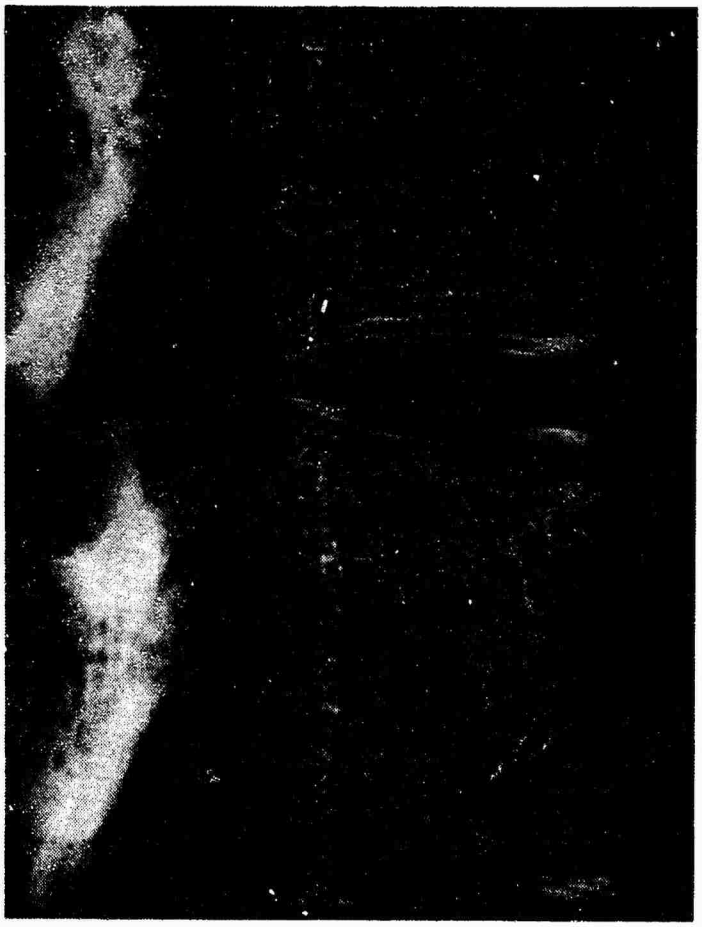

Figure 87. Lateral radiograph of one month post-impaction baboon (H14, L_{4-5}).

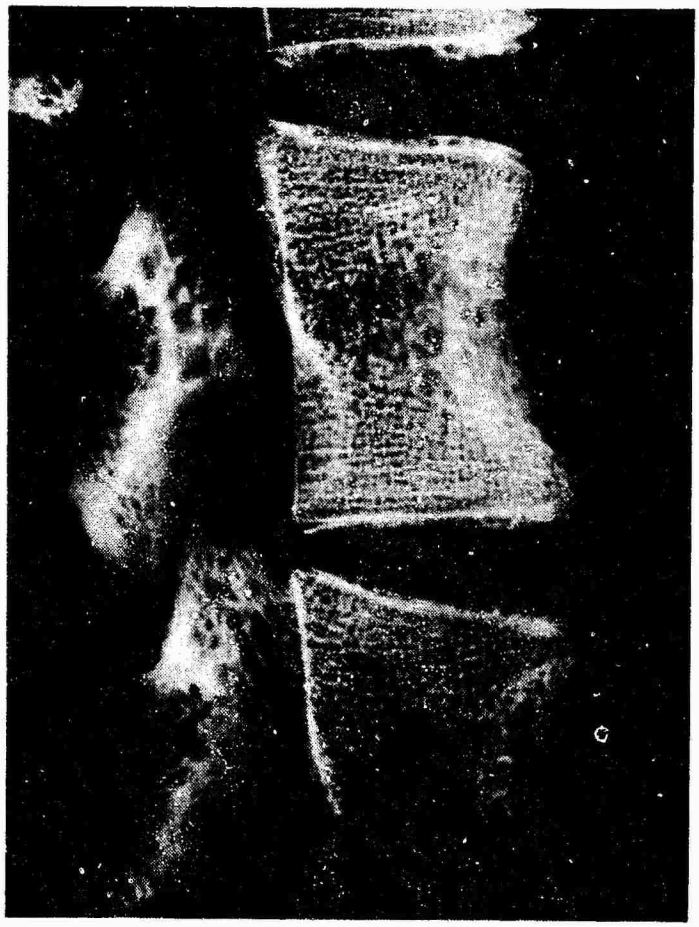

Figure 88. Lateral radiograph of six month post-impaction baboon (G88, L_{3-4}).

Six years post-impaction group. Radiographic changes in the impacted baboons were most evident in the six year post-impaction animals. Both animals had numerous osteophytes along the anterior border of the column (fig. 89). The vertebral bodies were often wedge-shaped in appearance indicating anterior collapse. Oblique views of the spinal column as shown in figure 90 indicated varying degrees of fusion of the facet joints.

Scanning Electron Microscopy. Control group. The vertebral bodies, cartilaginous end plates, and intervertebral disc were clearly visible with SEM (fig. 91). Fragments of bone were present on the cut surface of the SEM samples. These fragments were homogeneously scattered across the surface and were thought to be due to the sawing process during preparation. The control animals had intact cartilaginous end plates which separated the vertebral bodies from the intervertebral discs (fig. 92). The end plate appeared to be tightly adhered to both the disc and the vertebral body. An annular epiphysis was embedded in the anterior end plate of older animals. Uncalcified regions which crossed the end plate vertically near the nucleus pulposus were also noted (fig. 91).

Two zones of the cartilaginous end plate were observed. The outer articular zone next to the intervertebral disc was composed of a superficial and a deep region. The superficial region consisted of a homogeneous matrix with scattered chondrocytes. This region was about 150 μm thick and was located next to the disc. The deep region of the articular zone had scattered mineralized islands with areas of uncalcified cartilage between. This region varied from 700 to 1000 μm in thickness. The second zone visible with SEM was the inner growth

Figure 89. Lateral radiograph of L_{1-4} of a six year post-impaction animal. Note anterior osteophytes at all levels and vertebral body wedging of L_2. E18.

Figure 90. Right oblique radiograph of T_{13}-L_5 of a six year post-impaction animal. Note the partial fusion of L_{1-2} facet joint. E18.

Figure 91. SEM of caudal disc region of control animal. Fragments scattered across the sample surface are preparation artifacts. G30 L3-4.

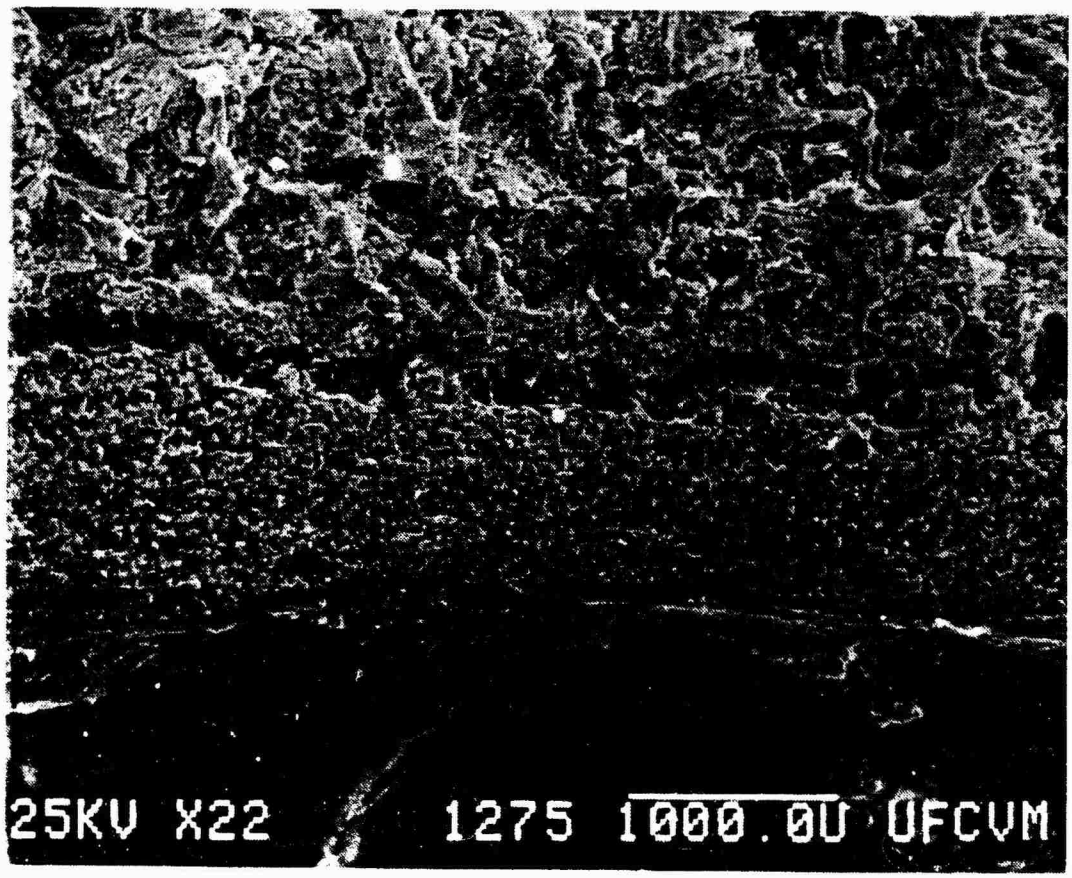

Figure 92. SEM of the cartilaginous end plate of a control baboon. G82, upper lumbar region.

zone which was located next to the trabecular bone of the vertebral body. In this region, the chondrocytes were arranged in columns with artifactual spaces between the columns. This growth region was only present in younger animals (G82 of the control group).

The vertebral body had anterior and posterior cortices of compact bone. The center of the body was composed of trabecular bone.

The articular surfaces of the zygapophysial joints ranged from smooth (figs. 93 and 94) to severely eroded (figs. 95 and 96). The eroded cartilage had large cracks and fibrillation.

A fused disc space was observed at L_{4-5} in H18 (fig. 97). The trabecular bone of the adjacent vertebral bodies extended across the disc space in several locations. The cartilaginous end plates and the balance of the intervertebral disc were replaced by homogeneous connective tissue.

A Schmorl's node was observed at L_{2-3} in animal G30 (fig. 98). A clear pathway from the nucleus pulposus through the cartilaginous end plate into the vertebral body was present.

Immediately post-impaction group. Fractures were observed in the cartilaginous end plates of immediately post-impaction animals (fig. 99). Cracks were noted in both the articular and growth zones. Zygapophysial joint articular surfaces had slight peripheral fibrillation.

One month post-impaction group. Fractures of the cartilaginous end plate as observed in the immediately post-impaction animals were also present in this group (fig. 100). An area of fractured trabeculae was also noted above the end plate of three samples.

Figure 93. SEM of the articular surface of a zygapophysial joint from a control baboon. H12, T_{13}-L_1.

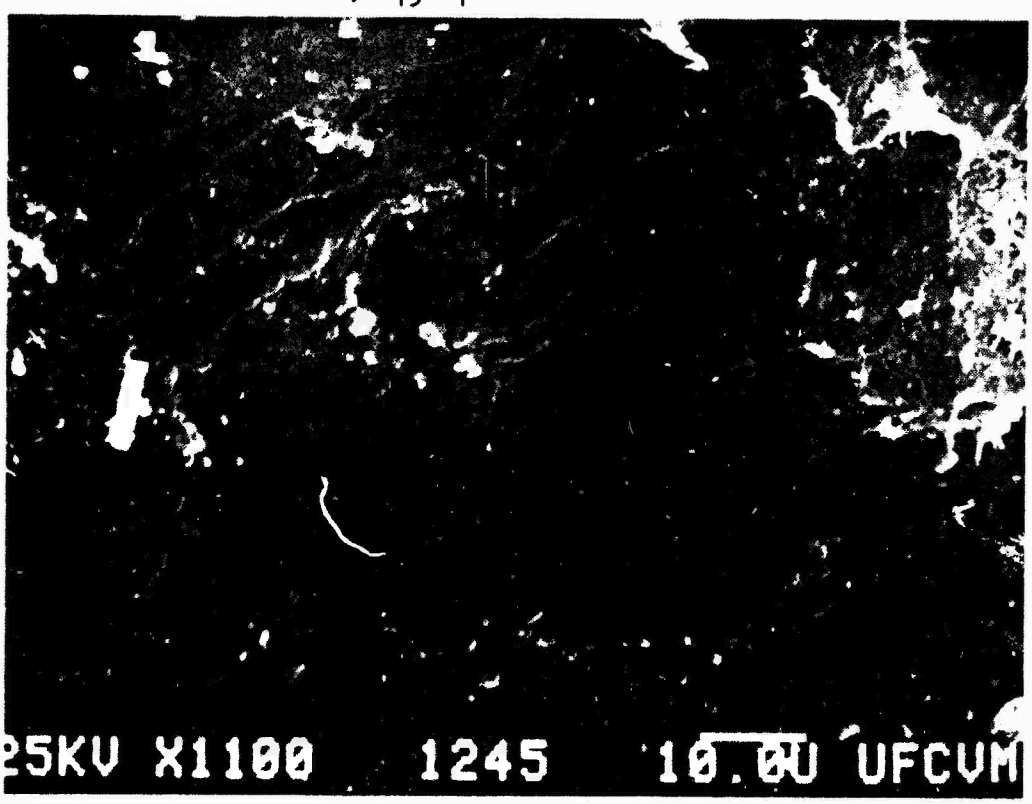

Figure 94. Higher magnification of figure 93.

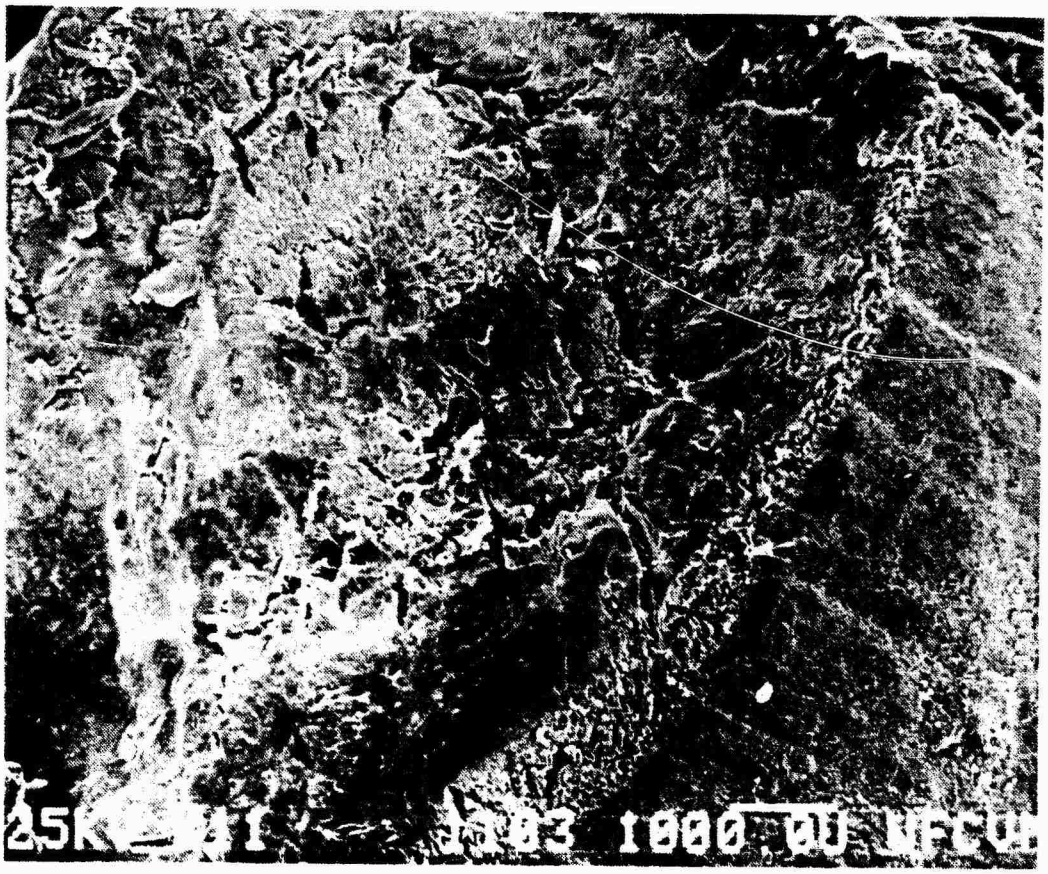

Figure 95. SEM of the articular surface of a control baboon. H18, T_{11-12}.

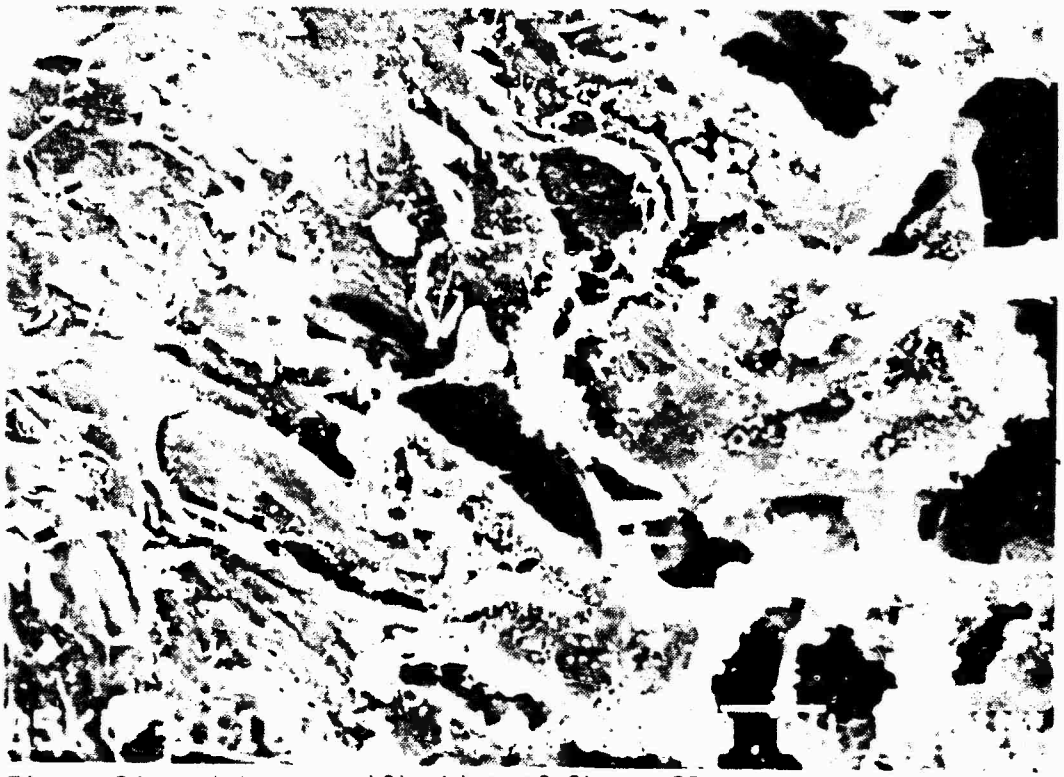

Figure 96. Higher magnification of figure 95.

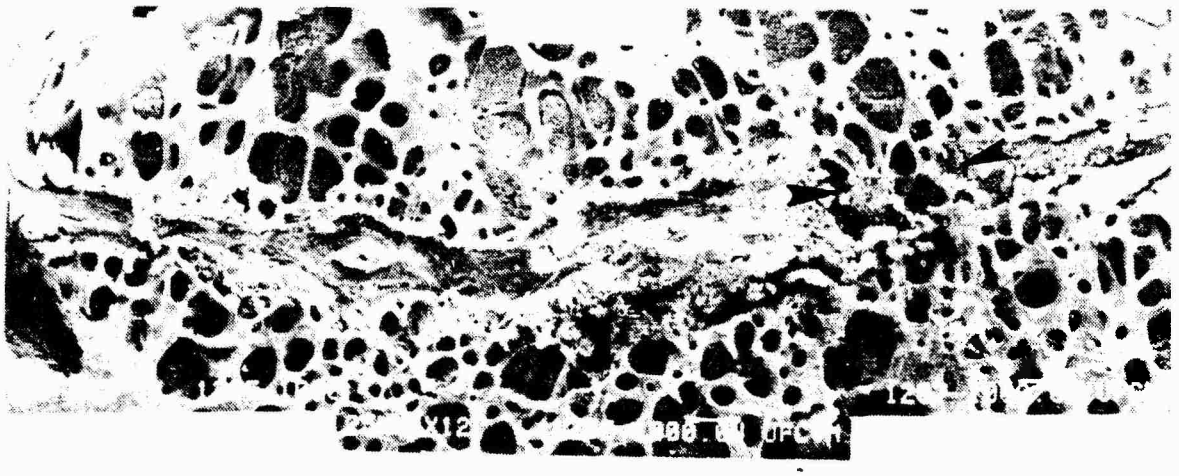

Figure 97. SEM of fused disc, L_{4-5}, H18. Trabecular bone bridging the disc space is indicated by arrows.

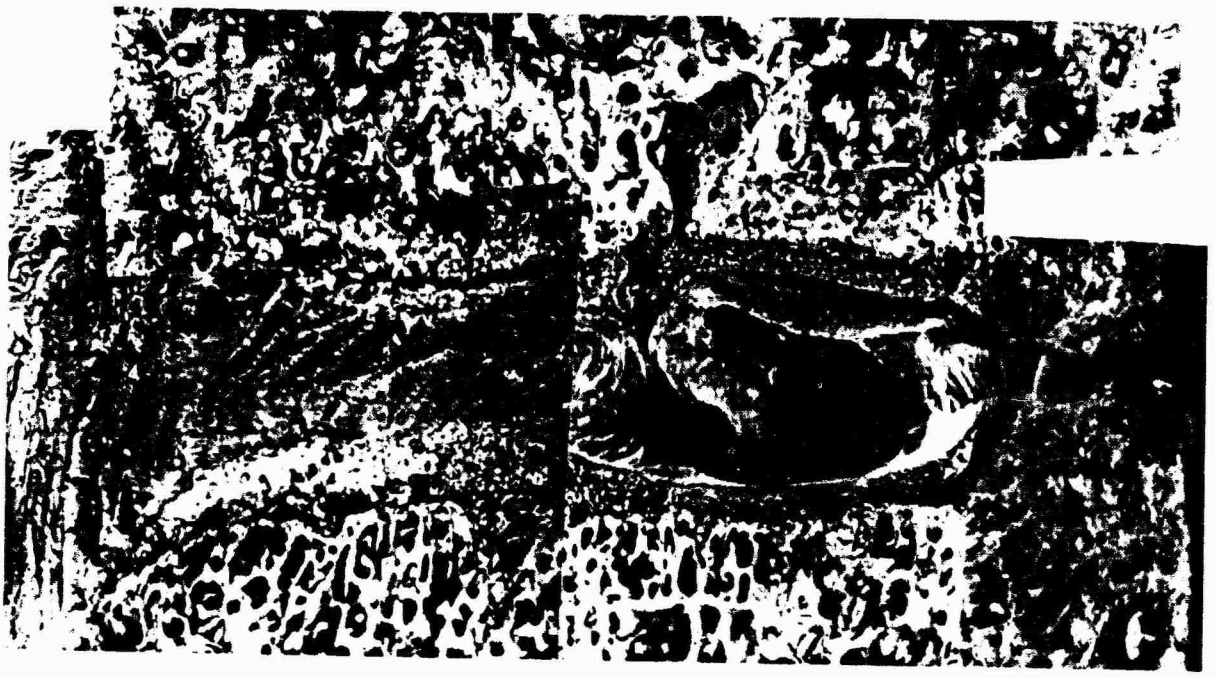

Figure 98. SEM of disc area of a control baboon. A Schmorl's node is present at S. G30, L_{2-3}.

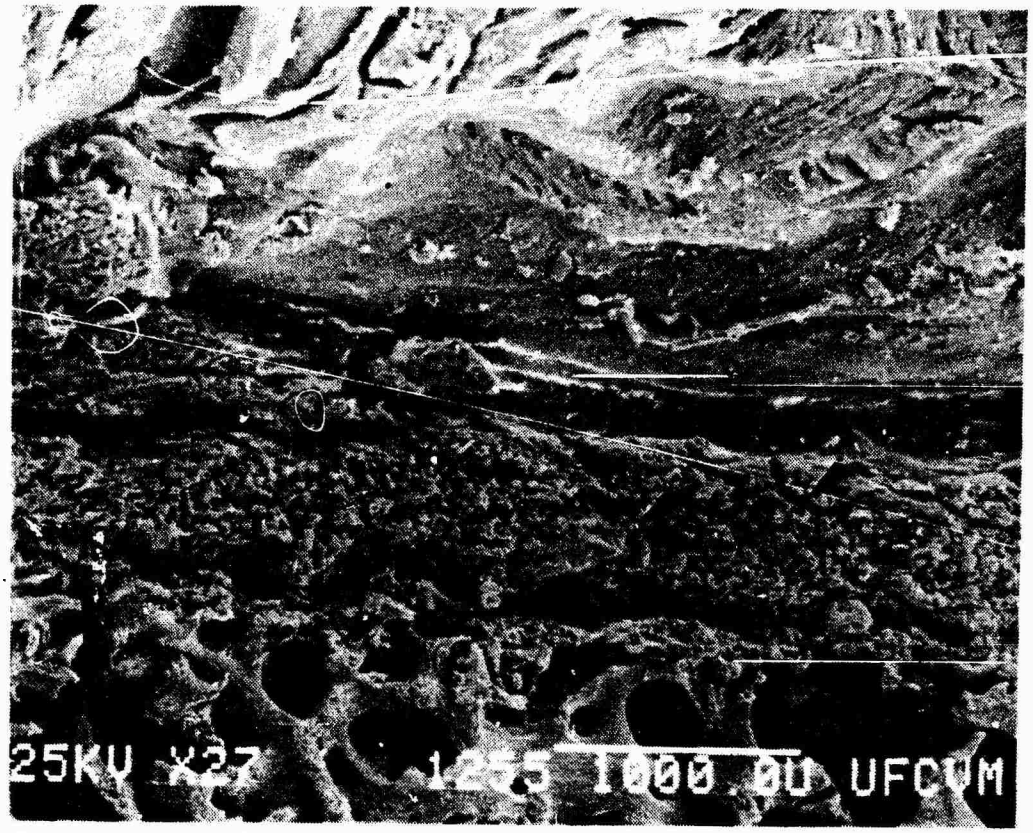

Figure 99. SEM of end plate area of an immediately post impaction baboon. Note cracks in the plate indicated by arrows. H22, L_{2-4}.

Figure 100. SEM of end plate region of one month post-impaction baboon. H 14, L_{5-6}.

Three month post-impaction group. Fractures of the cartilaginous end plate and fragmented trabeculae were also noted in this group (fig. 101).

Six month post-impaction group. A concentrated area of fractured trabeculae and debris was noted in the six month post-impaction animals. This area was observed either immediately above the nucleus pulposus (fig. 102) or just anterior to it (fig. 103). The lesions were more prominent in the lower thoracic and upper lumbar regions. The debris in the hematopoetic spaces appeared to be bone fragments.

Trabecular microfractures were present in other regions away from the nucleus, but they were few in number (1 to 3 per vertebral body). The microfractures were located near the cartilaginous end plate, and were usually in trabeculae which ran in a vertical direction. The microfractures in figures 104 and 105 appear to be healed but other microfractures (figs. 106 and 107) were still open indicating that the fractures were at different stages in the remodeling process and probably did not occur simultaneously.

The articular surface of the zygapophysial joints had a central zone of fibrillation (fig. 108). A higher magnification of this fibrillation is shown in figure 109.

Six years post-impaction group. The anterior surface of several vertebral bodies had protruding osteophytes (fig. 110). These osteophytes frequently bridged the intervertebral disc space. Bony fragments were observed in the intervertebral disc (fig. 111). Fractures through the cartilaginous end plate were a consistent finding (figs. 112 and 113).

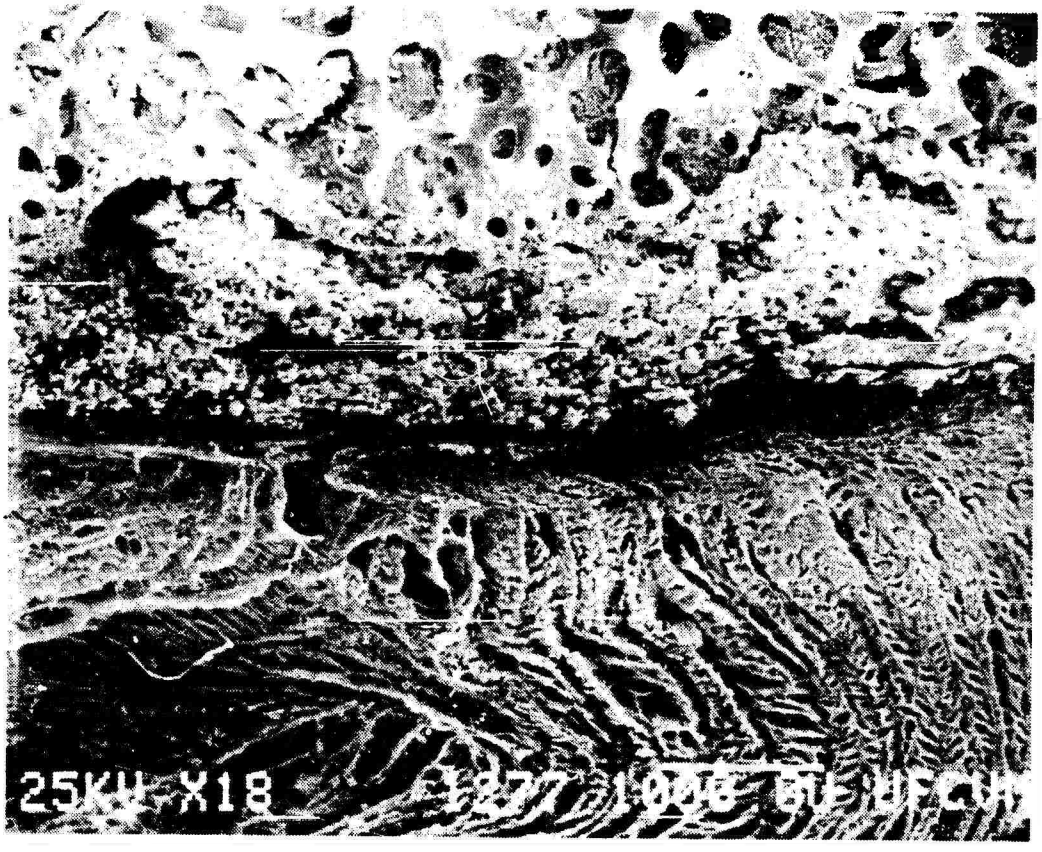

Figure 101. SEM of the cartilaginous end plate of a three month post-impaction animal. H10, L5-6

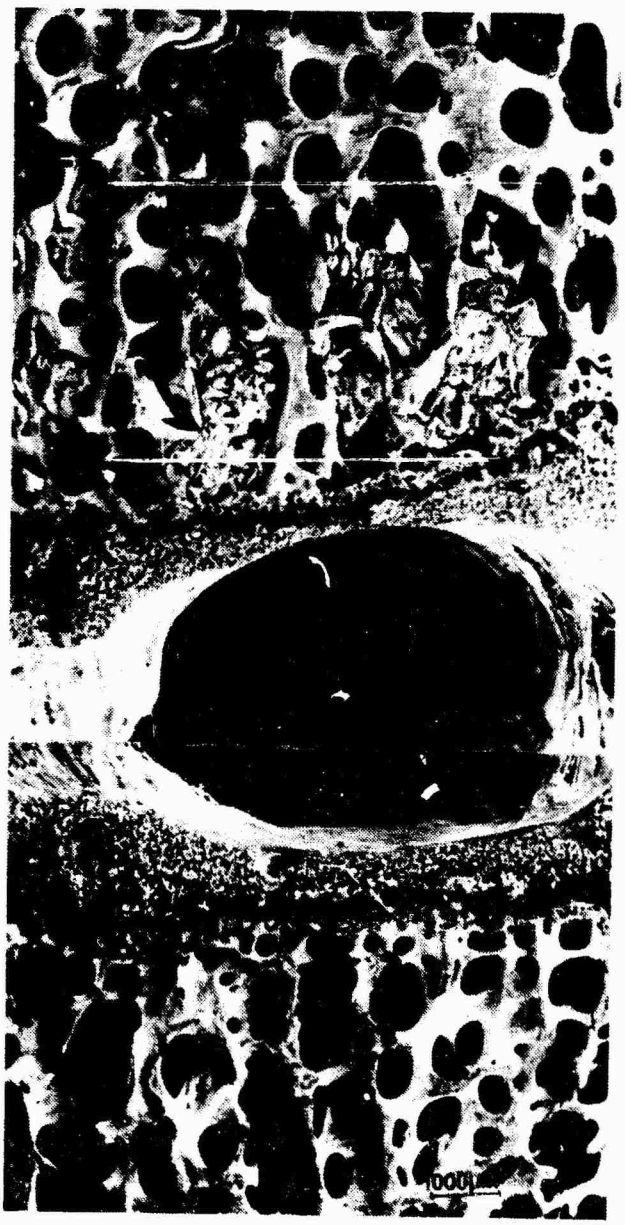

Figure 102. SEM of caudal disc region. The arrows indicate a concentrated area of fractured trabeculae and debris over the nucleus pulposus. G74, L_{1-2}.

Figure 103. SEM of the caudal end zone of L_3 just anterior to the nucleus pulposus. Note concentration of debris in this region. G74, L_{3-4}.

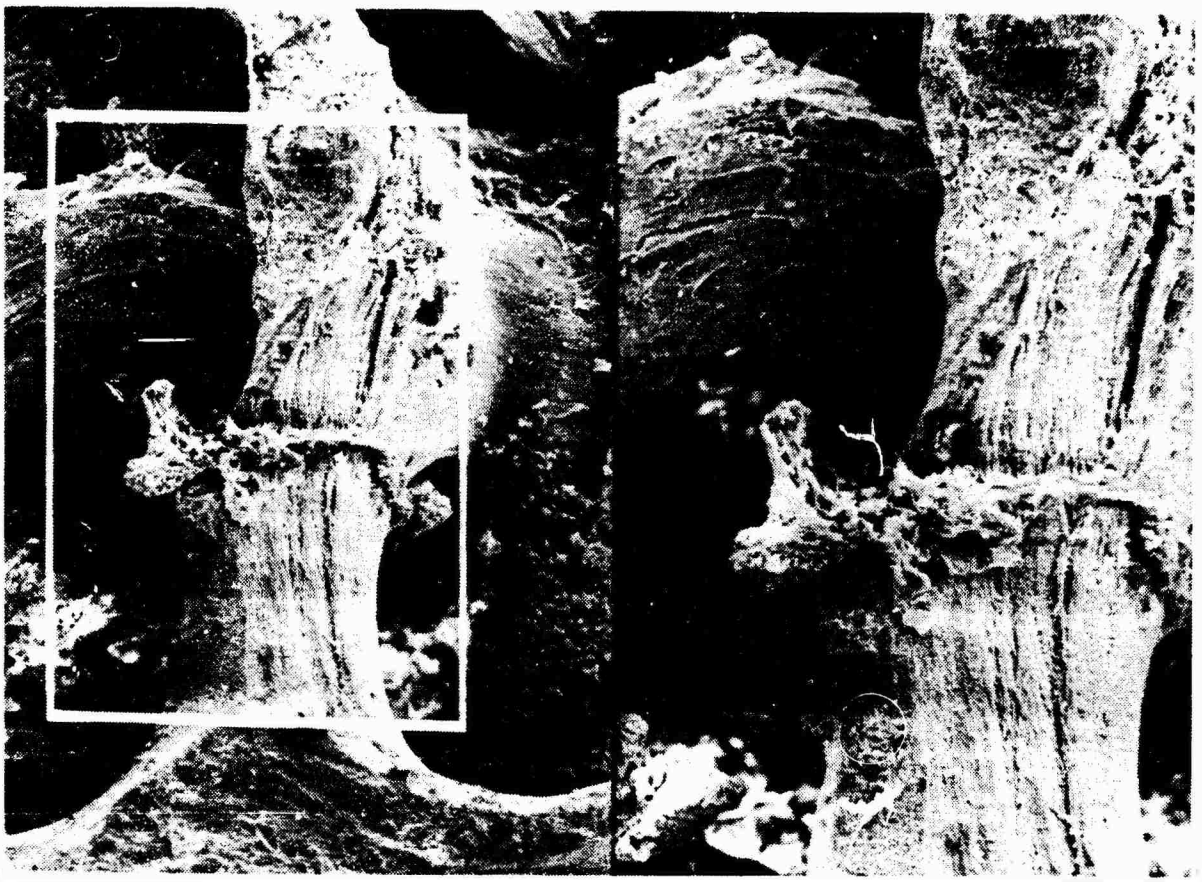

Figure 104. SEM of end zone near disc. Healed microfracture is present. G74, L_3.

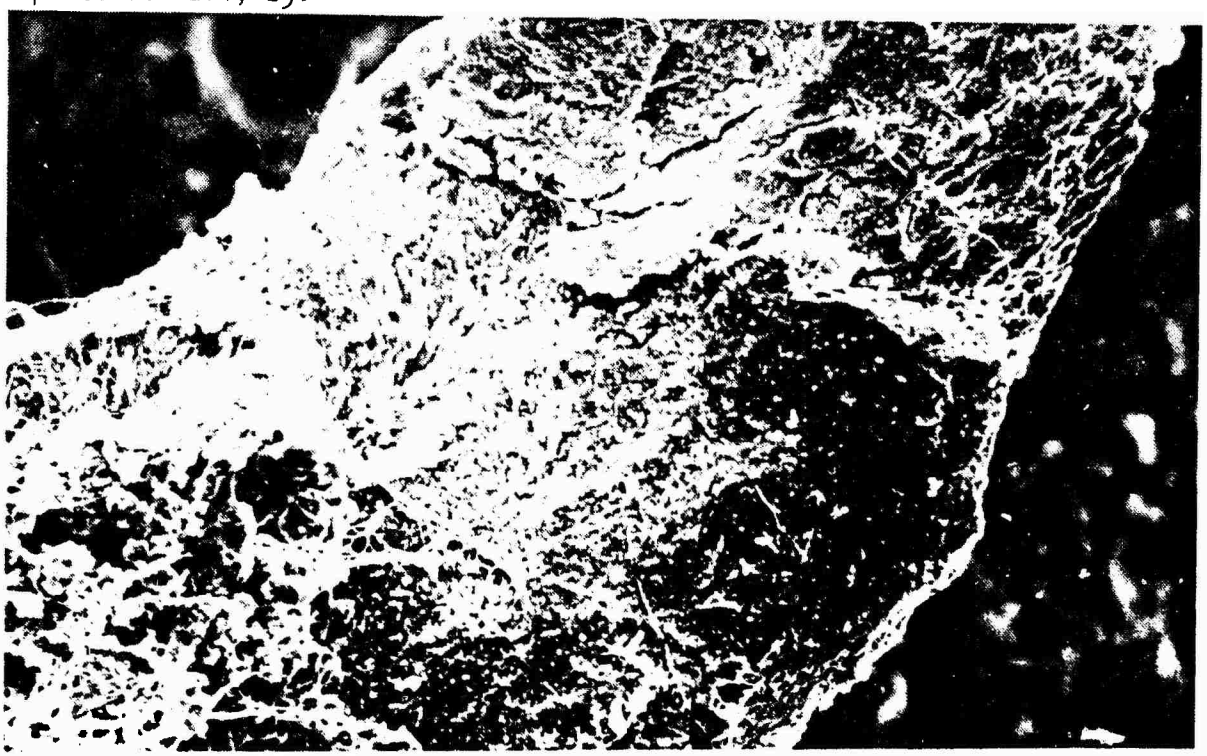

Figure 105. SEM of another healed microfracture which is further remodeled than the one above in figure 104. G84, T_{12}-L_1.

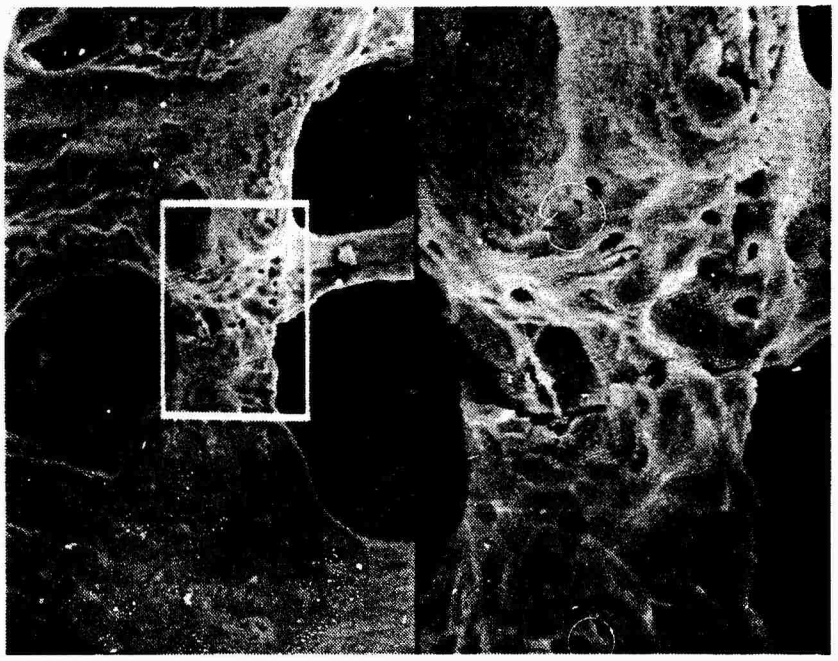

Figure 106. SEM of an open microfracture which occurred at 90 degrees to the disc. G74, T_{12}-L_1.

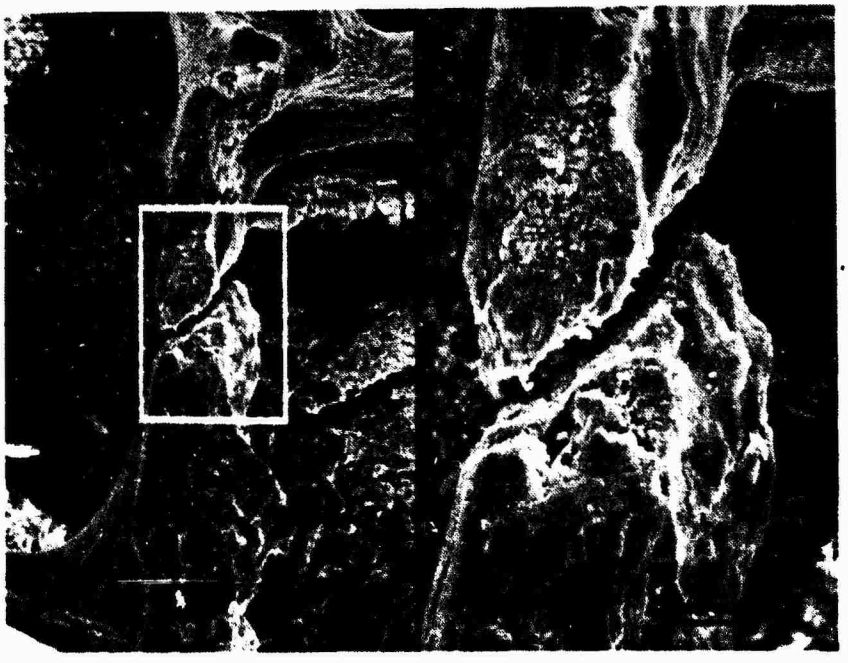

Figure 107. SEM of an open microfracture which occurred at 45 degrees to the disc. G74, T_{12}-L_1.

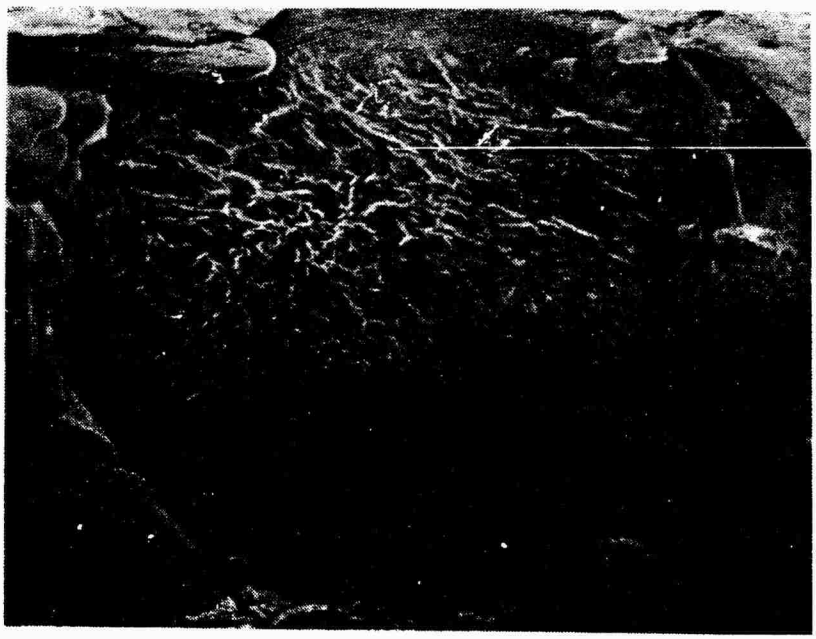

Figure 108. Articular cartilage of a zygapophysial joint from a six month post-impaction baboon. G74, 14X.

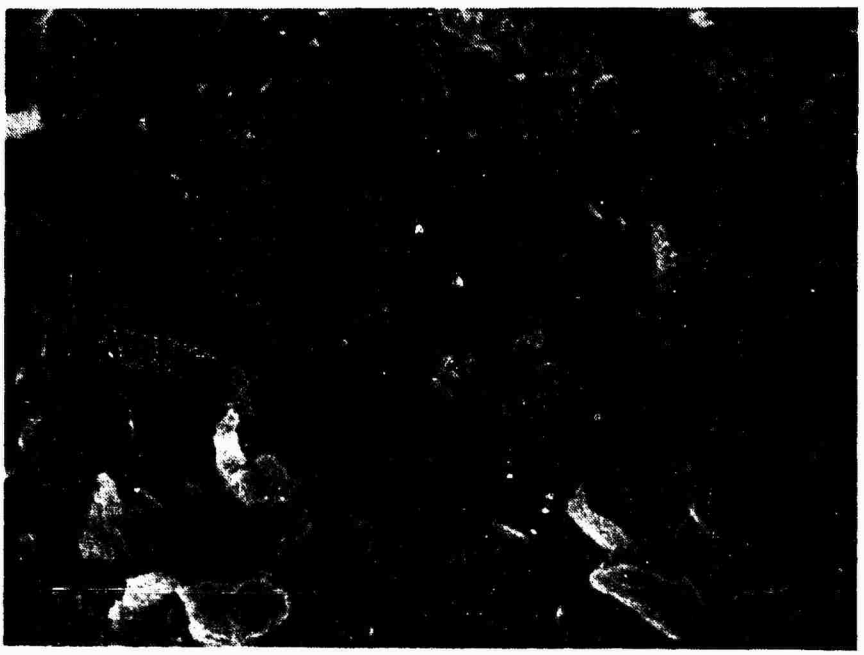

Figure 109. Higher magnification of central fibrillated region shown in figure 108. F74, 675X.

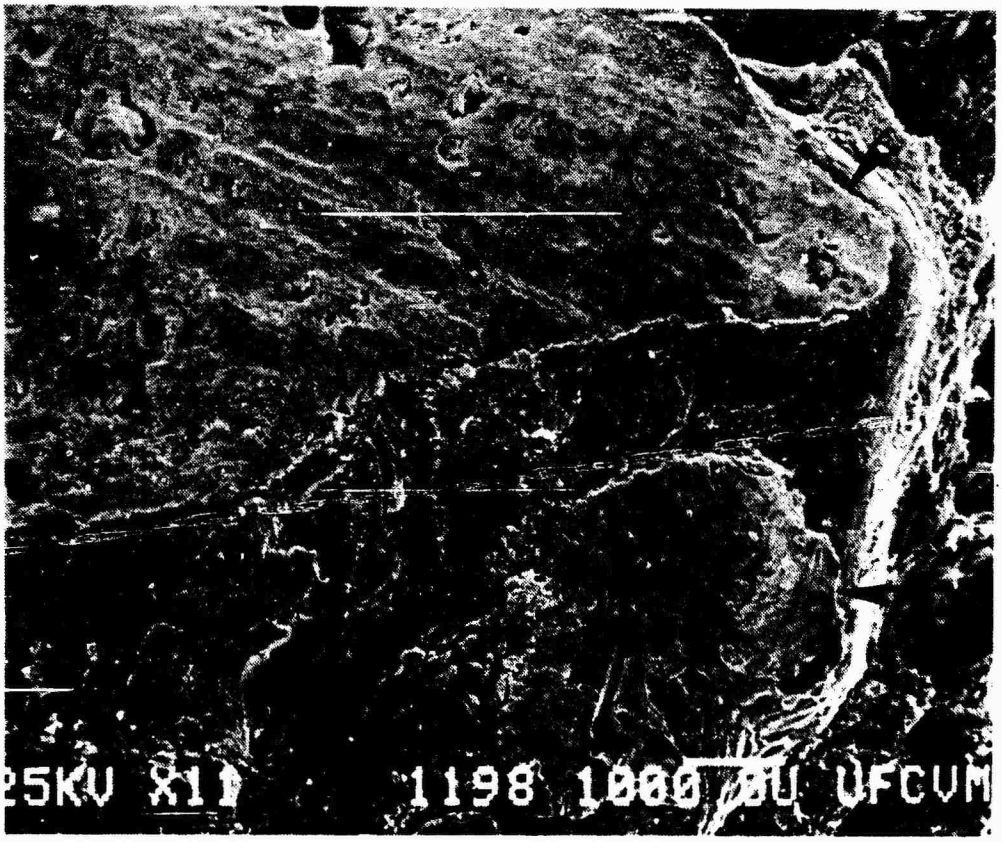

Figure 110. The anterior surface of L_5 from a six year post-impaction baboon (E18). Osteophytes are indicated by arrows.

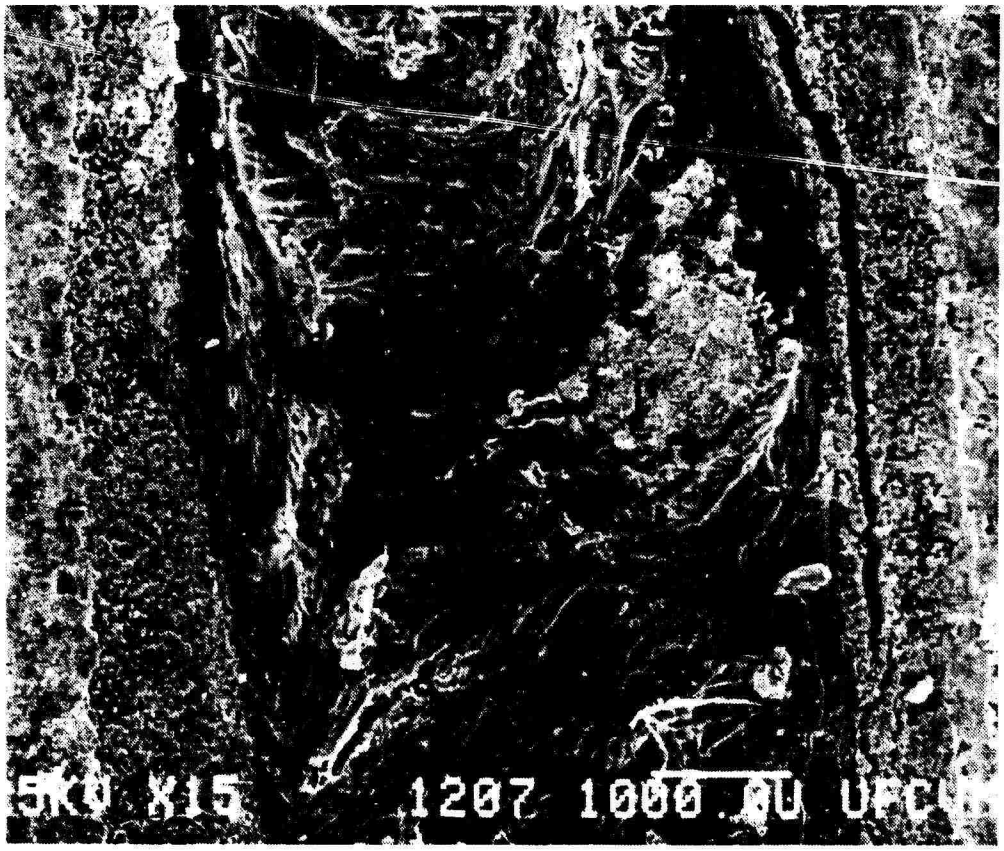

Figure 111. Bony fragments in the intervertebral disc of a six year post-impaction baboon. E18, L_{5-6}.

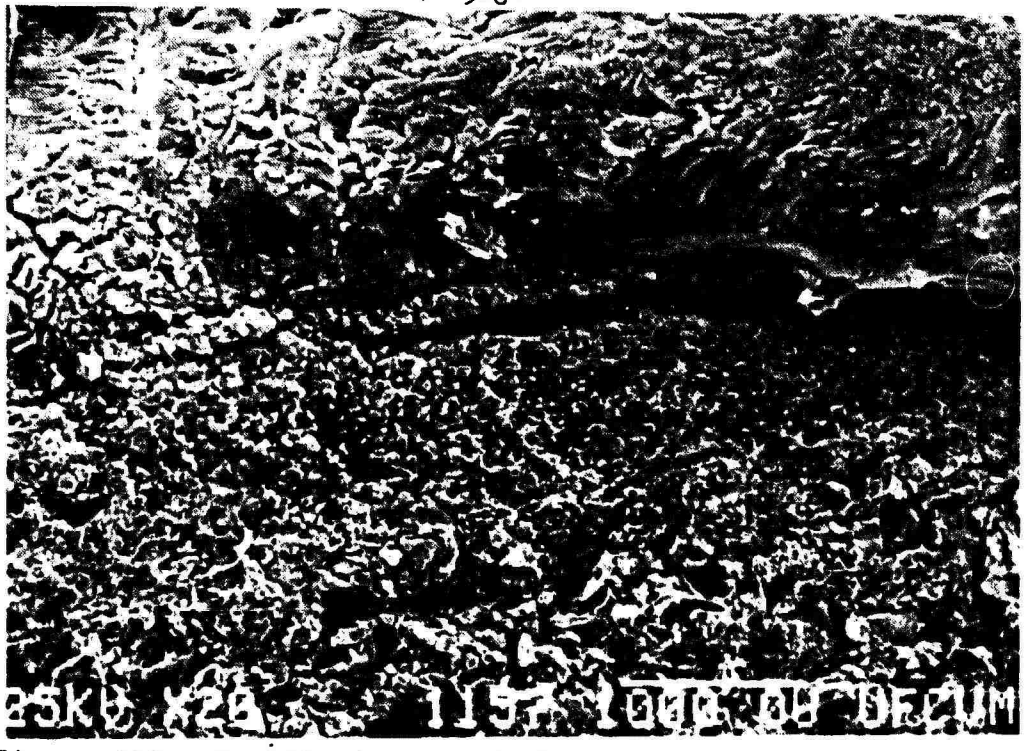

Figure 112. Cartilaginous end plate of a six year post-impaction baboon. E18, T_{1-2}.

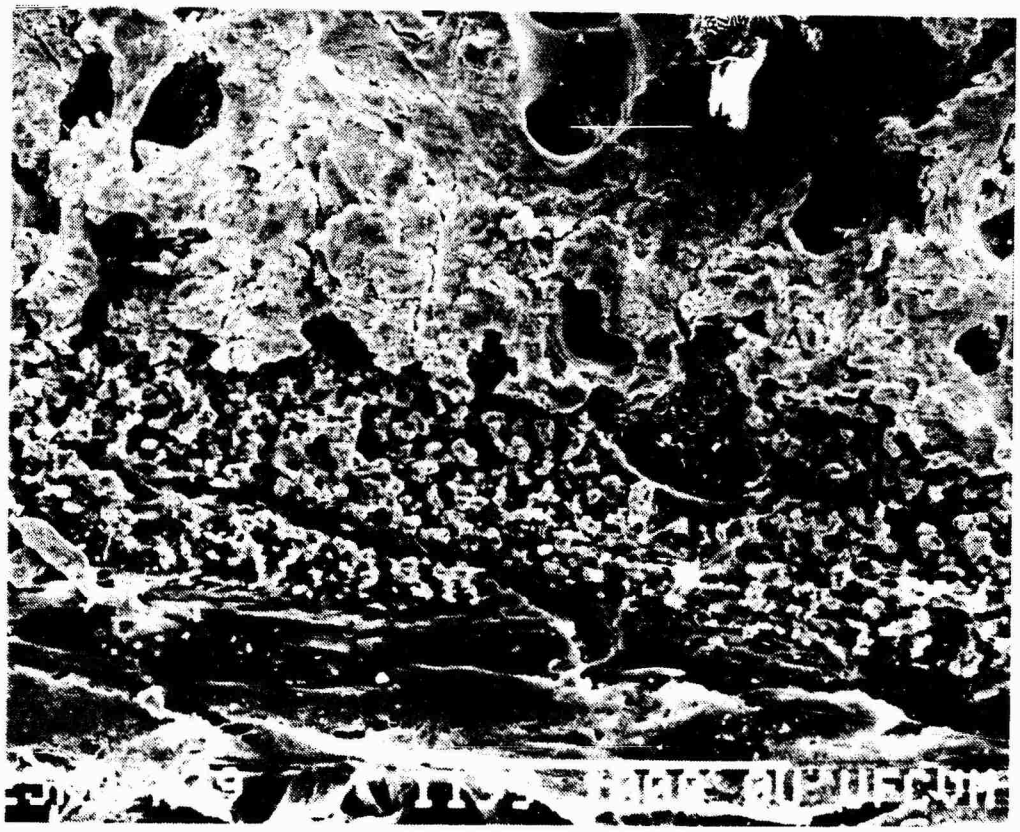

Figure 113. Cartilaginous end plate of a six year post-impaction baboon. E18, L_{5-6}.

The articular surfaces of the zygapophysial joints were severely fibrillated (fig. 114). At higher magnification, the collagen fibers were clearly visible (fig. 115).

Light microscopy. Control group. Animal G82 had a normal appearing intervertebral disc with an intact annulus fibrosus. The nucleus pulposus was lost during tissue processing.

The cartilaginous end plates of the vertebral bodies were undisrupted. An annular epiphysis was present in the anterior portion of both the superior and inferior end plates. The annular epiphysis was partially fused with the superior body via extensions of trabecular bone (fig. 116). The outer articular zone of the end plate had two regions as noted with SEM. The superficial region of the articular zone consisted of cartilage with scattered chondrocytes in oval lacunae (fig. 117). The matrix of this region was eosinophilic and homogeneous. This region was approximately 0.25 mm thick. With Alcian blue-van Gieson (AB-VG) stain, the matrix of this region was strongly red and the chondrocytes had pale green cytoplasm with a yellow nucleus. The deep region of the articular zone consisted of basophilic islands of calcification surrounded by a lamina limitans. Outside the lamina limitans were lighter eosinophilic regions which separated the calcification islands. The matrix of the eosinophilic regions was homogeneous and chondrocytes were present. With AB-VG stain, the calcified areas near the superficial region were red. In the deeper portion of the region, the calcified areas were blue-green and occasional red chondrocytes were noted. This region was about 0.75 mm thick.

Figure 114. The articular surface of a zygapophysial joint from a six year post-impaction baboon. E18, L_6 inferior.

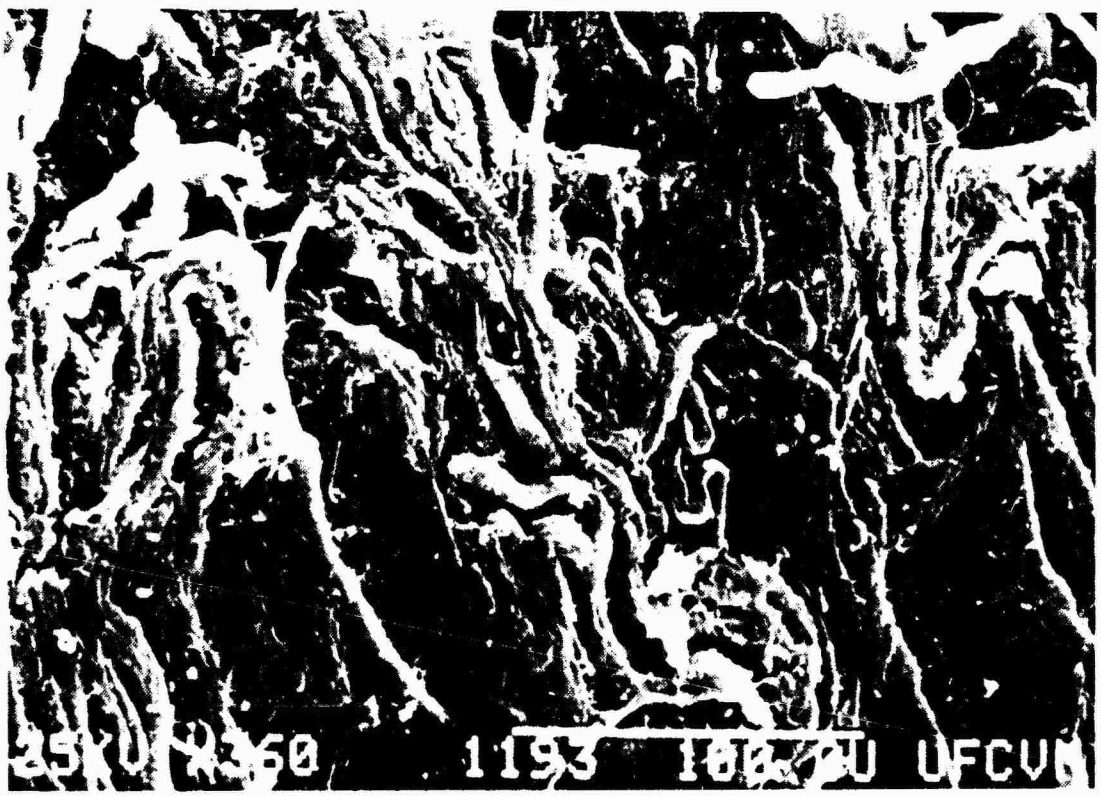

Figure 115. Higher magnification of figure 114.

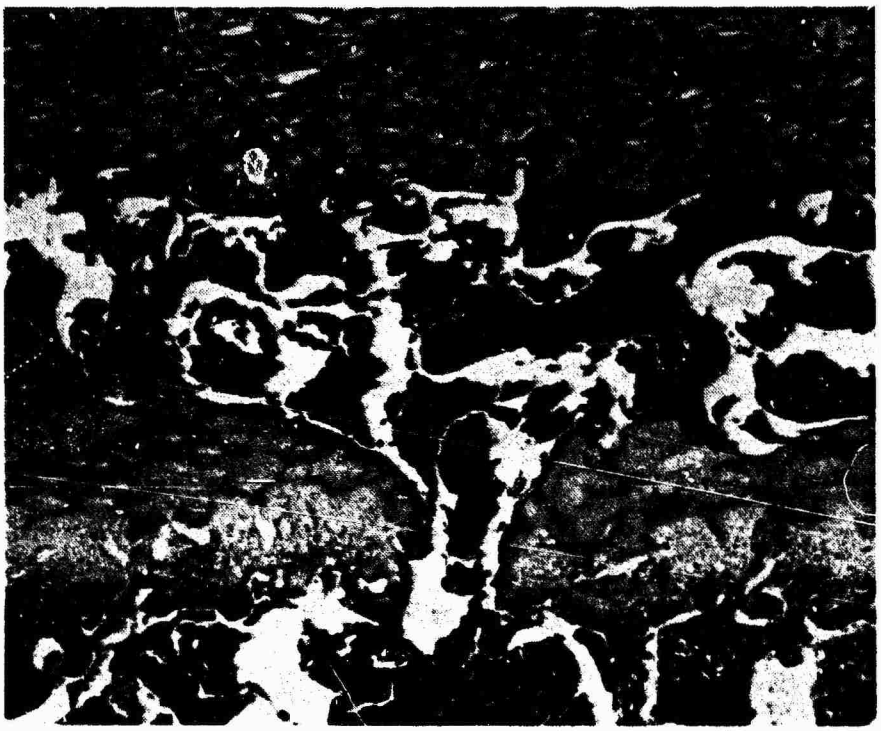

Figure 116. The annular epiphysis of a control baboon. Note the extension of the epiphysis to the underlying vertebral body (arrow). G82, upper lumbar region.

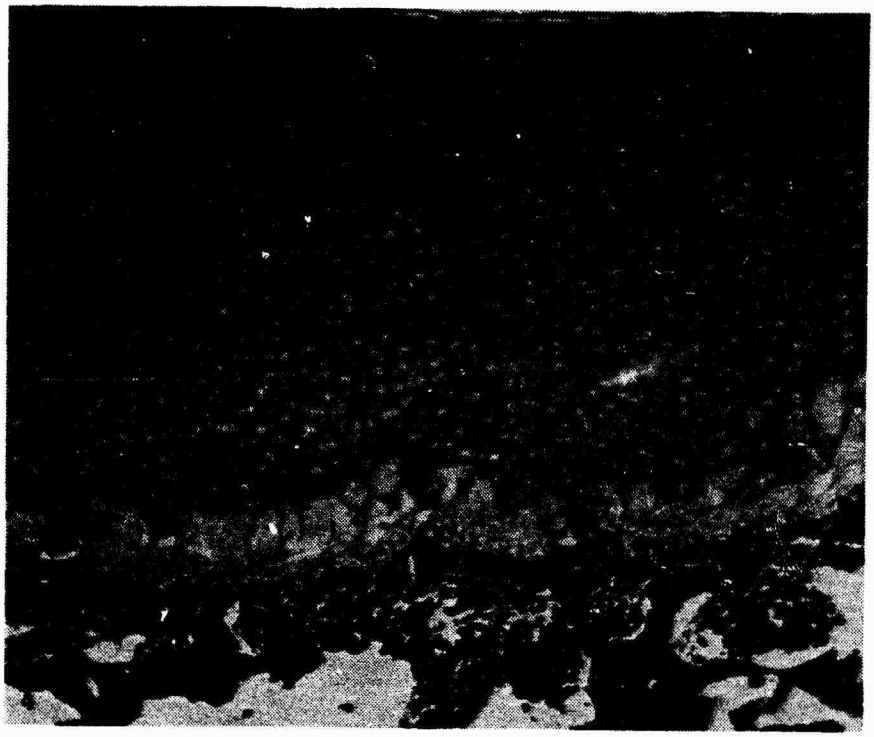

Figure 117. The cartilaginous end plate of a control baboon. 1=superficial region of articular zone; 2=deep region of articular zone; 3=growth zone; 4=trabecular bone of the vertebral body. G82, upper lumbar region.

Beneath the articular zone was a growth zone which was similar in appearance to the cartilaginous growth plate of long bones (fig. 118). Chondrocytes of the upper growth zone were arranged in columns. The cells in the upper part of the columns were flattened while those in the lower part of the columns were hypertrophied. The matrix between the cell columns was palely eosinophilic with hematoxylin and eosin stain and plate lavender with AB-VG stain. The region of cell columns was about 0.25 mm wide. The balance of the growth zone adjacent to trabecular bone was strongly basophilic and chondrocytes were absent. With AB-VG stain, the matrix was bright blue-green. This area of calcified cartilage was approximately 0.10 mm wide. Underlying trabecular bone of the vertebral bodies was strongly eosinophilic.

Scattered regions of cartilage with embryonic blood vessels were noted in some samples (fig. 119). These areas passed vertically through the cartilaginous end plate and were usually associated with areas adjacent to the nucleus pulposus.

Blood vessels were observed at the base of the growth zone of the cartilage plate in contact with the calcified cartilage. The vessels resembled metaphyseal vessels of long bones (fig. 120).

The zygapophysial joint articular cartilage was rough on the surface. The cells were arranged in clusters, and no tidemark was present (fig. 121).

Animal G30 had intact discs and end plates. The growth zone noted in the previous animal was absent in the lumbar region but inconsistently present in the upper thoracic area (fig. 122). In the lumbar area, the calcified articular zone of the end plate was in contact with the underlying bone of the vertebral body. The bony end

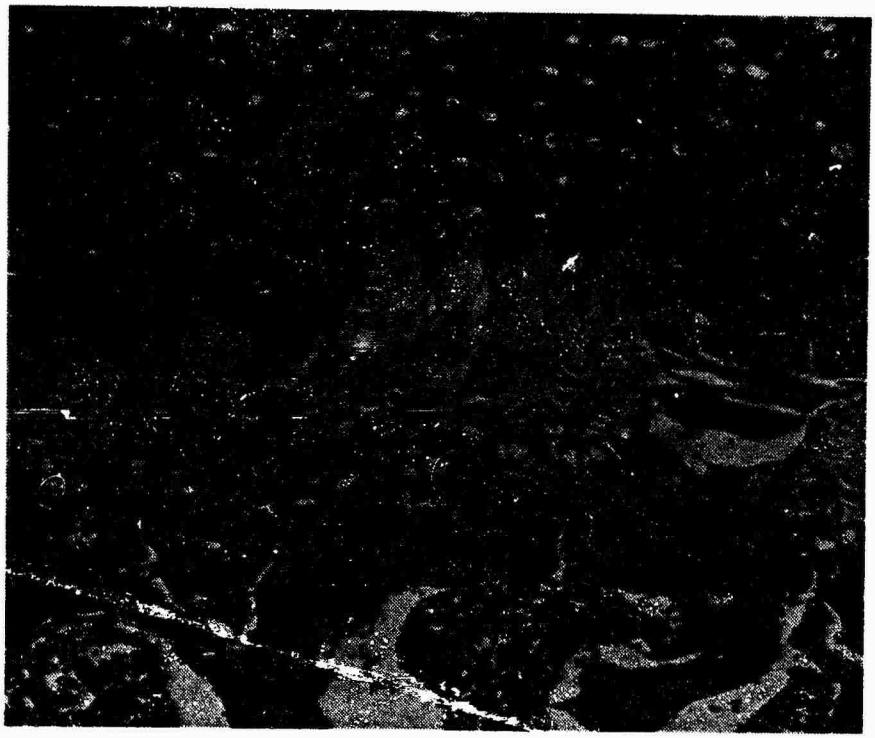

Figure 118. Higher magnification of the growth zone of the cartilaginous end plate. A=region of chondrocyte columns; B=calcified cartilage; C=bone of vertebral body. G82, upper lumbar region.

Figure 119. Cartilage associated with embryonic blood vessel remnants which traverses the cartilaginous end plate. G82, upper lumbar region.

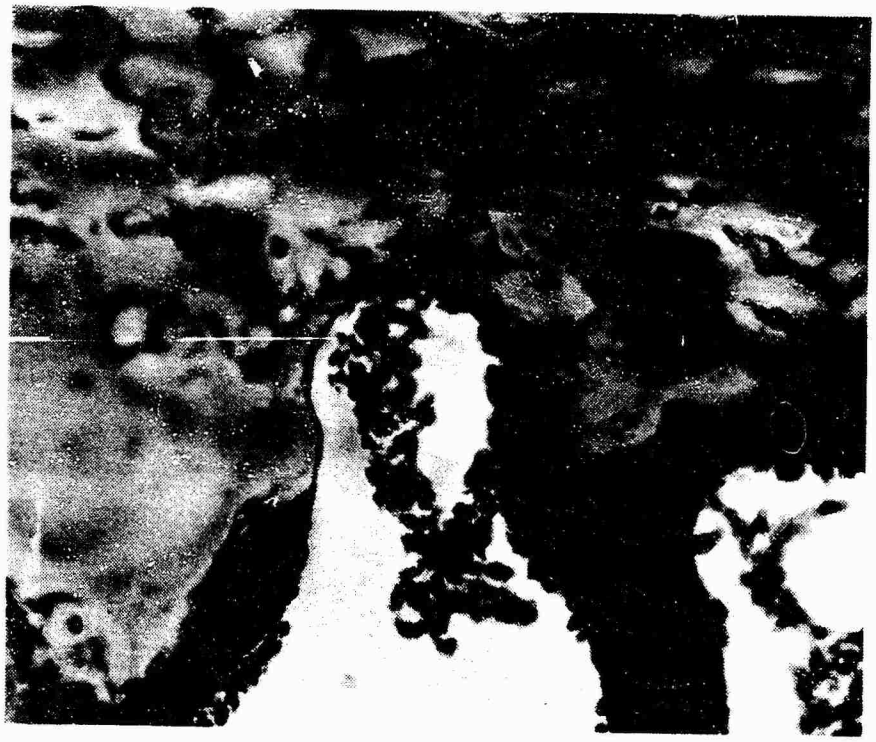

Figure 120. Blood vessels at the base of the growth zone of the cartilaginous end plate. G30, T_{6-9}.

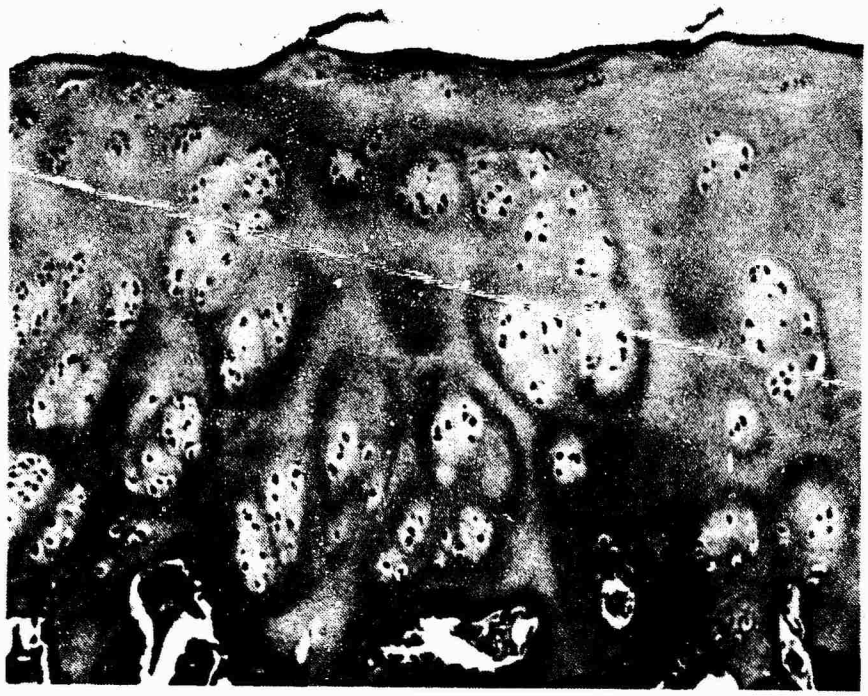

Figure 121. The articular cartilage of the zygapophysial joint from a control baboon. G82, upper lumbar region.

Figure 122. Cartilaginous end plate of control baboon with inconsistent growth zone regions. G30, upper lumbar region.

plate of the vertebral body was complete except for periodic gaps in which bone marrow contacted calcified cartilage of the end plate.

No zygapophysial joints were collected from this animal.

Animal H18 had a fused intervertebral disc at L_{4-5} (fig. 123). Bone crossed the narrowed disc space in several locations. Small areas of cartilaginous end plate were present but they were localized. The architecture of the annulus was disrupted and replaced by irregularly arranged, dense connective tissue.

The articular cartilage of the zygapophysial joints had a fibrillated surface, the cells were clustered in groups, and multiple tidemarks were present (fig. 124).

Only zygapophysial joints were collected for animal H12. The articular cartilage had been converted to fibrocartilage (fig. 125) and multiple tidemarks were present in the samples examined.

Immediate post-impaction group. The cartilaginous end plate of the immediate post-impaction animals had areas of separation through the upper growth zone which was still present in both H20 and H22 (fig. 126). The trabeculae under the end plate were fragmented.

All of the zygapophysial joints had fibrocartilage on their articular surfaces, and multiple tidemarks were present deep in the cartilage. Animal H24 had five tidemarks while animal H22 had two.

One month post-impaction group. The anterior vertebral column of only one animal (H14) in this group was examined with light microscopy because it was abnormal radiographically. A small osteophyte was present at the junction of L_{4-5}, and other levels had fibrocartilage and increased basophilia along the anterior border of

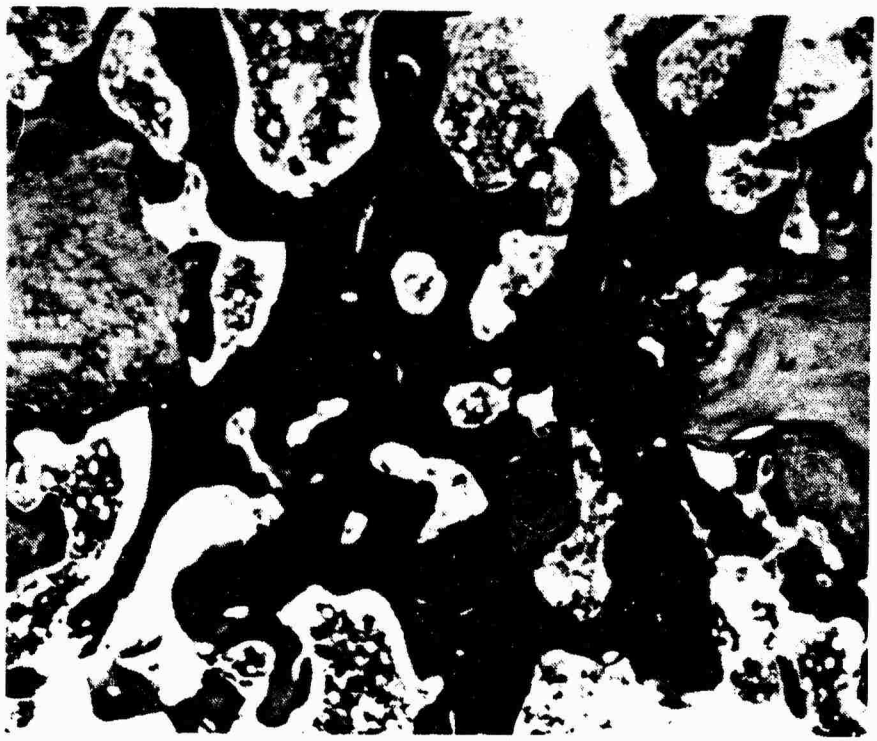

Figure 123. Fused intervertebral disc of one control baboon. H18, L_{4-5}.

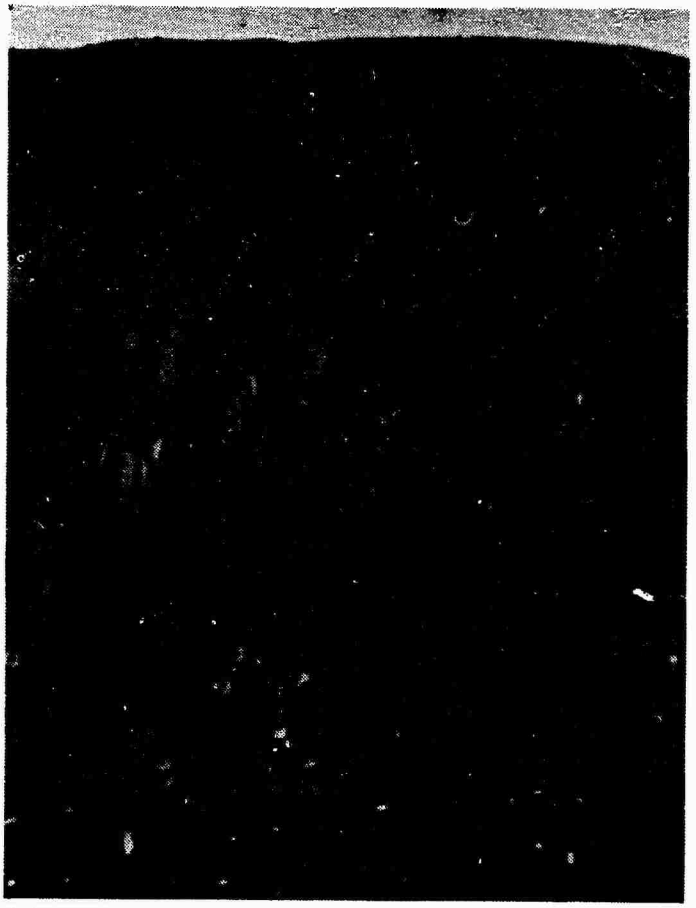

Figure 124. Articular cartilage of control baboon. Arrows indicate multiple tidemarks. H18, T_{12-13}.

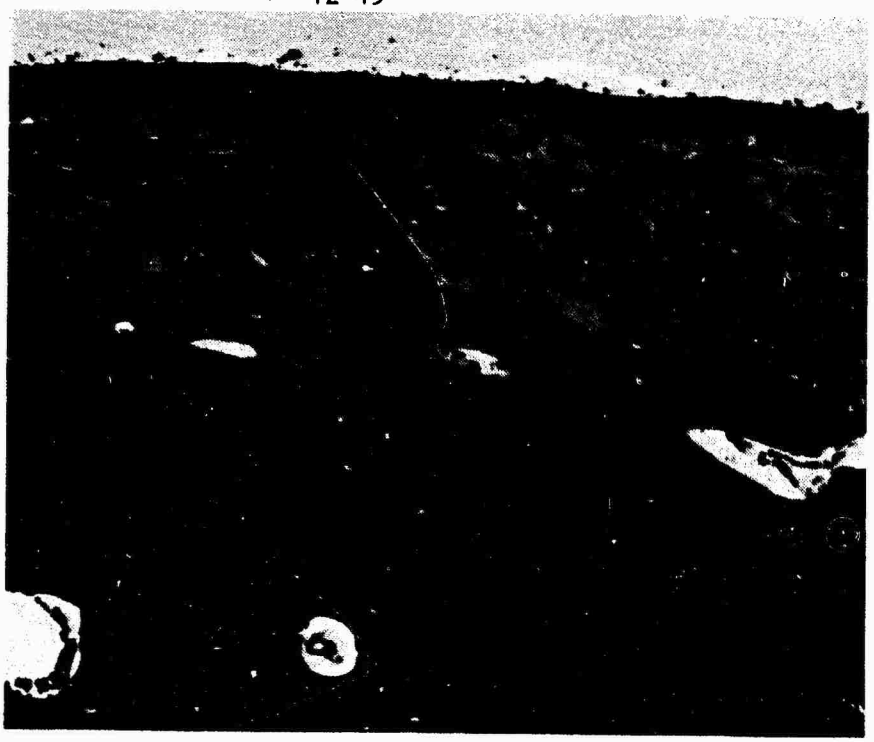

Figure 125. Fibrocartilaginous articular cartilage of a control baboon. H12, L_{1-2}.

Figure 126. Cartilaginous end plate of an immediate post-impaction baboon. Arrows indicate area of separation through the upper growth plate. H20, L_{5-6}.

the vertebral bodies near the disc. The articular cartilage was moderately fibrillated and the chondrocytes were clumped.

Three months post-impaction group (H10). The cartilaginous end plates were intact as were the intervertebral discs and trabecular bone of the vertebral bodies. The articular cartilage of the zygapophysial joint had prominent eosinophilic fibers in the upper zone.

Six months post-impaction group. Growth zones were present in the cartilaginous end plate of three animals in this group. The cartilage in this area was very disrupted with fragments of bone present in at least one animal (G84). Along the anterior cortex of the vertebral bodies in areas adjacent to the disc, cartilage was forming underneath the periosteum (fig. 127). In G74, the cartilage lacunae were closely grouped between the periosteum and cortical bone (fig. 128). The matrix was alcian blue negative. In G88, the cartilage matrix had alcian blue positive regions. Underlying cortical bone was fragmented. Numerous osteoclasts and osteoblasts were present. G84 had large hyaline cartilage nodules along the anterior border (fig. 129). Cartilage on the articular surface of the zygapophysial joints ranged from cells grouped in clusters to fibrocartilage with a fibrillated surface.

Six years post-impaction group. Both animals in this group had numerous osteophytes which bridged the intervertebral joint space (fig. 130). The growth zone of the cartilaginous end plate had closed except for an occasional remnant of hyaline cartilage. The remaining portion of the growth plate was securely attached to the

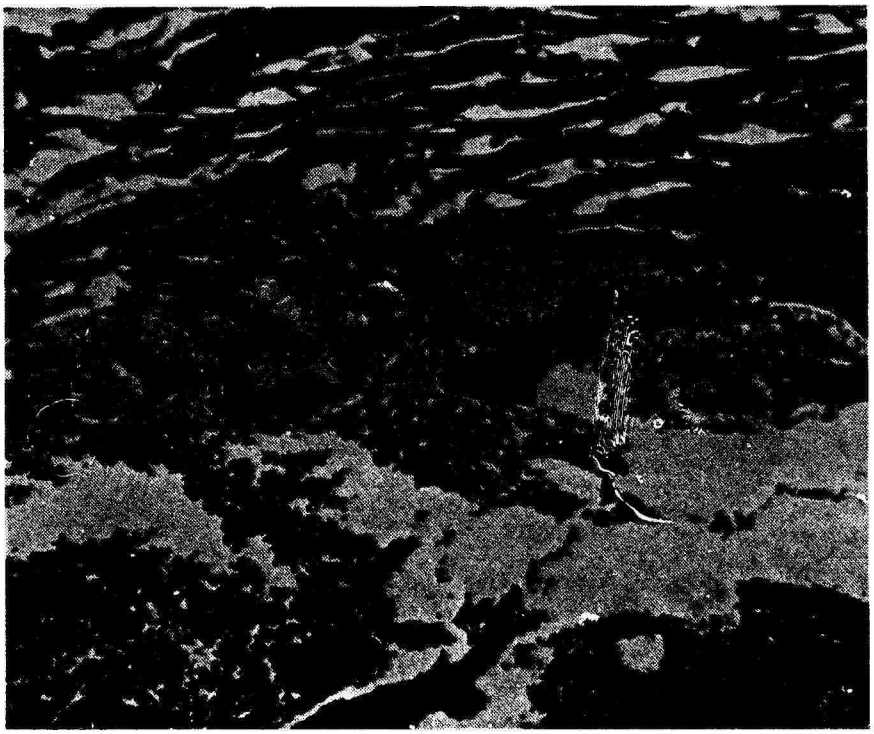

Figure 127. Areas of cartilage beneath the periosteum of a six months post-impaction animal (arrows). G88; L_4.

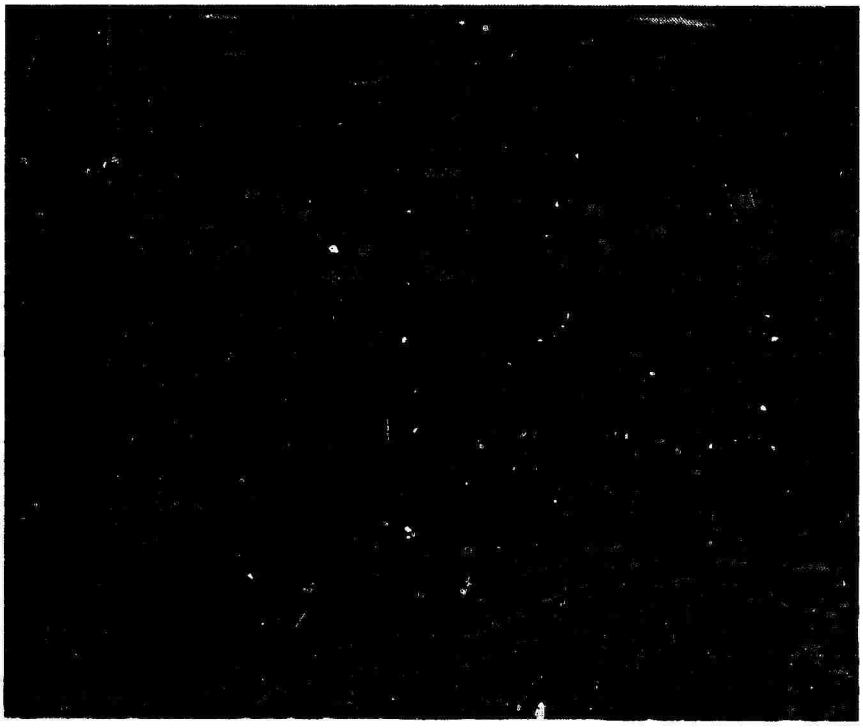

Figure 128. Chondrocytes and lacunae beneath the periosteum of a six months post-impaction baboon (arrows). G74, L_2.

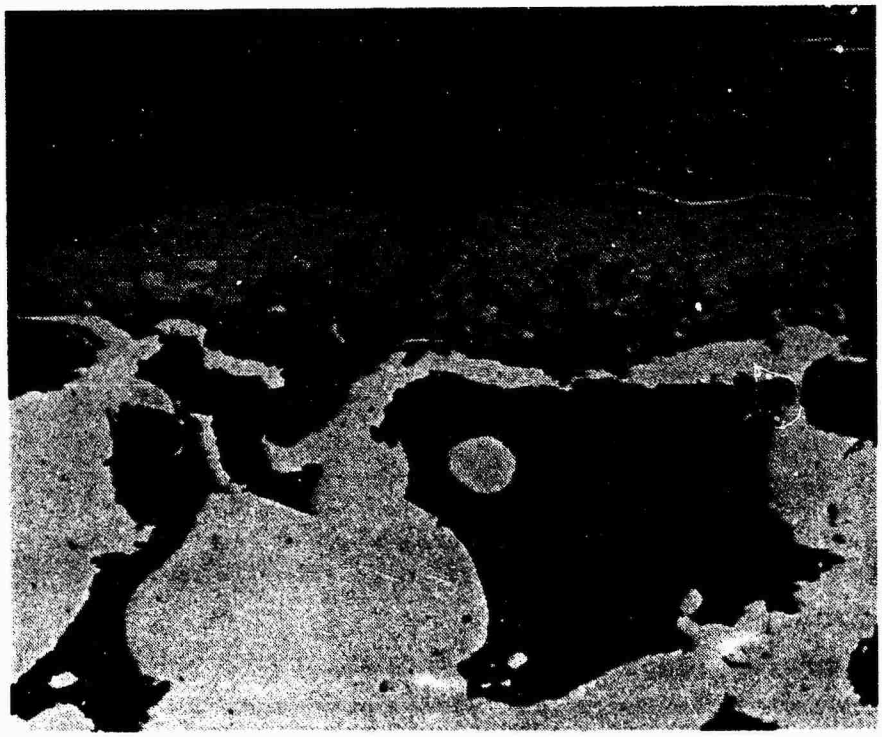

Figure 129. Large hyaline cartilage nodules along the anterior border of the vertebral body of a six months post-impaction baboon. G84, L_{3-4}.

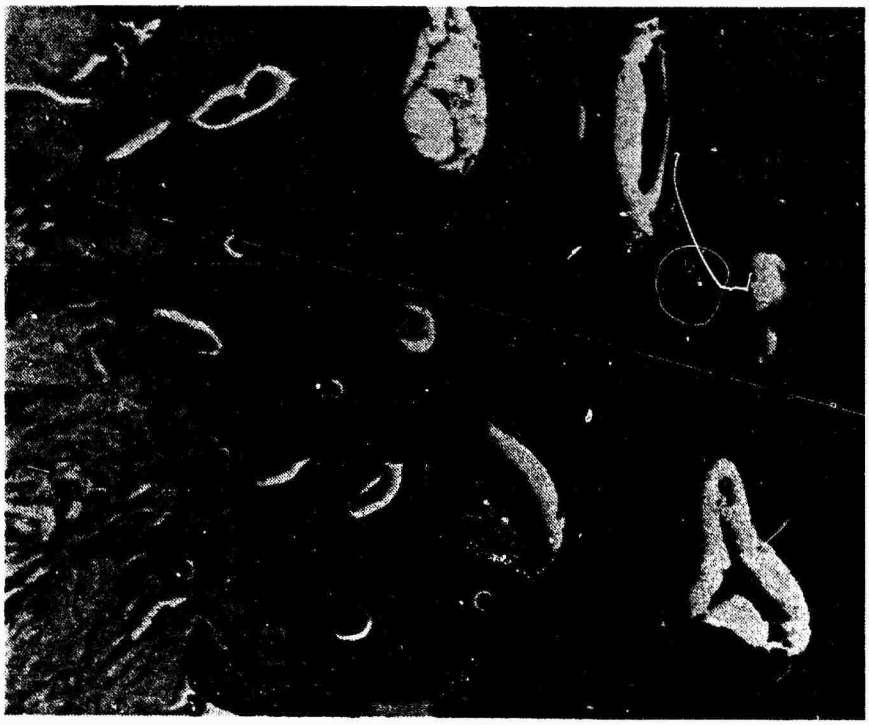

Figure 130. Anterior osteophyte of a six year post-impaction baboon. E18, L_{5-6}.

underlying bone of the vertebral body (fig. 131). The annular epiphysis was also securely fused with the vertebral body.

The articular cartilage of the zygapophysial joints was severely degenerated (fig. 132). The tissue was fibrocartilaginous, and the matrix stained yellow and pale red with AB-VG.

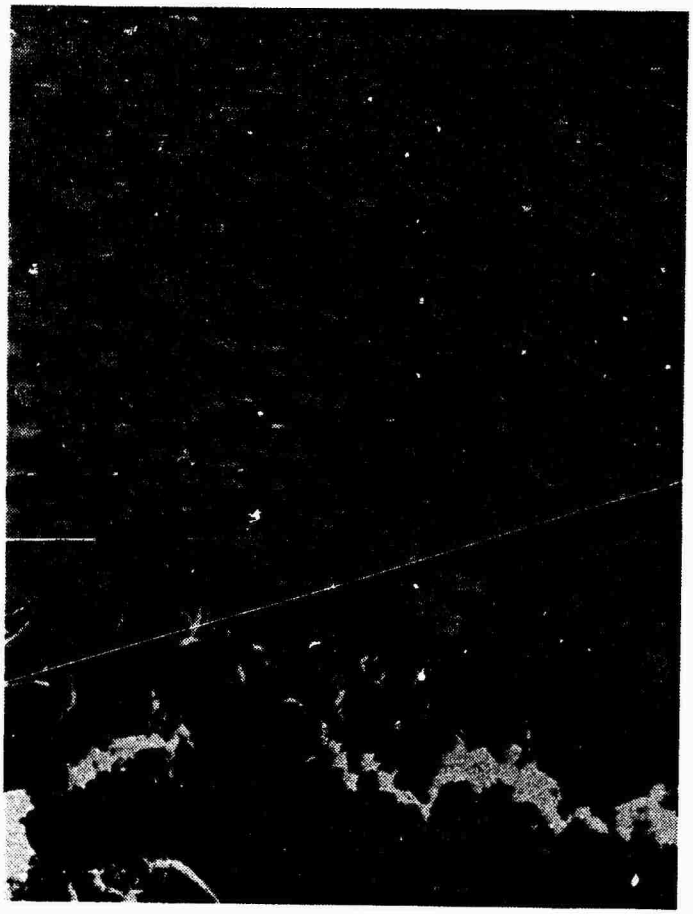

Figure 131. Junction of cartilaginous end plate and trabecular bone of the vertebral body from a six year post-impaction baboon. E34, T_{10-11}.

Figure 132. The articular cartilage of a zygapophysial joint from a six years post-impaction baboon. E34, L_5 superior.

Discussion

Based on necropsy weight and histologic appearance of the growth zone of the cartilaginous end plate, the animals were of varying ages at the time of impaction. All animals were judged to be skeletally immature at impaction.

Animals H18 and H24 both had radiographic evidence of abnormalities related to previous injuries and therefore should be excluded from the study.

The calcified articular zone of the cartilaginous plate could be clearly visualized with radiograph (fig. 86). The radiographically less dense zone beneath the articular zone and above the vertebral body corresponds to the growth zone of unmineralized hyaline cartilage. The irregular mineralization of the cartilaginous end plate of G88 corresponds with the increased mineralization noted with light microscopy. This increased mineralization is probably related to the approaching closure of the growth zone and formation of subchondral bone in that area, rather than a lesion related to the impaction sequence.

The radiographic findings of osteophytes along the anterior border of the vertebral column and zygapophysial joint degeneration were confirmed by both histopathology and scanning electron microscopy and will be discussed further below.

The structure of the baboon cartilaginous end plate was determined with SEM and LM to be similar to that of the rhesus monkey. The baboon end plate has not been described previously. The plate is unique in that it appears to serve as both an epiphysis and to contribute to growth in length of the vertebral bodies of the baboon

where many other species have a true cartilaginous growth plate for longitudinal growth underlying a bony epiphysis (Schmorl and Junghanns, 1959).

The end plate complex consists of the growth zone which eventually closes upon skeletal maturity. The annular epiphysis at the periphery of the plate fuses with the bony vertebral body at maturity as well. The remaining islands of calcification in the end plate persist beyond skeletal maturity, and bear further investigation in older animals to determine if they fuse with age to form bone.

A wide range of deterioration of the articular cartilage of the zygapophysial joints was observed in both control and impacted baboons. The clumping of cells, surface fibrillation, and matrix cracking indicated deterioration of the articular cartilage. Multiple tidemarks are a sign of progressive remodeling of osteoarthritis (Johnson, 1959), indicating that the joint deterioration observed in these animals was of a chronic nature. Although present in both control and impacted baboons, the degree of articular cartilage deterioration was most severe in the 6 years post-impaction animals. The initial cause of joint deterioration in the control animals is uncertain, but degeneration of the joints of six year post-impaction animals was probably related to changes in the anterior vertebral column (fusion, etc.) which affected the motion of the posterior joints. Vernon Roberts (1980) has reported such degenerative changes in the zygapophysial joints of humans with anterior instability of the intervertebral joint.

Evaluation of both SEM and LM seems to indicate that the impaction sequence may damage the end plate initially but that this

lesion does not persist. The separation through the upper part of the growth zone was noted immediately post-impaction, but later the end plate was tightly fused to the vertebral body. This disappearance of the gap seems to indicate that the growth zone of the end plate can be separated from the underlying bone and then continuity reestablished without long term damage to the plate or the vertebral body. Because of lack of supporting light microscopy, many of the cracks in the end plate observed with SEM in groups which were more than one month post-impaction are thought to be artifact. Traversing fractures of the cartilaginous end plate as seen in impacted spinal units were not present in the in vivo impacted baboons.

The fractured trabeculae associated with the cartilaginous end plate and the nucleus pulposus were an inconsistent finding. The fractures correlate with those found in compressed spinal units (see previous sections of this report). The location of the microfractures near the end plate and in trabeculae with a vertical direction corresponds to work reported by Hansson and Roos (1981 a and b). The predominance of the lesions in the lower thoracic and upper lumbar regions is supported by Perrey's findings (1957). Other fractures scattered through the vertebral body which were in various stages of healing probably did not occur simultaneously. Frost (1973) suggests that such microfractures occur as a result of normal physical activity. Inconsistency of the fractures suggests that there was a variation in the impaction response between animals. It is also difficult to determine if these fractures are real or an artifact of processing.

The intervertebral discs and cartilaginous end plates were intact in the post-impaction animals. The annulus was complete and no signs of extrusion of the nucleus pulposus were noted.

The appearance of cartilage under the periosteum of the anterior cortex at six months post-impaction is thought to be the initial appearance of the bridging osteophytes seen later in this area. Although the vertebrae in the test animals are still growing, bone growth in this location is normally intramembranous without cartilage formation. The stimulus for cartilage formation seems to be the impaction sequence, but the exact mechanism which causes the formation of cartilage instead of bone in this area is uncertain.

Vernon-Roberts (1980) has proposed that the osteophytes result because of disc instability, but in this case, the disc appears normal. One animal (G88) would suggest that fracture of the cortical bone is related to cartilage formation in this area. Another possibility could be damage to the vascular supply as a result of impaction trauma, resulting in cartilage formation instead of bone. In general though, the response of the tissue seems delayed when compared to other types of bone healing.

Based on the above observations, it would seem that upon impaction of animals with skeletally immature vertebral columns, the growth zone of the cartilaginous end plate deforms by splitting through the upper region. The anterior cortices of the vertebral bodies are traumatized such that cartilage begins to form under the periosteum. The growth zone lesion resolves and no long term effects result, but the hyaline cartilage along the cortices progresses to form significant osteophytes which impair the function of the

intervertebral disc and zygapophysial joints. The effect of impaction on skeletally mature individuals without the growth zone to absorb the effects of the trauma may result in more severe damage to the disc and a different injury pattern.

THE HISTOMORPHOMETRY OF RHESUS MONKEYS EXPOSED TO HYPOKINESIA

Introduction and Literature Review

The expanding use of space as an operational area with development of a space station, advanced aircraft, and weapon systems and continuing space shuttle flights has raised many questions related to human safety and productivity in space (Dietlein, et al., 1983). Of primary concern is the skeletal system which has been shown to lose significant amounts of bone mineral when exposed to weightlessness (Hattner and McMillan, 1968; Berry, 1969; Pace, 1977; Tilton, et al., 1980). The skeletal dynamics of this bone loss are poorly understood. Major areas of concern are: 1) the time required until bone loss plateaus, 2) the possibility of irreversible bone loss, 3) the possible toxic effects of released calcium and phosphate on soft tissues such as the kidney, and 4) the potential for fractures as a result of impact loading or torsional stress (Dietlein, et al., 1983).

Studies of laboratory animals following spaceflight have shown bone losses similar to those found in human astronauts. Decreased bone density was noted radiographically at several body sites in the pigtail monkey (Macaca nemestrina) following 8.8 days in space (Mack, 1971). Osteoporosis of the metaphysis combined with decreased trabecular bone was present in young rats flown in space for 22 days (Yagodovsky, et al., 1976). Other studies of young rats and the effect of spaceflight have indicated that bone formation is reduced or ceases altogether at some sites (Holton, et al., 1978; Morey and Baylink, 1978; Turner, et al., 1981; Wronski, et al., 1981). In appendicular long bones (tibia and humerus), periosteal bone formation

and trabecular bone volume were reduced (Holton, et al., 1978; Morey and Baylink, 1978; Turner, et al., 1981). Cessation of periosteal bone formation was predicted to occur in the rat on the eleventh day of flight (Morey and Baylink, 1978). Frost has shown that skeletal mass is related to relative differences in bone formation and resorption (Frost, 1966). Therefore, a significant decrease in bone formation with constant or slight decreased bone resorption would account for loss in bone mass with exposure to spaceflight (Cann, et al., 1980).

In contrast, endosteal bone formation in weight-bearing bones and resorption and bone formation in non-weight bearing bones (mandible) of the rat is not affected by spaceflight (Holton, et al., 1978; Simmons, et al., 1980; Simmons, et al., 1983). The variable effect of spaceflight on bone formation would therefore seem to indicate a localized modification of bone formation. However, the picture is further complicated by studies of bone cells from rats which indicate that differentiation of osteoblasts is suppressed by spaceflight, and this suppression may be due to systemic effects (Roberts and Mozsary, 1981). Therefore, the effect of spaceflight on the skeletal system appears to consist of multiple factors, the dynamics of which require more investigation. The exact histomorphometric parameters of the flight period have yet to be studied at this time.

Recovery to normal formation and resorption levels following spaceflight has been reported to begin in rat long bones three days post-flight and to be completed by 25 days post-flight (Holton, et al., 1978). Eurell and Kazarian found histochemically normal calcium salt levels in rat vertebrae immediately post-flight, but by six days

post-flight, these levels decreased significantly indicating increased bone resorption (Eurell and Kazarian, 1983). By 29 days post-flight, calcium salts had returned to normal levels. A complete histomorphometric study of post-flight recovery bone dynamics in either the rat or higher animals has not been reported.

The effects of spaceflight on the skeleton are thought to be due largely to a lack of gravity, and the resulting condition closely mimics immobilization osteoporosis (Landry and Fleisch, 1964). Hypokinetic studies with rats have revealed a three phase response to immobilization:)1 diminished bone formation, the 2) increased formation and increased destruction, followed by 3) diminished formation. Heaney and Whedon have shown similar phases in paralyzed humans in which formation and resorption decrease in the last phase (Heaney and Whedon, 1958). These phases may apply to the dynamics of bone loss associated with spaceflight but insufficient studies have been performed to verify this.

Histomorphometric parameters related to immobilization in laboratory animals parallel findings in spaceflight studies. Immobilization of very young (8 week old) canines for two months resulted in decreased cortical volume and cortical thickness of long bones (Pavlova, et al., 1975). The author attributed these findings to inhibition of periosteal growth with continued endosteal resorption similar to the findings in rats exposed to spaceflight (Holton, et al, 1978). Another study of four year old rhesus monkeys immobilized for 14 days also indicated inhibition of bone formation in the long bones (Wronski and Morey, 1983). Trabecular bone was more severely affected than cortical bone. The mineral apposition rate in cortical osteons

was diminished and therefore this decrease would suggest that osteoblast function was impaired. The mineral apposition rate for trabecular bone could not be determined due to minimal deposition of tetracycline. This finding further indicated that osteoblasts were severely inhibited in trabecular bone as well. Schock and co-workers reported a study of rhesus monkeys of similar are as Wronski and Morey's (Wronski and Morey, 1983) but immobilized for a longer period of time (2 months) (Schock, et al., 1975). The periosteal apposition rate was significantly reduced in the long bones. The prevalence of osteoid, the amount of tetracycline labelling, and the cortical: total area were also reduced. No change in percentage of surface involved in bone resorption was observed; this finding is in contrast to the previously described canine study (Pavlova, et al., 1975) but the animals were of different ages (juvenile vs. adolescent).

Further, it has been shown that mineralization in osteons of functional mandibles of otherwise immobilized animals is impaired (Simmons, et al., 1984). This study suggests a possible systemic effect of immobilization on mineralization such as stress generated endocrinopathy.

Cann, et al., compared mineral loss between axial and appendicular bones in immobilized adult pigtail monkeys using computed tomography (Cann, et al., 1980). Significantly greater loss was found in axial cancellous bone than in cortical bone of the appendicular long bones. Dual-photon absorptiometry of the lumbar spine of human patients immobilized for treatment of intervertebral disc prolapse showed a mean bone decrease of 0.9%± 0.3% per week (Mazess and Whedon, 1983). The vertebral column is the primary axis of body

support and should be critically examined by histomorphometry to better understand the nature of the bone loss, and how it related to the previously studied appendicular skeleton.

In general, the dynamics of bone loss due to either spaceflight or immobilization are poorly understood. Several of the above studies have been conducted on the rat which has primarily modeling-based skeletal turnover unlike the remodeling turnover in adult humans (Frost, 1973). The sub-human primate and canine studies also used modeling (juvenile and adolescent) animals. None of the studies have documented the histomorphometry for multiple time intervals during spaceflight, hypokinesia, or an extended recovery period.

The objective of this study is to report the histomorphometric parameters of rhesus monkeys exposed to hypokinesia for 14 days. Parameters were collected for the recovery periods of 0, 28, and 56 days post-hypokinesia for ribs, femurs, and vertebrae.

Materials and Methods

A total of twelve rhesus monkeys (Macaca mulatta) were divided into four groups for this study. All animals were placed in a metabolic cage for fourteen days prior to hypokinesia exposure. One group was not exposed to hypokinesia and served as a control group. The other three groups were exposed to hypokinesia for 14 days in a modified primate restraint system (Oloff and Finch, 1978). The three experimental groups were allowed to recover for 0, 28, and 56 days post-hypokinesia and then sacrificed. All groups were labeled with tetracyclines for bone labeling at 5 mg/kg body weight administered intravenously. The labeling schedule used was 2:5:2:3.

Tissue samples were taken from the rib, just below the articulation with the vertebral column; the mid-shaft region of the left femur; and the mid-sagittal section of the L_7 vertebral body. The tissues were fixed in ethanol and shipped to Dr. Eurell.

All samples were dehydrated and embedded in methylmethacrylate. The vertebral bodies were sectioned at 10 micrometers on an LKB Multirange microtome with a tungsten carbide steel knife. The ribs and femurs were cut on a milling machine to 200 micrometers and ground to acceptable thinness. Representative sections of each block were stained with toluidine blue (Parfitt, et al., 1977). Both stained and unstained sections were mounted with Eukitt mounting medium.

All sections were examined with a Leitz microscope for routine histology. The University of Florida Bone Histomorphometry Program[2] was used for all bone histomorphometry.

---

2 This program was kindly loaned by Dr. J.C. Woodard, University of Florida, for use in this study.

The vertebral body parameters were collected in 10 consecutive fields located one field (.26 mm) below the cartilaginous end plate. The rib parameters were collected across the entire surface of the section. The femur parameters were collected across the entire surface except for haversian system parameters which were collected for 10 random fields (a total of 1.6 square mm).

The data were analyzed for mean, standard deviation and analysis of variance using the Epistat Statistical Program for the IBM-PC.

Results

The histomorphometric parameters for the vertebrae, femurs, and ribs are shown in tables 4, 5, and 6. Because of the relatively small sample size of three animals per experimental group, the difference between experimental and control groups was not statistically significant in most cases. Certain trends were present however which should be considered.

Table 4. Means and standard deviations of histomorphometric parameters for vertebrae of rhesus monkeys exposed to hypokinesia for 14 days.

	14-0		14-28		14-56		Control	
Total bone volume (cubic mm)	0.178±	0.075	0.220±	0.035	0.162±	0.035	0.204±	0.040
Total trabecular surface (squ mm)	3.479±	0.251*	3.944±	0.459	3.380±	0.999	4.239±	0.322
Total formation surface (squ mm)	1.031±	0.915	0.916±	0.346	0.818±	0.962	1.655±	0.617
Total resorption surface (squ mm)	0.111±	0.115	0.344±	0.093*	0.200±	0.072	0.082±	0.086
Active resorption surface (squ mm)	0.111±	0.115	0.164±	0.153	0.200±	0.072	0.082±	0.086
Total osteoid volume (cubic mm)	0.011±	0.013	0.008±	0.005	0.007±	0.009	0.014±	0.007
Total bone tissue (cubic mm)	0.638±	0.005	0.664±	0.001	0.652±	0.006	0.675±	0.003
Double label surface (squ mm)	0.378±	0.151	0.337±	0.137	0.489±	0.250	0.416±	0.389
Single label surface (squ mm)	0.529±	0.513	0.544±	0.228	0.342±	0.233	0.313±	0.164
Total trabecular surface on the labeled slide (squ mm)	3.896±	0.862	4.000±	0.086	3.470±	0.662	3.720±	0.406
Osteoid seam width (μm)	7.498±	7.200	9.536±	2.150	7.990±	3.710	11.473±	4.260

Table 4 (cont'd)	14-0		14-28		14-56		Control	
Mean wall thickness (μm)	13.149 ±	7.820	11.216 ±	3.951	12.076 ±	2.262	10.187 ±	3.178
Mean double label width (μm)	15.325 ±	0.737*	11.184 ±	1.775	24.882 ±	4.813	9.880 ±	2.559
Inert surface (squ mm)	2.341 ±	1.117	2.683 ±	0.442	2.361 ±	0.727	2.501 ±	0.888
FIRST ORDER DERIVED PARAMETERS								
Trabecular bone specific volume (mm^3/mm^3)	0.280 ±	0.120	0.331 ±	0.051	0.249 ±	0.053	0.303 ±	0.057
Osteoid specific volume (mm^3/mm^3)	0.017 ±	0.021	0.013 ±	0.008	0.011 ±	0.015	0.022 ±	0.010
Relative osteoid volume (mm^3/mm^3)	0.048 ±	0.051	0.042 ±	0.029	0.038 ±	0.046	0.075 ±	0.040
Trabecular bone specific surface (mm^2/mm^3)	5.455 ±	0.412	5.942 ±	0.684	5.181 ±	1.508	6.262 ±	0.468
Fractional formation surface (mm^2/mm^2)	0.305 ±	0.267	0.231 ±	0.080	0.216 ±	0.205	0.398 ±	0.176
Fractional resorption surface (mm^2/mm^2)	0.031 ±	0.033	0.090 ±	0.036*	0.061 ±	0.019	0.019 ±	0.019
Fractional active resorption surface (mm^2/mm^2)	0.031 ±	0.033	0.041 ±	0.036	0.061 ±	0.019	0.019 ±	0.019

Table 4 (cont'd)	14-0		14-28		14-56		Control	
Fractional inert surface (mm^2/mm^2)	0.664±	0.276	0.680±	0.063	0.722±	0.214	0.583±	0.183
Fractional active double labeled surface (mm^2/mm^2)	0.105±	0.055	0.084±	0.033	0.152±	0.092	0.110±	0.100
Fractional single labeled surface (mm^2/mm^2)	0.158±	0.158	0.135±	0.054	0.108±	0.078	0.085±	0.043
Fractional instantaneously active formation surface (mm^2/mm^2)	0.184±	0.130	0.152±	0.048	0.206±	0.130	0.186±	0.097
Fractional instantaneously active osteoid surface (mm^2/mm^2)	0.368±	0.323	0.741±	0.432	2.700±	3.188	0.443±	0.351
Fractional inactive resorptive surface (mm^2/mm^2)	0		0.048±	0.042	0		0	
Mineral apposition rate (μm/day)	1.734±	0.084	1.265±	0.200	1.684±	0.545	1.118±	0.289
Osteoblast per osteoid perimeter (cells/mm)	37.135±	32.516	65.033±	6.790	60.186±	8.970	45.584±	7.360
Osteoclasts per active resorption perimeter (cells/mm)	15.443±	13.526	23.882±	30.713	33.589±	15.606	29.503±	38.976
Nuclei per osteoclast (nuclei/osteoclast)	2.750±	0.354	2.188±	1.149	2.318±	0.909	2.917±	1.530

Table 4 (cont'd)

	14-0		14-28		14-56		Control	
SECOND ORDER DERIVED PARAMETERS								
Radial closure rate (μm/day)	0.653 ±	0.568	0.895 ±	0.439	4.145 ±	5.257	0.444 ±	0.267
Bone formation period (days)	6.296±	6.733	15.720±	9.745	19.195±	27.853	39.469±	41.427
Mineralization lag time (days)	4.261±	4.163	7.674±	2.277	4.684±	1.024**	10.030±	1.344
Corrected mineralization lag time (days)	7.560±	7.024	11.728±	4.039	15.470±	23.764	41.686±	39.576
Bone formation rate, volume referent (mm^3/mm^3/year)	0.632±	0.453	0.401±	0.052	0.546±	0.317	0.351±	0.198
Bone formation rate, active surface referent (mm^3/mm^2/year)	0.633±	0.031*	0.462±	0.073	0.614±	0.199	0.408±	0.106
Bone formation rate, formation surface referent (mm^3/mm^2/year)	0.238±	0.207	0.327±	0.161	1.513±	1.919	0.162±	0.097
Bone formation rate, total surface referent (mm^3/mm^2/year)	0.118±	0.084	0.068±	0.017	0.111±	0.063	0.055±	0.028
Bone formation rate, osteoblast referent (mm^2/cell/year)	0.008±	0.007	0.007±	0.002	0.011±	0.005	0.009±	0.004

Table 4 (cont'd)	14-0		14-24		14-56		Control	
Trabecular surface/ volume ratio	22.512 ±	11.385	18.066 ±	2.034	20.842 ±	4.537	21.238 ±	4.238
Trabecular volume/ surface ratio	0.052 ±	0.023	0.056 ±	0.006	0.050 ±	0.011	0.048 ±	0.010
Trabecular thickness index	0.104 ±	0.044	0.112 ±	0.012	0.099 ±	0.023	0.097 ±	0.019
Derived osteoid seam width (μm)	6.750 ±	7.530	9.395 ±	3.156	7.335 ±	2.027	8.963 ±	2.221
Bone resorption period (days)	0.240 ±	0.415	5.087 ±	1.390*	3.649 ±	3.385	1.309 ±	1.438
Sigma (days)	6.569 ±	6.755	20.807 ±	10.818	22.844 ±	31.194	40.778 ±	42.679

*Mean is significantly ($p<0.05$) different from the control.
**Mean is highly significantly ($p<0.01$) different from the control.

Table 5. Means and standard deviations of histomorphometric parameters for femurs of rhesus monkeys exposed to hypokinesia for 14 days.

	14-0	14-28	14-56	Control
DIRECT PARAMETERS				
Cortical bone area (mm^2)	32.843± 4.437	38.111± 1.838	39.852± 2.775	38.912± 4.041
Marrow cavity area (mm^2)	19.970± 5.601**	34.894± 3.277	26.128± 4.190**	42.039± 6.282
Haversian envelope				
Mean osteon wall thickness (μm)	46.874± 10.359	63.051± 15.440	61.836± 13.086	66.086± 13.620
Osteoid seam width (μm)	91.424± 51.435	108.009± 80.521	41.776± 11.368	46.800± 37.976
Double label width (μm)	36.850± 26.869	43.208± 21.372	46.803± 38.333	38.472± 19.834
Osteoid lined cavity area (mm^2)	0.022± 0.012	0.048± 0.058	0.066± 0.086	0.012± 0.014
Osteoid lined cavity surface (mm)	0.684± 0.310	1.064± 1.095	2.385± 1.232	0.813± 0.896
Resorption cavity area (mm^2)	0.009± 0.016	0.011± 0.019	0.009± 0.008	0.008± 0.002
Resorption cavity surface (mm^2)	0.203± 0.352	0.237± 0.410	0.318± 0.275	0.339± 0.043

Table 5 (cont'd)	14-0		14-28		14-56		Control	
Inert cavity area (mm^2)	0.015±	0.004	0.016±	0.005	0.014±	0.007	0.012±	0.004
Total osteoid area (mm^2)	0.013±	0.007**	0.040±	0.034**	0.061±	0.034**	2.373±	0.617
Total formation surface (mm^2)	0.684±	0.310	1.064±	1.095	2.385±	1.232	1.016±	0.964
Total resorption surface (mm^2)	0.203±	0.352	0.237±	0.410	0.318±	0.275	0.492±	0.092
DERIVED PARAMETERS								
Cortical bone to total bone area ratio	0.624±	0.083	0.523±	0.015	0.606±	0.031**	0.482±	0.043
Haversian envelope								
Mean osteoid seam circumference (mm)	0.396±	0.061*	0.554±	0.308	0.427±	0.130	0.254±	0.040
Fractional formation surface (mm^2/mm^2)	0.179±	0.092	0.227±	0.188	0.495±	0.195	0.234±	0.212
Fractional active formation surface (mm^2/mm^2)	0.136±	0.089	0.046±	0.037	0.024±	0.178	0.160±	0.125
Fractional single labeled formation surface (mm^2/mm^2)	0.066±	0.011	0.065±	0.056	0.053±	0.044	0.016±	0.027
Fractional instantaneously active formation surface (mm^2/mm^2)	0.139±	0.088	0.078±	0.057	0.260±	0.198	0.168±	0.138

Table 5 (cont'd)	14-0		14-28		14-56		Control	
Fractional osteoid surface labeled (mm^2/mm^2)	0.735±	0.114	0.383±	0.073**	0.486±	0.186	0.740±	0.110
Mean resorptive cavity circumference (mm)	0.203±	0.352	0.237±	0.410	0.318±	0.275	0.371±	0.017
Fractional resorption surface (mm^2/mm^2)	0.042±	0.072	0.065±	0.113	0.063±	0.055	0.120±	0.005
Fractional inert surface (mm^2/mm^2)	0.779±	0.115	0.708±	0.204	0.441±	0.213	0.599±	0.222
Fractional number of osteons labeled	1.000±	0	0.944±	0.096	0.911±	0.084	0.941±	0.102
Mineral apposition rate (m/day)	5.265±	3.839	6.173±	3.054	6.686±	5.476	5.496±	2.834
Radial closure rate (mm/year)	3.970±	4.946	2.082±	0.953	2.324±	2.097	1.831±	0.807
Mineralization lag time (days)	20.231±	14.289	15.040±	8.372	9.852±	7.126	7.636±	2.819
Corrected mineralization lag time (days)	20.231±	14.289	15.975±	9.380	11.171±	8.126	8.409±	4.142
Bone formation period (days)	12.809±	8.744	13.216±	7.308	16.405±	11.188	16.580±	12.058
Bone formation rate, surface referent ($mm^3/mm^2/year$)	0.267±	0.204	0.189±	0.206	0.126±	0.106	0.428±	0.463

Table 5 (cont'd)	14-0		14-28		14-56		Control	
Sigma (days)	12.809±	8.744	13.216±	7.308	16.405±	11.188	16.580±	12.058
Cortical porosity (%)	0.029±	0.015	0.046±	0.033	0.055±	0.018*	0.020±	0.006

*Mean is significantly ($p<0.05$) different from the control.
**Mean is highly significantly ($p<0.01$) different from the control.

Table 6. Means and standard deviations of histomorphometric parameters for ribs of rhesus monkeys exposed to hypokinesia for 14 days.

	14-0		14-28		14-56		Control	
DIRECT PARAMETERS								
Cortical bone area (mm^2)	4.284±	0.418	3.696±	0.467	3.591±	0.501	3.283±	0.470
Marrow cavity area (mm^2)	1.079±	0.236	0.829±	0.134	0.850±	0.603	1.094±	0.175
PRIMARY PARAMETERS								
Periosteal envelope								
Total periosteal surface (mm^2)	9.584±	0.545*	8.344±	0.488	8.076±	0.342	8.017±	0.415
Total formation surface (mm^2)	4.182±	3.330	6.286±	2.888	5.596±	1.950	6.411±	1.728
Total resorptive surface (mm^2)	0		0		0		0	
Inert surface (mm^2)	5.402±	3.565	2.058±	3.201	2.480±	2.286	1.607±	1.332
Periostal mean double label width (μm)	3.853±	6.674	14.927±	6.080	19.794±	6.927	15.301±	8.565
Periosteal double label surface (mm^2)	1.455±	2.520	2.225±	2.002	3.132±	0.905	1.482±	1.287
Periosteal single label surface (mm^2)	2.741±	1.828	3.535±	1.215	1.676±	2.590	3.890±	1.912

Table 6 (cont'd)	14-0		14-28		14-56		Control	
Periosteal osteoid seam width (μm)	4.348±	7.530*	9.326±	8.384	19.750±	9.313	70.388±	40.363
Endosteal envelope								
Total endosteal surface (mm^2)	5.671±	0.336	4.322±	0.356	5.323±	3.556	5.597±	0.996
Total formation surface (mm^2)	2.220±	1.203	2.244±	0.098	1.826±	1.406	3.387±	1.469
Total resorptive surface (mm^2)	0.238±	0.412	0.146±	0.130	0		0.201±	0.348
Inert surface (mm^2)	3.214±	1.043	1.932±	0.337	3.504±	2.294	2.009±	1.330
Endosteal mean double label width (μm)	13.511±	5.349	17.407±	5.419	18.450±	4.087	13.758±	2.862
Endosteal double label surface (mm^2)	1.017±	1.046	1.215±	0.267	1.016±	1.020	1.983±	1.215
Endosteal single label surface (mm^2)	0.516±	0.377*	0.361±	0.295**	0.317±	0.275**	1.249±	0.114
Endosteal osteoid seam width (μm)	15.811±	3.313	15.910±	1.915	13.023±	0.549	22.618±	9.453
Haversian envelope								
Mean osteon wall thickness (μm)	52.318±	20.752	49.085±	16.791	49.806±	19.466	47.550±	14.897
Osteoid seam width (μm)	103.386±	107.975	21.813±	12.458	64.329±	9.274	166.913±	138.624

Table 6 (cont'd)	14-0		14-28		14-56		Control	
Double label width (μm)	117.181±	167.139	16.425±	2.818	38.094±	29.039	160.119±	198.771
Osteoid lined cavity area (mm^3)	0.392±	0.522	0.181±	0.077	0.268±	0.076	0.168±	0.058
Osteoid lined cavity surface (mm^2)	6.120±	5.722	4.072±	0.084	6.545±	0.352**	3.379±	0.875
Osteoid seam number (seams)	9.667±	5.508	7.667±	2.517	15.667±	2.528*	7.667±	3.512
Resorption cavity area (mm^2)	0.053±	0.090	0.007±	0.008	0.019±	0.023	0.007±	0.006
Resorption cavity surface (mm^2)	0.746±	1.109	0.249±	0.228	0.696±	0.884	0.242±	0.210
Resorption cavity number (resorption cavities)	1.000±	1.000	0.667±	0.577	2.000±	2.646	0.667±	0.577
Waltzing osteon number (waltzing osteons)	0		0		0		0	
Total cavity area (mm^2)	0.454±	0.476	0.196±	0.077	0.290±	0.054	0.183±	0.048
Total cavity surface (mm^2)	8.583±	5.522	5.675±	0.880	8.081±	1.746*	5.038±	0.176
Total osteoid area (mm^2)	0.355±	0.509	0.152±	0.076	0.219±	0.071	0.136±	0.042

Table 6 (cont'd)	14-0		14-28		14-56		Control	
Total formation surface (mm^2)	6.120±	5.722	4.072±	0.804	6.545±	0.352**	3.379±	0.876
Total resorption surface (mm^2)	0.746±	1.109	0.249±	0.228	0.696±	0.884	0.242±	0.210
Double labeled surface (mm^2)	2.260±	1.941	1.073±	0.408	2.218±	0.445	1.856±	0.800
Double label number (double labels)	7.667±	4.933	5.667±	2.517	11.667±	2.082*	6.000±	2.000
Single labeled surface (mm^2)	0.468±	0.484	0.367±	0.327	0.428±	0.300	0.323±	0.204
Single label number (single labels)	1.667±	2.082	1.667±	0.577	2.333±	1.155	1.667±	1.528
DERIVED PARAMETERS								
Cortical bone to total bone area ratio	0.798±	0.049	0.816±	0.031	0.812±	0.124	0.749±	0.032
Cortical porosity (%)	9.978±	9.601	5.557±	2.998	8.311±	2.649	5.130±	1.117
Periosteal envelope								
Fractional formation surface (mm^2/mm^2)	0.442±	0.359	0.763±	0.367	0.700±	0.264	0.794±	0.178
Fractional active formation surface (mm^2/mm^2)	0.155±	0.268	0.275±	0.253	0.389±	0.117	0.186±	0.161

Table 6 (cont'd)	14-0		14-28		14-56		Control	
Fractional instantaneously active formation surface (mm^2/mm^2)	0.300±	0.363	0.486±	0.276	0.495±	0.108	0.426±	0.205
Fractional single labeled formation surface (mm^2/mm^2)	0.290±	0.198	0.422±	0.135	0.212±	0.329	0.478±	0.216
Fractional osteoid surface labeled (mm^2/mm^2)	0.530±	0.282	0.606±	0.096	0.747±	0.166	0.539±	0.224
Fractional resorptive surface (mm^2/mm^2)	0		0		0		0	
Fractional inert surface (mm^2/mm^2)	0.558±	0.359	0.237±	0.367	0.300±	0.264	0.206±	0.178
Mineral apposition rate (μm/day)	0.550±	0.953	2.133±	0.869	2.828±	0.990	2.186±	1.224
Corrected mineral apposition rate (μm/day)	0.463±	0.802	1.343±	0.670	2.204±	1.219	1.323±	1.053
Mineralization lag time (days)	2.633±	4.560	3.677±	3.188	6.974±	1.652	39.347±	24.819
Corrected mineralization lag time (days)	3.131±	5.424	5.567±	4.838	9.435±	2.167	89.573±	68.498
Bone formation rate (mm^3/mm^2/year)	0.256±	0.443	0.729±	0.756	1.128±	0.531	0.506±	0.498

Table 6 (cont'd)	14-0		14-28		14-56		Control	
Endosteal envelope								
Fractional formation rate (mm^2/mm^2)	0.398 ±	0.221	0.520 ±	0.023	0.329 ±	0.150	0.616 ±	0.252
Fractional active formation surface (mm^2/mm^2)	0.183 ±	0.184	0.279 ±	0.041	0.163 ±	0.071	0.359 ±	0.199
Fractional instantaneously active formation surface (mm^2/mm^2)	0.229 ±	0.216	0.320 ±	0.072	0.191 ±	0.069	0.474 ±	0.214
Fractional osteoid surface labeled (mm^2/mm^2)	0.085 ±	0.074	0.081 ±	0.062*	0.057 ±	0.024**	0.230 ±	0.061
Fractional resorption surface (mm^2/mm^2)	0.040 ±	0.069	0.035 ±	0.032	0		0.033 ±	0.057
Fractional inert surface (mm^2/mm^2)	0.562 ±	0.155	0.445 ±	0.046	0.671 ±	0.150	0.352 ±	0.197
Mineral apposition rate (μm/day)	1.930 ±	0.764	2.487 ±	0.774	2.636 ±	0.584	1.965 ±	0.409
Corrected mineral apposition rate (μm/day)	0.722 ±	0.330	1.471 ±	0.215	1.733 ±	0.836	1.500 ±	0.381
Mineralization lag time (days)	8.676 ±	2.211	6.640 ±	1.208	5.144 ±	1.391*	11.123 ±	2.790
Corrected mineralization lag time (days)	28.202 ±	21.737	10.891 ±	1.160	9.550 ±	6.415	14.572 ±	2.981

Table 6 (cont'd)	14-0		14-28		14-56		Control	
Bone formation rate ($mm^3/mm^2/year$)	0.262±	0.240	0.678±	0.138	0.441±	0.267	0.751±	0.476
Haversian envelope								
Relative osteoid volume (mm^3/mm^3)	0.076±	0.103	0.043±	0.028	0.063±	0.029	0.029±	0.017
Osteoid seam number (seams/sq mm)	2.272±	1.384	2.104±	0.725	4.394±	0.469*	2.346±	1.004
Labeled osteoid seam number ($seams/mm^2$)	1.983±	1.315	1.788±	0.781	3.621±	0.798	2.211±	0.900
Resorptive cavity number per unit area ($cavities/mm^2$)	0.234±	0.247	0.189±	0.167	0.499±	0.635	0.219±	0.192
Mean osteoid seam circumference (mm)	0.597±	0.545	0.557±	0.133	0.419±	0.028	0.475±	0.115
Fractional formation surface (mm^2/mm^2)	0.618±	0.372	0.715±	0.053	0.835±	0.175	0.672±	0.181
Fractional active formation surface (mm^2/mm^2)	0.237±	0.127	0.187±	0.060	0.281±	0.062	0.409±	0.182
Fractional single labeled formation surface (mm^2/mm^2)	0.068±	0.082	0.060±	0.045	0.057±	0.041	0.071±	0.043
Fractional instantaneously active formation surface (mm^2/mm^2)	0.271±	0.155	0.217±	0.070	0.309±	0.082	0.444±	0.203

Table 6 (cont'd)	14-0		14-28		14-56		Control	
Fractional osteoid surface labeled (mm^2/mm^2)	0.456±	0.094	0.299±	0.080*	0.370±	0.060	0.576±	0.132
Mean resorptive cavity circumference (mm)	0.409±	0.531	0.249±	0.228	0.245±	0.214	0.242±	0.210
Fractional resorption surface (mm^2/mm^2)	0.151±	0.249	0.043±	0.042	0.074±	0.088	0.048±	0.042
Fractional inert surface (mm^2/mm^2)	0.232±	0.123	0.242±	0.094	0.091±	0.088	0.295±	0.146
Fractional number of osteons labeled	0.831±	0.190	0.825±	0.109	0.817±	0.097	0.913±	0.076
Mineral apposition rate (μm/day)	16.740±	23.877	2.346±	0.402	5.442±	4.148	22.874±	28.396
Radial closure rate (mm/year)	4.034±	5.260	0.713±	0.194	1.625±	1.252	8.196±	10.483
Mineralization lag time (days)	24.232±	36.342	8.902±	3.444	15.680±	8.050	22.844±	18.929
Corrected mineralization lag time (days)	27.963±	41.902	10.714±	3.339	19.168±	9.267	24.644±	20.722
Bone formation period (days)	15.209±	12.601	27.912±	15.546	17.703±	12.922	6.404±	7.048
Bone formation rate, volume referent ($mm^3/mm^3/year$)	1.179±	0.613	0.302±	0.149	1.338±	0.995	3.356±	2.845

Table 6 (cont'd)	14-0		14-28		14-56		Control	
Bone formation rate, surface referent ($mm^3/mm^2/year$)	0.816±	0.744	0.189±	0.081	0.625±	0.510	2.266±	1.833
Surface/volume ratio	1.938±	1.050	1.575±	0.467	2.234±	0.176**	1.458±	0.070
Activation frequency, osteoid seam based ($foci/year/mm^2$)	0.958±	1.050	0.296±	0.243	1.581±	1.888	1.930±	1.282
Sigma (days)	15.209±	12.601	27.912±	15.546	17.703±	12.922	6.404±	7.047

*Mean is significantly ($p<0.05$) different from the control.
**Mean is highly significantly ($p<0.01$) different from the control.

Discussion

Results indicate that bone formation in the rhesus monkey vertebrae was inhibited as a result of hypokinesia, but bone resorption was not. This inhibition resulted in decreased trabecular bone specific volume, decreased formation surface and increased resorption surface (0 day post-hypokinesia animals). Mineral apposition rate was increased, resulting in a high bone formation rate in spite of reduced numbers of osteoblasts.

Trabecular bone specific volume was increased at 28 days. Fractional resorption surface was also significantly elevated indicating that the bone was in a resorption phase. Bone formation was slightly decreased but still above normal. The number of osteoblasts per osteoid perimeter had increased indicating more osteoblast activity which was further supported by a wider osteoid seam width.

At 56 days post-hypokinesia, trabecular bone specific volume and fractional formation surface had further declined. Fractional resorption surface had decreased, but was still above normal. Mineral apposition rate was still elevated. At this point, bone mineralization was proceeding faster than normal. Although the number of osteoblasts had increased as had bone formation per cell, the total bone formation had not yet balanced the bone resorption. The resorption rate between the 28 day post-hypokinesia group and the 58 day post-hypokinesia group is approximately 1.705 $mm^3/mm^2/day$ compared to a bone formation rate of 1.513 $mm^3/mm^2/day$, therefore the bone had not yet recovered from the hypokinesia.

The 0 day post-hypokinesia femurs had increased mineralization lag time and osteoid seam widths, but a relatively normal mineral apposition rate. The fractional formation surface, fractional resorption surface, and bone formation rate were decreased. These parameters seemed to indicate that formation and resorption were inhibited. Mineralization may have been temporarily inhibited, creating an increased osteoid seam width. Then mineralization resumed, resulting in a normal apposition rate at sampling time.

Fractional formation surface increased to near control level and fractional resorption surface increased slightly at 28 days post-hypokinesia. Mineralization lag time decreased but was still elevated above control levels.

At 56 days post-hypokinesia, fractional formation surface was greatly increased. Cortical porosity was also increased significantly as a result of the increased number of bone modeling sites. Mineral apposition rate and mineralization lag time were near control levels.

The femoral parameters indicate an inhibition of bone formation and resorption and an episode of mineralization interruption which occurred during hypokinesia. During the recovery period, the femur had increased bone formation at the osteonal level, but resorption appeared to remain depressed. The pattern may be the result of young growing animals recovering from the earlier inhibition of formation and resorption during hypokinesia.

Cortical porosity of the femur was increased in the 0 and 28 day post-hypokinesia monkeys.

The periosteal fractional formation surface was decreased in the 0 day post-hypokinesia group. Mineral apposition rate was decreased,

as was mineralization lag time and osteoid seam width, suggesting an inhibition in osteoid formation resulting in the decreased periosteal bone formation rate.

The periosteal bone formation rate and associated parameters (osteoid seam width and formation surface) increased with time until at 56 days, the formation rate exceeded the control rate. This increase in bone formation may reflect the response of the modeling animal to recovery from hypokinesia.

Endosteal formation surface was reduced in the 0 day post-hypokinesia group. Mineral apposition rate was increased and mineralization lag time decreased in the 58 day post-hypokinesia group resulting in the decreased formation surface observed in that group. In general, endosteal bone formation rate remained below the control group for all three experimental groups. This effect may be a combination of modeling and hypokinesia effect.

Decreased periosteal bone formation parallels findings in the tibia and humerus of other species following spaceflight (Holton, et al., 1978), however endosteal resorption observed in these animals was not observed.

The osteonal surface of the rib has increased fractional resorption surface at 0 days post-hypokinesia. The bone formation rate and fractional formation surface are decreased. This indicates an initial resorption phase following hypokinesia.

At 28 days post-hypokinesia, the fractional formation surface is increased, but mineral apposition rate and bone formation rate are still decreased.

At 56 days post-hypokinesia, fractional formation surface is further increased, bone formation rate is increased over the 28 day level and mineral apposition rate is slightly increased indicating that the bone formation phase is beginning.

In summary, because of the low number of animals per group, most histomorphometric parameters were not statistically significant. Trends seem to indicate that the hypokinesia treatment inhibited bone formation in all three bones examined. Bone resorption was also inhibited in the femur. All three bones responded by increasing bone formation by 56 days post-hypokinesia, but the vertebrae seemed to be less responsive than the long bones. This lack of response may be due to a fairly long sigma of 40.8 days in the vertebrae compared to the rib sigma of 6.4 days and femoral sigma of 16.6 days. Wronski and Morey (1983) also demonstrated that trabecular bone was more severely affected by immobilization than cortical bone.

All three bones had decreased fractional formation surface immediately after hypokinesia. Fewer osteoblasts per formation surface were also noted when cells were counted (vertebral sections only). This may indicate supression of osteoblast differentiation as reported by Roberts and Mozsary (1981).

The results of this study are complicated by the effects of normal bone growth in a skeletally immature animal. Also one animal in the 0 days post-hypokinesia group was ill (088), and values from this animal further skewed sample results. In addition, the ribs are not truly immobilized in this study as the animal continues to breathe. This raises a question of effect on the bone due to stress generated endocrinopathy.

SCANNING ELECTRON MICROSCOPY OF FRACTURE SURFACES OF LONG BONES

Introduction and Literature Review

Fractures of long bones occur frequently in association with military aircraft ejection (Every, 1977). Scanning electron microscopy of *in vivo* fractures has not been reported in the literature to date. It is probable that SEM of fractures would contribute to an understanding of fracture propagation and healing (Boyde, 1972). Characterization of this type might also help in determining the etiology of fractures.

The purpose of this study was to observe two of the basic patterns of long bone fractures with SEM and develop techniques for further evaluation of fractures.

Materials and Methods

Two canine femurs were utilized in this portion of the study. One femur had been fractured in a torsional pattern *in vivo*. Both right and left femurs were collected and excess tissue was removed. The bones were air dried. The opposite femur was fractured post mortem in a straight pattern by clamping the femur in a vise and manually applying force in an anterior-posterior direction. Fragments of each bone were coated with gold palladium and examined using SEM as previously described.

Results

Montages of the fracture edges of the torsional and straight fractures are shown in figure 133. Osteocytic lacunae were present in higher magnification of the straight fracture surface (figs. 134 and 135). The surface in general was uneven and rough. Grooves representative of canaliculi crossed the surface at scattered intervals. At higher magnification, the surface of the torsional fracture was also roughened, but protruding edges of the mineralized tissue fragments were more rounded and shorter than the surface fragments of the straight fractures (figs. 136 and 137). Canaliculi were not as obvious on the torsional fracture surface. Unlike on the straight fracture surface, numerous cracks running perpendicular to the long axis of the bone were observed in the surface of the torsional fracture.

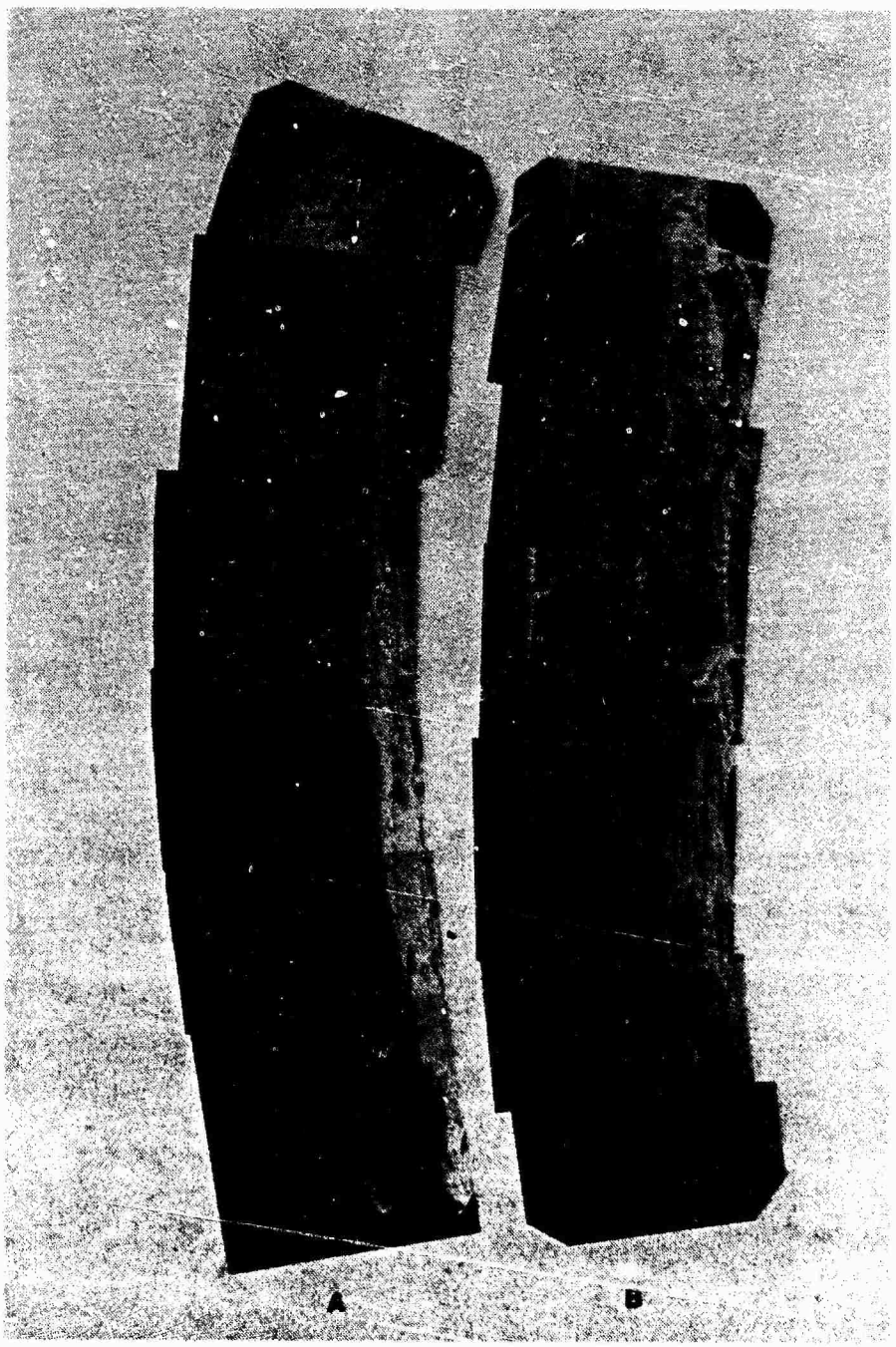

Figure 133. Montages of straight (A) and torsional (B) fracture surfaces. 4X.

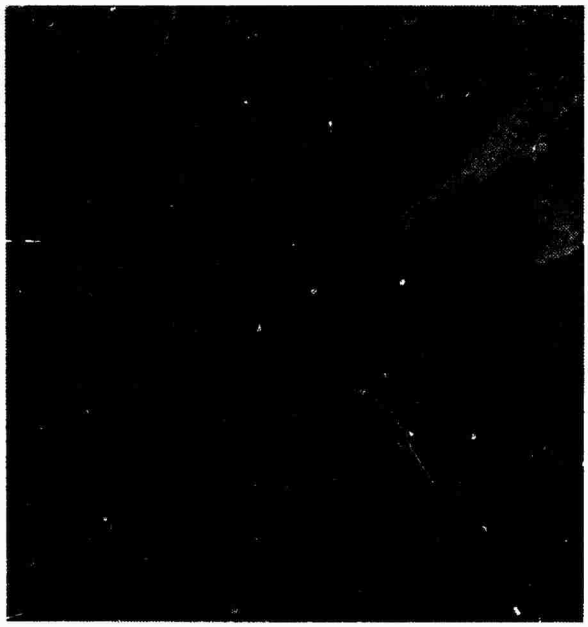

Figure 134. Osteocytic lacuna on the surface of a straight fracture. 2000X. C=canaliculus.

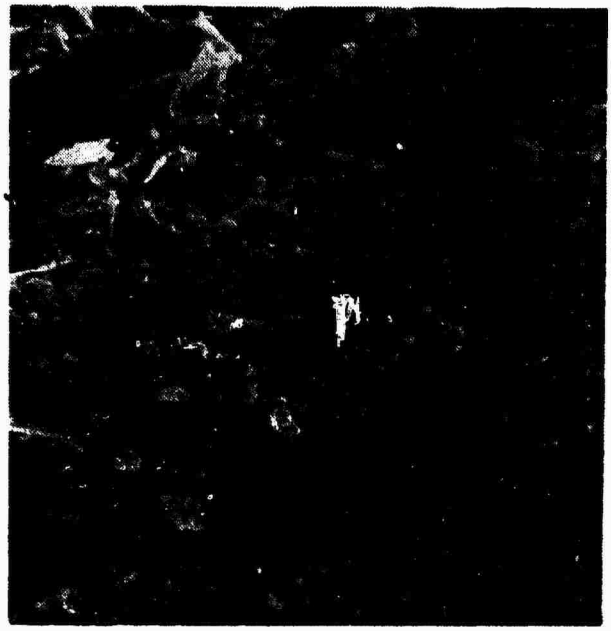

Figure 135. Osteocytic lacunae and prominent grooves representative of canaliculi present on straight fracture surface. 2000X. C=canaliculus.

Figure 136. Surface of torsional fracture with more rounded mineralized tissue fragments and less prominent canaliculi than the straight fracture. 2000X.

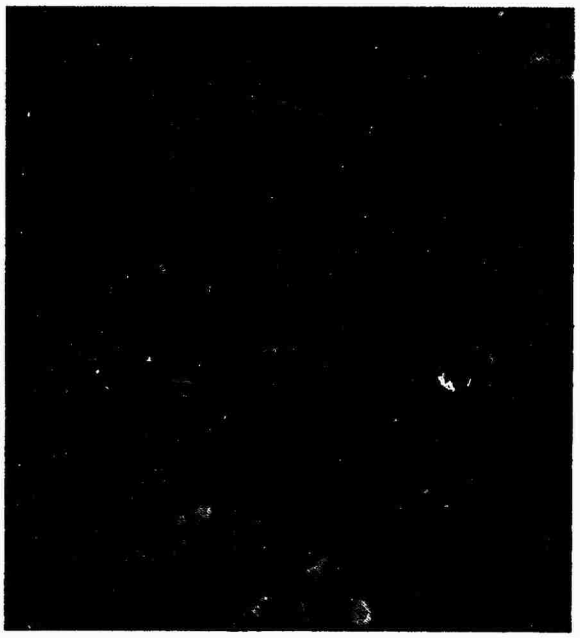

Figure 137. Cracks in the surface of the torsional fracture. 2000X.

Discussion

Variation of the surface texture of the torsional and straight fractures was probably due to the different angles of the two fracture planes across collagen fibers and mineralized matrix. The different angles of the planes may also account for the prominent canaliculi on the surface of the straight fracture. The cracks in the surface of the torsional fracture may be a result of the different type of forces necessary to produce a torsional fracture compared to a straight fracture. In order to adequately characterize these fracture patterns, it must be considered that one fracture was created *in vivo* while the other fracture was created *in vitro*. Further evaluation of the several fractures of each type (straight, torsional, etc.) occurring both *in vivo* and *in vitro* must be conducted to ensure adequate characterization.

REFERENCES

Adams, R., D.R. Eyre, and H. Muir (1977) Biochemical aspects of development and ageing of human lumbar intervertebral discs. Rheum. Rehab. 16: 22-29.

Anderson, C., and K.D. Danylchuk (1977) Scanning electron microscopic observations on bone. Arch. Pathol. Lab. Med. 101: 19-21.

Antonopoulos, C.A., S. Gardell, J.A. Szirmai, and E.R. DeTyssonsk (1964) Determination of glycosaminoglycans (mucopolysaccharides) from tissues on the microgram scale. Biochimica et Biophysica Acta 83: 1.

Beadle, O.A. (1931) The intervertebral discs. Observations of their normal and morbid anatomy in relation to certain spinal deformities. London: His Majesty's Stationery Office.

Bernick, S., and R. Cailliet (1982) Vertebral end-plate changes with aging of human vertebrae. Spine 7(2): 97-102.

Bernick, S., R. Cailliet, and B. Levy (1980) Maturation and aging of the vertebrae of marmosets. Spine 5(6): 519-524.

Berry, C.A. (1969) Preliminary clinical report of the medical aspects of Apollos VII and VIII. Aerosp. Med. 40: 245-254.

Bick, E.M., and J.W. Copel (1950) Longitudinal growth of the human vertebra. A contribution to human osteogeny. J. Bone Jt. Surg. 32A: 803-814.

Boyde, A. (1972) Scanning electron microscope studies of bone. In Bourne, G.H. (ed): The Biochemistry and Physiology of Bone. New York: Academic Press, pp. 259-310.

Brown, R., R.J. Hansen, and A.J. Yorra (1957) Some mechanical tests on the lumbosacral spine with particular reference to the intervertebral discs. J. Bone Jt. Surg. 39A: 1135-1164.

Butler, W.F., and R.N. Smith (1967) Age changes in the nucleus pulposus of the non-ruptured intervertebral disc of the cat. Res. Vet. Sci. 8: 151-156.

Butler, W.F., and C.M. Wels (1971) Glycosaminglycans of cat intervertebral disc. Biochem. J. 122: 647-652.

Calve, J., and M. Galland (1930) The intervertebral nucleus pulposus. Its anatomy, its physiology, its pathology. J. Bone Jt. Surg. 12: 555-578.

Cann, C.E., R.R. Adachi, and E.M. Holton (1980) Bone resorption and calcium absorption in rats during spaceflight. Physiologist 23: 585-586.

Cann, C.E., H.K. Genant, and D.R. Young (1980) Comparison of vertebral and peripheral mineral losses in disuse osteoporosis i.. monkeys. Radiology 134: 525-529.

Coventry, M.B. (1969) Anatomy of the intervertebral disk. Clin. Orthop. 67: 9-15.

Coventry, M.B., R.K. Ghormley, and J.W. Kernohan (1945a) The intervertebral disc: its microscopic anatomy and pathology. Part I. Anatomy, development, and physiology. J. Bone Jt. Surg. 27: 105-112.

Coventry, M.B., R.K. Ghormley, and J.W. Kernohan (1945b) The intervertebral disc: its microscopic anatomy and pathology. Part II. Changes in the intervertebral disc concomitant with age. J. Bone Jt. Surg. 27: 233-247.

Davidson, E.A., and W. Small (1963) Metabolism in vivo of connective tissue mucopolysaccharides. 1. Chondroitin sulfate C and keratosulfate of nucleus pulposus. Biochim. et Biophys. Acta 69: 445-458.

De Palma, A.F., and R.H. Rothman (1970) The Intervertebral Disc. Philadelphia: W. B. Saunders, pp. 4-14.

Dietlein, L.F., P.C. Rambaut, and A.E. Nicogossian (1983) Future thrusts in life sciences experimentation in space. Aviat. Space Environ. Med. 54: 56-58.

Donisch, E., and W. Trapp (1971) The cartilage endplates of the human vertebral column (some considerations of postnatal development). Anat. Rec. 169: 705-716.

Eurell, J.A., and L.E. Kazarian (1982) The scanning electron microscopy of compressed vertebral bodies. Spine 7(2): 123-128.

Eurell, J.A., and L.E. Kazarian (1983) Quantitative histochemistry of rat lumbar vertebrae following spaceflight. Physiologist 244: R315-318.

Eyring, E.J. (1969) The biochemistry and physiology of intervertebral disk. Clin. Orthop. Rel. Res. 67: 16-18.

Fick, R. (1904) Handbuch der Anatomie und Mechanik der Gelenke. Jena: Verlag G. Fischer.

Frankel, V.H., and M. Nordin (1980) Basic Biomechanics of the Skeletal System. Philadelphia: Lea and Febiger, pp. 22-27.

Frost, H.L. (1973) The spinal osteoporoses. Mechanisms of pathogenesis and pathophysiology. Clin. Endocrinol. Metab. 2: 257-275.

Frost, H.M. (1966) Bone dynamics in metabolic bone disease. J. Bone Jt. Surg. 48A: 1192-1203.

Frost, H.M. (1973) Bone Remodeling and Its Relationship to Metabolic Bone Diseases. Springfield, IL: CC Thomas.

Guntz, E. (1934) Die erkrankungen der zwischenwirbelgelenke. Arch. Orthop. Unfall-Chir. 34: 333.

Hallen, A. (1958) Heoxamine and ester sulphate content of the human nucleus pulposus at different ages. Acta Chemica Scandinavica 12: 1869.

Ham, A.W., and D.H. Cormack (1979) Histology. Philadelphia: J.B. Lippincott, p. 448.

Hansson, T., and B. Roos (1981a) The relation between bone mineral content, experimental compression fractures, and disc degeneration in lumbar vertebrae. Spine 6: 147-153.

Hansson, T., and B. Roos (1981b) Microcalluses of the trabeculae in lumbar vertebrae and their relation to the bone mineral content. Spine 6: 375-380.

Harris, I.R., and I. Macnab (1954) Structural changes in the lumbar intervertebral discs. J. Bone Jt. Surg. 36B: 304-322.

Hattner, R.S., and D.F. McMillan (1968) Influence of weightlessness upon the skeleton: a review. Aerosp. Med. 39: 849-855.

Heaney, R.P., and G.D. Whedon (1958) Radiocalcium studies of bone formation rate in human metabolic bone disease. J. Clin. Endocrinol. 18(1): 1246-1267.

Higuchi, M., K. Kaneda, and K. Abe (1982) Postnatal histiogenesis of the cartilage plate of the spinal column. Spine 7(2): 89-96.

Hirsch, C., and A. Nachemson (1961) Clinical observations on the spine in ejected pilots. Acta Orthop. Scand. 31: 135.

Hirsch, C., and F. Schajowicz (1953) Studies on structural changes in the lumbar annulus fibrosus. Acta Orthop. Scand. 22: 184-231.

Holman, W., and G.L. Duff (1939) Pathology of the intervertebral disc. Prog. Med. Sci. 198(3): 419-437.

Holton, E.M., R.T. Turner, and D.H. Baylink (1978) Quantitative analysis of selected bone parameters. In Rosenweig, S.N., and K.A. Sousa (eds): Final Reports of U.S. Experiments Flown on the Soviet Satellite COSMOS, NASA Technical Memorandum 78526.

Kazarian, L., and G.A. Graves (1977) Compressive strength characteristics of the human vertebral centrum. Spine 2: 1-14.

Kazarian, L.E. (1978) Identification and classification of vertebral fractures following emergency capsule egress from military aircraft. Aviat. Space Environ. Med. 49: 166-169.

Kazarian, L.E. (1979) Personal communication.

Kelley, R.O., and R.A.F. Dekker, and J.G. Bluemink (1975) Thiocarbohydrazide-mediated osmium binding: a technique for protecting soft biological specimens in the scanning electron microscope. In Hayat, M.A. (ed): Principles and Techniques of Scanning Electron Microscopy. New York: Van Nostrand Reinhold, pp. 34-45.

Keyes, D.C., and E.L. Compere (1932) The normal and pathological physiology of the nucleus pulposus of the intervertebral disc. J. Bone Jt. Surg. 14: 897-938.

Landry, M., and H. Fleisch (1964) The influence of immobilization on bone formation as evaluated by osseous incorporation of tetracyclines. J. Bone Jt. Surg. 46B: 764-771.

Laurell, L., and A. Nachemson (1963) Some factors influencing spinal injuries in seat ejected pilots. Aerospace Medicine 34: 726-729.

Lewin, T. (1964) Osteoarthritis in lumbar synovial joints: a morphologic study. Acta Orthop. Scand. S73: 3-112.

Lewin, T., R. Moffett, and A. Viidik (1961) The morphology of the lumbar synovial intervertebral joints. Acta Morph. Neerl-Scand. 4: 299-319.

Mack, P.B. (1971) Bone density changes in a Macaca nemestrina monkey during the biosatellite III project. Aerosp. Med. 42: 828-833.

Mazess, R.D., and G.D. Whedon (1983) Immobilization and bone. Calcif. Tis. Int. 35: 265-267.

Morey, E.R., and D.J. Baylink (1978) Inhibition of bone formation during spaceflight. Science 201: 1138-1141.

Nussbaum, N. (1977) Pathology of trauma to vertebral segments subjected to mechanical stress. Request no. 86-88-24, Air Force Office of Scientific Research.

Nussbaum, N.S. (1981) Cartilage of the intervertebral disc end-plate. A histological, histochemical, and fine structure study. AFAMRL-TR-81-122.

Olin, H.A. (1937) Injuries to the intervertebral disc. Indust. Med. 6: 401-406.

Oloff, C.M., and W.L. Finch (1978) A subhuman primate restraint system. AMRL-TR-78-88.

Pace, N. (1977) Weightlessness: a matter of gravity. New Eng. J. Med. 297(1): 32-38.

Parfitt, A.M., A.R. Villanueva, M.M. Crouch, C.H. Mathews, and H. Duncan (1977) Classification of osteoid seams by combined use of cell morphology and tetracycline labeling. In Meunier, P.R. (ed): Proceedings of Second Workshop on Bone Morphometry. Paris: Armour Montagu.

Parke, W.W. (1975) Development of the spine. In Rothman, R.H., and F.A. Simeone (eds): The Spine. Philadelphia: W.B. Saunders, pp. 1-17.

Pavlova, M.N., A.I. Volozhin, and I. Muradov (1975) Effect of hypokinesia on structures and mineral content of the long bones of puppies. Bull. Exp. Biol. Med. 80: 260-274.

Peacock, A. (1951) Observations on the pre-natal development of the intervertebral disc in man. J. Anat. 85: 250-274.

Perey, O. (1957) Fracture of the vertebral end-plate in the lumbar spine. An experimental biomechanical investigation. Acta Orthop. Scand. Suppl. 26: 1-101.

Roaf, R. (1960) A study of the mechanics of spinal injuries. J. Bone Jt. Surg. 42B: 810-823.

Roberts, W., and P.G. Mozsary (1981) Supression of osteoblast differentiation during weightlessness. Physiologist 24(6): 575-576.

Scherft, J.P. (1972) The lamina limitans of the organic matrix of calcified cartilage and bone. J. Ultrastruct. Res. 38: 318-331.

Schmorl, G., and H. Junghanns (1959) The Human Spine in Health Disease. New York: Grune and Stratton, p. 13.

Schock, C.C., F.R. Noyes, M.M. Crouch, and C.H. Mathews (1975) The effects of immobility on long bone remodeling in the rhesus monkey. Henry Ford Hosp. Med. J. 23: 107-115.

Schultz, A.H. (1930) The skeleton of the trunk and limbs of higher primates. Human Biol. 2: 303.

Sherrington, C.S. (1892) Notes on the arrangement of some motor fibers in the lumbosacral plexus. J. Physiol. 13: 621.

Simmons, D.J., J.E. Russell, W.V. Walker, B. Grazman, C. Oloff, and L. Kazarian (1984) Growth and maturation of mandibular bone in otherwise totally immobilized rhesus monkeys. Clin. Orthop. Rel. Res. 182: 220-230.

Simmons, D.J., J.E. Russell, F. Winter, R. Baron, A. Vignery, T.V. Thuc, G.D. Rosenberg, and W. Walker (1980) Bone growth in the rat mandible during spaceflight. Physiologist 23: 587-590.

Souter, W.A., and T.K. Taylor (1970) Sulphated acid mucopolysaccharide metabolism in the rabbit intervertebral disc. J. Bone Jt. Surg. 52B: 371-384.

Spurling, R.G. (1953) Lesions of the Lumbar Intervertebral Disc. Springfield, IL: CC Thomas, pp. 17-35.

Stilwell, D.L. (1956) The nerve supply of the vertebral column and its associated structures in the monkey. Anat. Rec. 125(2): 139-169.

Sullivan, W.E. (1969) Skeleton and joints. In Hartman, C.G., and W.L. Straus, Jr. (eds): The Anatomy of the Rhesus Monkey. New York: Hafner Publishing Co., pp. 43-84.

Tilton, F.E., J.J. Degioanni, and V.S. Schneider (1980) Long term follow-up of Skylab bone demineralization. Aviat. Space Environ. Med. 51: 1209-1213.

Turek, S.L. (1977) Orthopaedics: Principles and Their Application. Philadelphia: J.B. Lippincott, pp. 1322-1328.

Turner, R.T., J.D. Bobyn, P. Duvall, E.R. Morey, D.J. Baylink, and M. Spector (1981) Evidence for arrested bone formation during spaceflight. Physiologist 24(6): 597-598.

VanDenHoof, A. (1964) Polysaccharide histochemistry of endochondral ossification. Acta Anat. 57: 16-28.

Van Sickle, D.C. (1984) Experimental models of osteoarthritis. In (ed): Comparative Pathobiology of Major Age-Related Diseases: Current Status and Research Frontiers. New York: Alan R. Liss, Inc., pp. 175-188.

Van Sickle, D.C., and L.E. Kazarian (1982) Chronic effects of +Gz impact of the baboon spine. In (ed): Impact Injury Caused by Linear Acceleration Mechanisms, Prevention and Cost. Neuilly Sur Seine: AGARD, pp. 1-1.

Vernon-Roberts, B. (1980) The pathology and interrelation of intervertebral disc lesions, osteoarthrosis of the apophyseal joints, lumbar spondylosis and lowback pain. In Jayson, M.I. (ed): The Lumbar Spine and Back Pain. New York: Pitman Medical, pp. 83-114.

Walmsley, R. (1953) The development and growth of the intervertebral disc. Edinburg Medical J. 60: 341-364.

Whitehouse, W.J., E.D. Dyson, and C.K. Jackson (1971) The scanning electron microscope in studies of trabecular bone from a human vertebral body. J. Anat. 108: 481-496.

Wolfe, H.J., W.G. Putschar, and A.L. Vickery (1965) Role of the notochord in human intervertebral disk. I. Fetus and infant. Clin. Orthop. 39: 205-212.

Wronski, T.J., and E.R. Morey (1983) Inhibition of cortical and trabecular bone formation in the long bones of immobilized monkeys. Clin. Orthop. Rel. Res. 181: 269-276.

Wronski, T.J., E. Morey-Holton, and W.S. Jee (1981) COSMOS 1129: Spaceflight and bone changes. Physiologist 23: 579-738.

Yagodovsky, V.S., L.A. Triftanidi, and G.P. Gorokhova (1976) Space flight effects on skeletal bones of rats (light and electron microscopic examination). Aviat. Space Env. Med. 47: 734-738.

PUBLICATIONS

Eurell, J.C. and L.E. Kazarian. The scanning electron microscopy of compressed vertebral bodies. Spine 7(2): 123-128, 1982.

Eurell, J.A., L.E. Kazarian, W. Blakeney and P. Gordon. The scanning electron microscopy of compressed spinal units. Anatomia Clinica 5: 35-40, 1983.

Eurell, J.A., and L.E. Kazarian. The scanning electron microscopy of the vertebral column of the rhesus monkey. In preparation.

Eurell, J.A., and L.E. Kazarian. The quantitative histochemistry of the vertebral column of the rhesus monkey. In preparation.

Eurell, J.A., L.E. Kazarian, and D.C. Van Sickle. The microscopy of the effects of +Gz impact on baboon spines. In preparation.

Eurell, J.A., C. Oloff, K.C. Smith, and L.E. Kazarian. The histomorphometry of vertebral bodies, femurs, and ribs from rhesus monkeys exposed to hypokinesia. In preparation.

PROFESSIONAL PERSONNEL ASSOCIATED WITH RESEARCH EFFORT

Dr. Jo Ann C. Eurell, Principal investigator

INTERACTIONS

Presentations:

Eurell, J.A. and L.E. Kazarian, the Schmorl's Node and Burst Fractures, May 24-28, 1980, International Society for the Study of the Lumbar Spine, New Orleans, LA.

Briefing on research at Review of Air Force Sponsored Basic Research in Environmental Physiology and Biomechanics, September 23-25, 1980, Lexington, KY.

Eurell, J. and L. Kazarian. The quantitative histochemistry of lumbar vertebrae from rats following flight in space. International Society for the Study of the Lumbar Spine. Paris, France, May 16-21, 1981.

Presentations (cont'd)

Eurell, J. Analysis of long bone and vertebral failure patterns. Review of Air Force Sponsored Basic Research in Environmental Physiology and Biomechanics. San Antonio, TX, March 15-17, 1982.

Eurell, J. and L. Kazarian. The scanning electron microscopy of the vertebral column from baboons following vertical impaction, June 6-10, 1982, International Society for the Study of the Lumbar Spine, Toronto, Canada.

Eurell, J.A., L.E. Kazarian, and D.C. Van Sickle. The Microscopy of the Effects of +Gz Impact on Baboon Spines, February 6-9, 1984, Orthopaedic Research Society, Atlanta, GA.

Eurell, J.C. and L.E. Kazarian. Scanning Electron Microscopy of the Pre-Adult Rhesus Monkey Vertebral Column, June 3-6, 1984, International Society for the Study of the Lumbar Spine, Montreal, Canada.

Visits to Air Force Laboratories:

To Wright Patterson AFB, AFAMRL/BBD
- June 16-20, 1980
- February 19-20, 1981
- June 21-26, 1981
- June 21-23, 1982
- December 19-21, 1982
- June 13-15, 1984

INVENTIONS AND PATENTS

None